12-13-2008

Experiments And Modeling Of Fatigue And Fracture Of Aluminum Alloys

J Brian Jordon

EXPERIMENTS AND MODELING OF FATIGUE AND FRACTURE OF ALUMINUM ALLOYS

By

James Brian Jordon

A Dissertation
Submitted to the Faculty of
Mississippi State University
in Partial Fulfillment of the Requirements
for the Degree of Doctor of Philosophy
in Mechanical Engineering
in the Department of Mechanical Engineering

Mississippi State, Mississippi

December 2008

EXPERIMENTS AND MODELING OF FATIGUE AND FRACTURE OF ALUMINUM ALLOYS

By

James Brian Jordon

Approved:

Mark F. Horstemeyer Center for Advanced Vehicular Systems Chair in Computational Solid Mechanics Professor of Mechanical Engineering (Major Professor)	James C. Newman, Jr. Professor of Aerospace Engineering (Committee Member)
Steven R. Daniewicz Professor of Mechanical Engineering (Graduate Coordinator and Committee Member)	John T. Berry Professor of Mechanical Engineering (Committee Member)
Haitham El Kadiri Research Professor Center for Advanced Vehicular Systems (Committee Member)	Sarah A. Rajala Dean of the Bagley College of Engineering

Name: James Brian Jordon

Date of Degree: December 12, 2008

Institution: Mississippi State University

Major Field: Mechanical Engineering

Major Professor: Dr. Mark F. Horstemeyer

Title of Study: EXPERIMENTS AND MODELING OF FATIGUE AND FRACTURE OF ALUMINUM ALLOYS

Pages in study: 132

Candidate for degree of Doctor of Philosophy

In this work, understanding the microstructural effects of monotonic and cyclic failure of wrought 7075-T651 and cast A356 aluminum alloys were examined. In particular, the structure-property relations were quantified for the plasticity/damage model and two fatigue crack models. Several types of experiments were employed to adapt an internal state variable plasticity and damage model to the wrought alloy. The damage model was originally developed for cast alloys and thus, the model was modified to account for void nucleation, growth, and coalescence for a wrought alloy. In addition, fatigue experiments were employed to determine structure-property relations for the cast alloy. Based on microstructural analysis of the fracture surfaces, modifications to the microstructurally-based MultiStage fatigue model were implemented. Additionally, experimental fatigue crack results were used to calibrate FASTRAN, a fatigue life

prediction code, to small fatigue-crack-growth behavior. Lastly, a set of experiments were employed to explore the damage history effect associated with cast and wrought alloys and to provide motivation for monotonic and fatigue modeling efforts.

DEDICATION

I would like to dedicate this work to my wife, Amy, who has supported me with love and respect, through the five years of graduate school. I love you Amy.

ACKNOWLEDGMENTS

First, I would like to thank my advisor Dr. Mark Horstemeyer, who, without his direction, input, mentoring, and friendship, this dissertation would not be possible. I would also like to thank Dr. James Newman, Jr., for introducing me to the world of fracture mechanics and to the damage tolerance modeling approach. Special thanks go to Dr. Steven Daniewicz, Dr. John Berry, and Dr. Haitham El Kadiri and for their advice in the writing of this dissertation. Expressed appreciation is also due to Dr. Yibin Xue, Dr. Youssef Hammi, Dr. Kiran Solanki, and Dr. Ricolindo Carino for their help with the numerical simulations. I want to thank Jairus Bernard for his assistance in performing experiments and finite element simulations. Also, I would like to thank Northrop Grumman Corp. and the James Worth Bagley College of Engineering for their financial support of this research. Additionally, I would like to express gratitude to my wife, Amy, for all of the support she gave during the late nights and long weekends. Finally, I want to thank my Lord and Savior for His unfailing goodness and grace on my life.

TABLE OF CONTENTS

Page

PAGE

LIST OF TABLES

TABLE Page

LIST OF FIGURES

FIGURE Page

FIGURE Page

FIGURE Page

FIGURE Page

FIGURE Page

FIGURE Page

CHAPTER I

INTRODUCTION

Failure of engineering alloys resulting from monotonic and cyclic loading is still an area of ongoing research. Understanding the mechanisms associated with ductile fracture can be used to predict the strength and ductility of an alloy. Therefore, characterizing the microstructure of the metal can provide motivation for a physical-based modeling approach. In addition, microstructure-based modeling can also be applied to the area of fatigue. Thus, the purpose of this work is to further understanding of failure of aluminum alloys due to monotonic and cyclic loading by performing experiments and updating models.

Chapter II presents experimental characterization and modeling results of monotonic failure of 7075-T651 aluminum alloy. The anisotropy of the wrought alloy was analyzed in terms of microstructural features. The microstructural characterization was then used to modify an internal state variable plasticity/damage model that was employed to predict the anisotropic stress and damage state of the alloy.

Chapter III presents fatigue experiments for an A365-T6 cast aluminum alloy. In addition, inclusion-property relations were determined based on scanning electron

microscopy analysis of the fracture surfaces. Information gained through this analysis was integrated into a microstructural-based fatigue model.

Chapter IV presents microstructurally small fatigue crack growth experimental results for 7075-T651 aluminum alloy for several load ratios. Additionally, using the small crack data, a damage tolerance type fatigue life prediction code was employed to bound the fatigue life results based on observed initial flaw sizes.

Chapter V presents experimental and modeling results of prestrain-followed-by-fatigue and pre-fatigue-followed-by-tensile tests for both 7075-T651 and A356-T6 aluminum alloys. Also, the models presented in Chapter II and IV were employed to predict the stress and damage state associated with these types of experiments.

Lastly, Chapter VI summarizes the results of the work performed in this research and also presents recommendations for future research.

CHAPTER II

ANISOTROPY OF A WROUGHT ALUMINUM ALLOY

Introduction

Materials which show an isotropic material response in the elastic regime often exhibit anisotropic characteristics in the inelastic regime. This is particularly true during material processing, such as rolling or extrusion, where metal alloys under extensive plastic deformation exhibit a significant anisotropy in mechanical and fracture properties. Void-like cavities and second phase inclusions are elongated and oriented (if not equiaxed) in such a way that the larger axis tends to align itself along the maximum principal load direction (Fig. 2.1) because of texture.

Elongated particle aspect ratios have been shown to subsequently generate an anisotropic structural response and strongly influence the ductile fracture of structural steels, where macroscopic compliances evolve differently in orthogonal directions (Garrison and Moody, 1987; Tirosh *et al*., 1999; Gray et al., 2000). This orientation dependent ductility leads to a pronounced anisotropy of the damage evolution (see Fig. 2.2) in quasi-static fracture responses (Tvergaard and Needleman, 2006) and under ballistic impact conditions.

In terms of the fracture of a 7xxx series aluminum alloy, ductile failure occurs by void nucleation, void growth, and void coalescence (Gurland and Plateau, 1963; McClintock 1968; Hahn and Rosenfield, 1975; Rawal and Gurland, 1977; Starke, Jr, 1977). Void nucleation primarily occurs either by particle-matrix decohesion or by particle fracture of intermetallics. Particle void nucleation is generally governed by the size, shape, and orientation morphologies of the particle (Horstemeyer *et al*., 2003). In addition, void nucleation can also occur at precipitate particles or larger intermetallic inclusions (Garrison and Moody, 1987). Void growth involves enlargement of the newly nucleated void and requires continuous plastic deformation. Finally, void coalescence takes place by the joining of multiple voids by either void impingement (Garber *et al*. 1976) or microvoid sheet mechanisms (Rogers, 1960, 1968). Kirman (1971) showed that intergranular void sheet coalescence could occur in 7075 aluminum alloy.

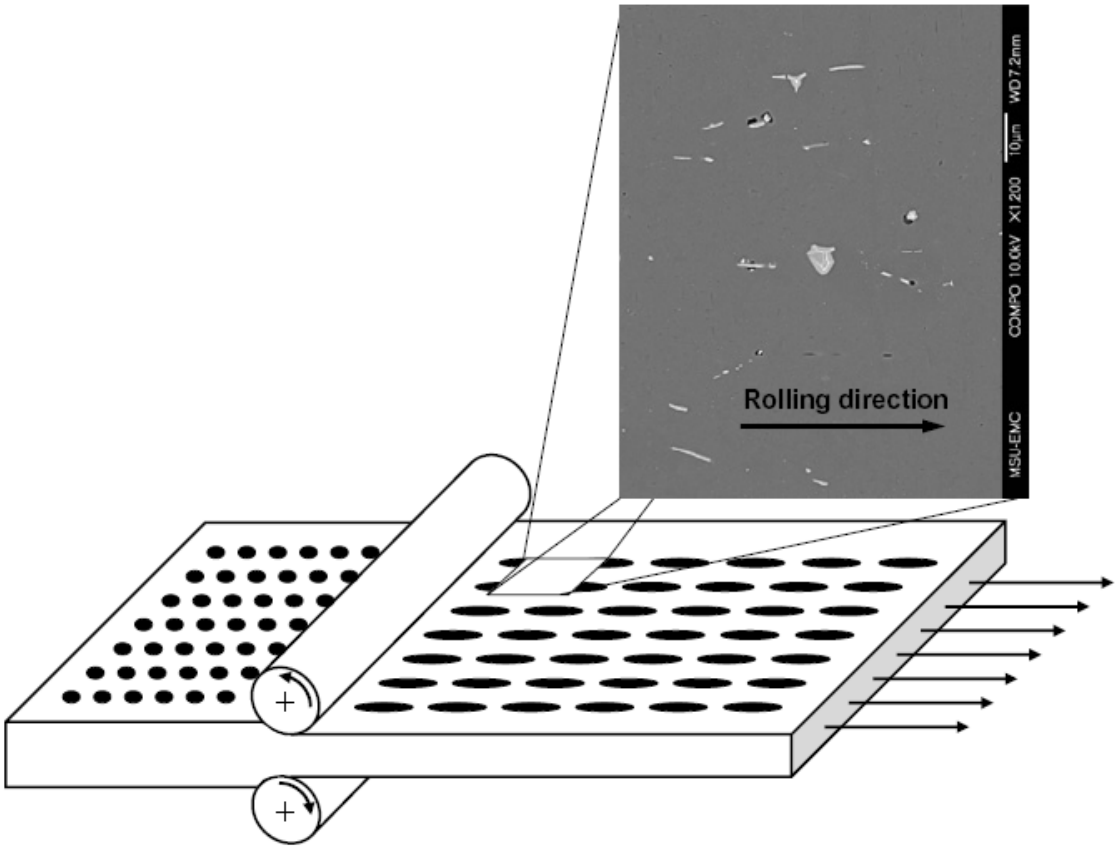

Figure 2.1 Schematic description of a rolling process and inclusion distribution in the aluminum alloy 7075-T651.

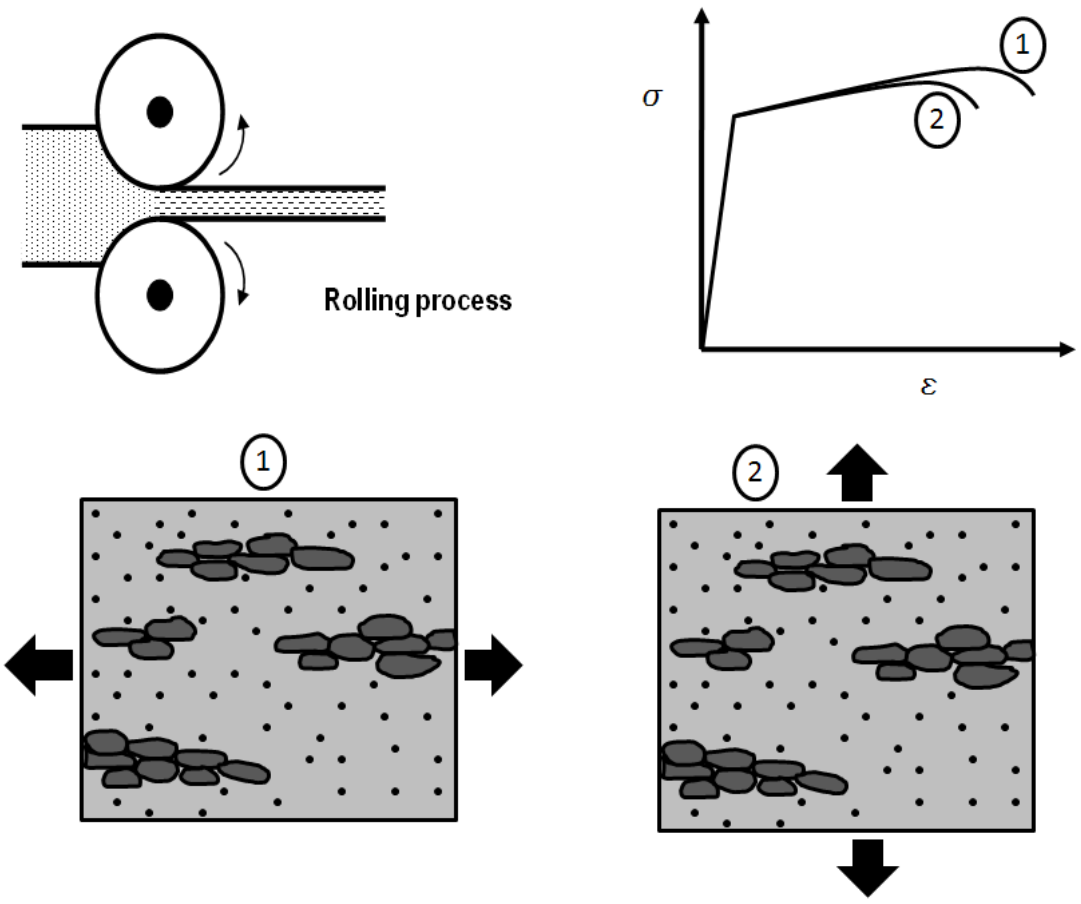

Figure 2.2 Schematic description of a rolling process and associated anisotropic deformation in the aluminum alloy 7075-T651. The large particles represent the iron-based intermetallics and the smaller particles represent the coarse precipitates.

A topic less frequently discussed is the effect of void nucleation and growth from coarse precipitates or dispersoids. Work by Haynes and Gangloff (1997), Hahn and Rosenfeld (1975), Liu *et al*. (2004, 2005), and Asserin-Lebert *et al.* (2005) has shown that in aluminum alloys, void nucleation and growth occur at coarse precipitates and or dispersoids. While void nucleation and growth from larger intermetallics generally

control ductility, the void growth from smaller sub-micron particles can have an effect on the damage rate, further reducing the ductility (Cox and Low, 1974, Marini *et al*., 1985; Faleskog and Shih, 1997; Perrin and Leblond, 1990 and 2000; Tvergaard and Needleman, 1992; Tvergaard, 1998; Horstemeyer and Ramaswamy, 2000). Recent modeling work by Fabregue and Pardoen (2008) showed that the void growth from secondary particles affected the coalescence of the primary voids.

Determining through thickness tensile properties of rolled plates and sheet metals is an important and yet, today, still a difficult task. As such, a through thickness apparatus was first proposed and developed by Oppenheimer and Berry (1968) to experimentally explore the anisotropy of 7075-T651 aluminum alloy. The design of the double ligament tensile (DLT) apparatus allows for very low compliance due to the stiffness of the fixture and the clamping of the specimens as shown in Fig. 2.3. Fig. 2.4 shows the DLT specimen design. Initially, Oppenheimer and Berry used the DLT specimens for impact studies on rolled steel plates. They tested a wide variety of very low carbon steels and their results showed that the impact energy varied as a function of specimen orientation in the plate. Later, the DLT test was employed to determine factors related to the tensile properties in the short transverse direction for both steels and aluminum alloys (Kumble *et al*., 1975; Berry *et al*., 1975; Kumble and Berry, 1976; Meyers *et al*., 1983; Srivatsan *et al*., 1985; Meyers, 1986). More specifically, Stoltz *et al*. (1983) studied an ultra high strength steel (AISI 4340) and found good agreement between standard tensile test results and the DLT experiments. Johnson (1994) tested a hot-rolled low-carbon steel plate (AISI 1014) and a higher strength steel (5B67629) as

well as an extruded aluminum alloy (Al 6090-T6). Likewise, Johnson found good agreement for the steels compared to standard-size tensile specimens. Srivatson *et al*. (1987) tested a wrought 7075-T651 aluminum alloy to quantify elongations to failure using the DLT test. They found that the specimens aligned in the rolling direction had the greatest elongation and the specimens in the short transverse direction had the lowest elongation. Srivatson *et al*. concluded that not only is the grain orientation the cause of the anisotropy but also the intermetallic constituents of the 7075-T651 aluminum alloy.

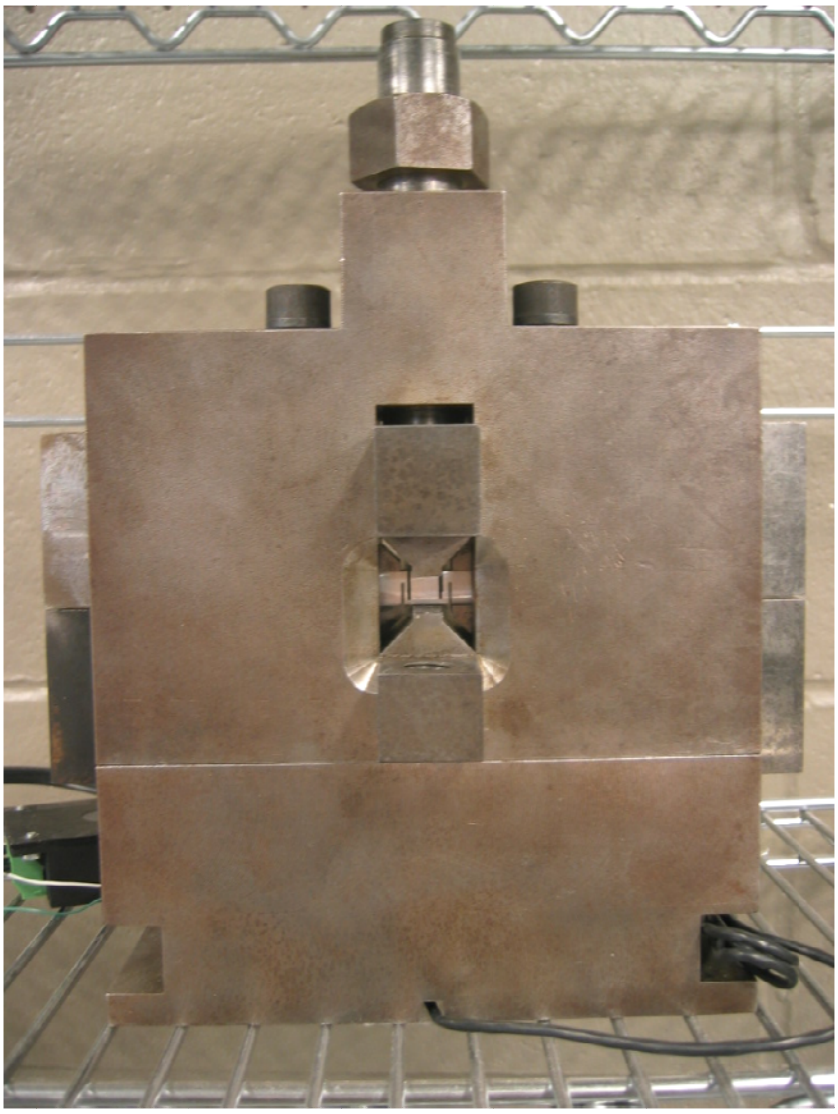

Figure 2.3 Front sectional view of DLT test fixture.

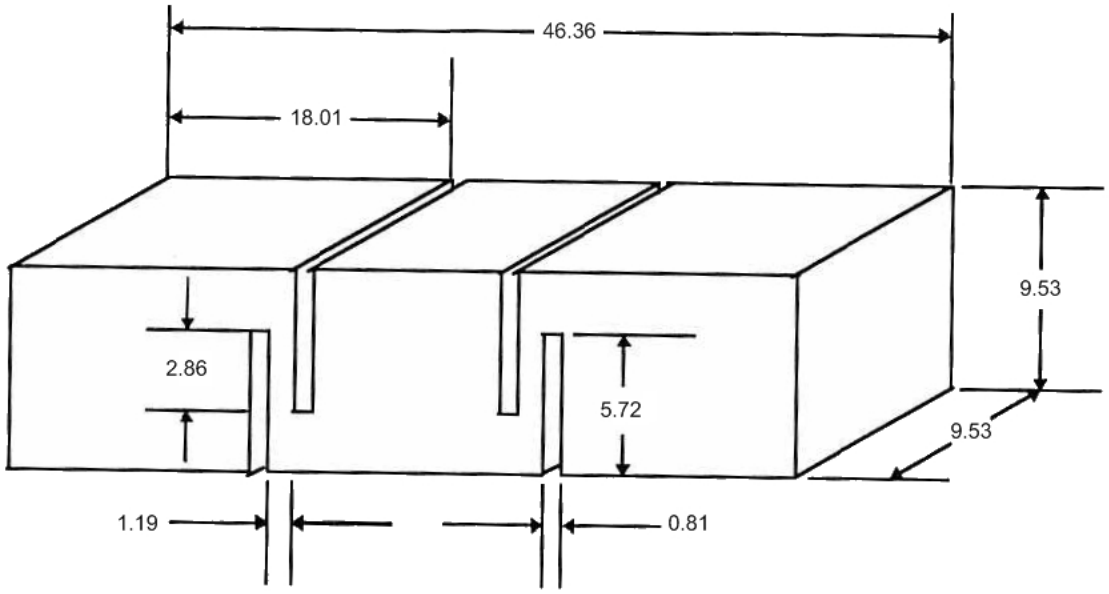

Figure 2.4 Specimen dimensions of the Double Ligament Tensile Specimen (Johnson, 1994).

Several modeling efforts have attempted to optimize and understand the stress state of the DLT specimen. Both Kumble (1975) and Johnson (1994) used finite element methods to elucidate the stress state in the gage length of the ligament and to optimize the design of the DLT specimen. Kumble (1975) used two-dimensional plane strain linear elastic calculations to optimize the ligament length. In addition, Kumble (1975) determined that a correction factor was needed to achieve good agreement between his two-dimensional calculations and the DLT tensile experiments with the low carbon steels. Later, Johnson (1994) employed a two-dimensional elastic/plastic finite element model that demonstrated that a correction factor was not needed.

In this work, the importance of anisotropic damage on ductility will be illustrated by using a sub-standard tensile design to experimentally characterize the material as a

function of the specimen direction relative to the rolling direction. The second goal is to employ an internal state variable plasticity/damage model to capture the void nucleation, growth and coalescence occurring at primary and secondary particles for the wrought 7075-T651 aluminum alloy. The continuum level material model used in this study reflects a multi-length scale effect by including microstructure detail such as inclusion/defect size, area fraction, and nearest neighbor distance, all as a function of specimen orientation.

Experiments and Materials

The 7075-T651 aluminum alloy is a wrought product with a relatively high yield strength and good ductility. As displayed by the triplanar optical micrographs shown in Fig. 2.5, the grains of this wrought alloy were found to be pancake shaped and aligned in the rolling direction of the wrought plate.

For this metallography study, specimens were mounted and polished using standard polishing techniques and examined under an optical microscope. Fig. 2.6 displays typical 7075-T651 aluminum alloy microstructure in the untested condition. The alloy contains two main types of primary (or large) particles: iron rich particles ($Al_6(Fe,Mn)$, Al_3Fe, $\alpha Al(Fe,Mn,Si)$ and Al_7Cu_2Fe); and silicon-based particles (Mg_2Si). The iron-rich intermetallic particles are seen in the optical micrograph (Fig. 2.7) as light grey particles and the Mg_2Si intermetallics are shown as dark particles. The distribution of the particle size, nearest neighbor distance, and aspect ratio for the iron-rich and Mg_2Si

intermetallics in the untested condition were tabulated from a 5.75 mm^2 area of material for each of the orientations and are shown in Fig 2.7. Fig 2.7a displays the area size of the particles, Fig. 2.7b displays the nearest neighbor distance of the particles and Fig. 2.7c displays the aspect ratio distributions of the particles. The mean values of the particle area, area fraction, aspect ratio and nearest neighbor distances in the untested condition are displayed in Table 2.1. Due to their small size (50-150 nm), the secondary or rather small particles (coarse precipitates) were assumed to be equiaxed and thus the aspect ratio distribution was not presented. The average size and nearest neighbor values for the coarse precipitates were estimated from the fracture surfaces. In addition to the intermetallic particle stereography, the average grain size was determined by EBSD analysis taken in (L), (LT), and (ST) directions and the results are listed in Table 2.1. Fig. 2.8 displays the grain morphology of the 7075-T651 aluminum alloy and pole figures (Fig. 2.9) further illustrate the anisotropic nature of the wrought product.

Figure 2.5 Triplanar optical micrograph illustrating the grain structure and orientation of 7075-T651 aluminum alloy.

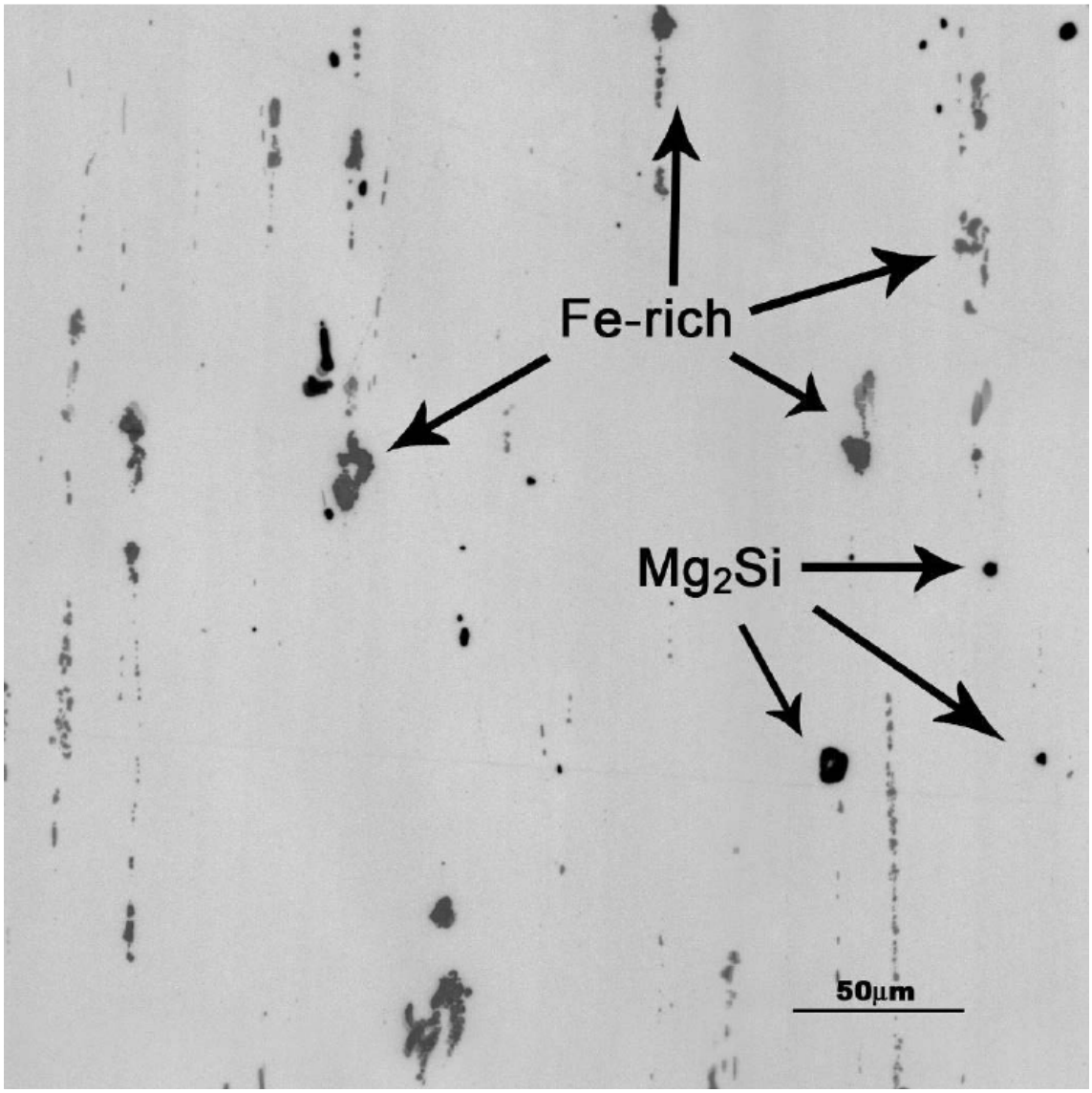

Figure 2.6 Microstructure of untested 7075-T651 aluminum alloy (Harris, 2006).

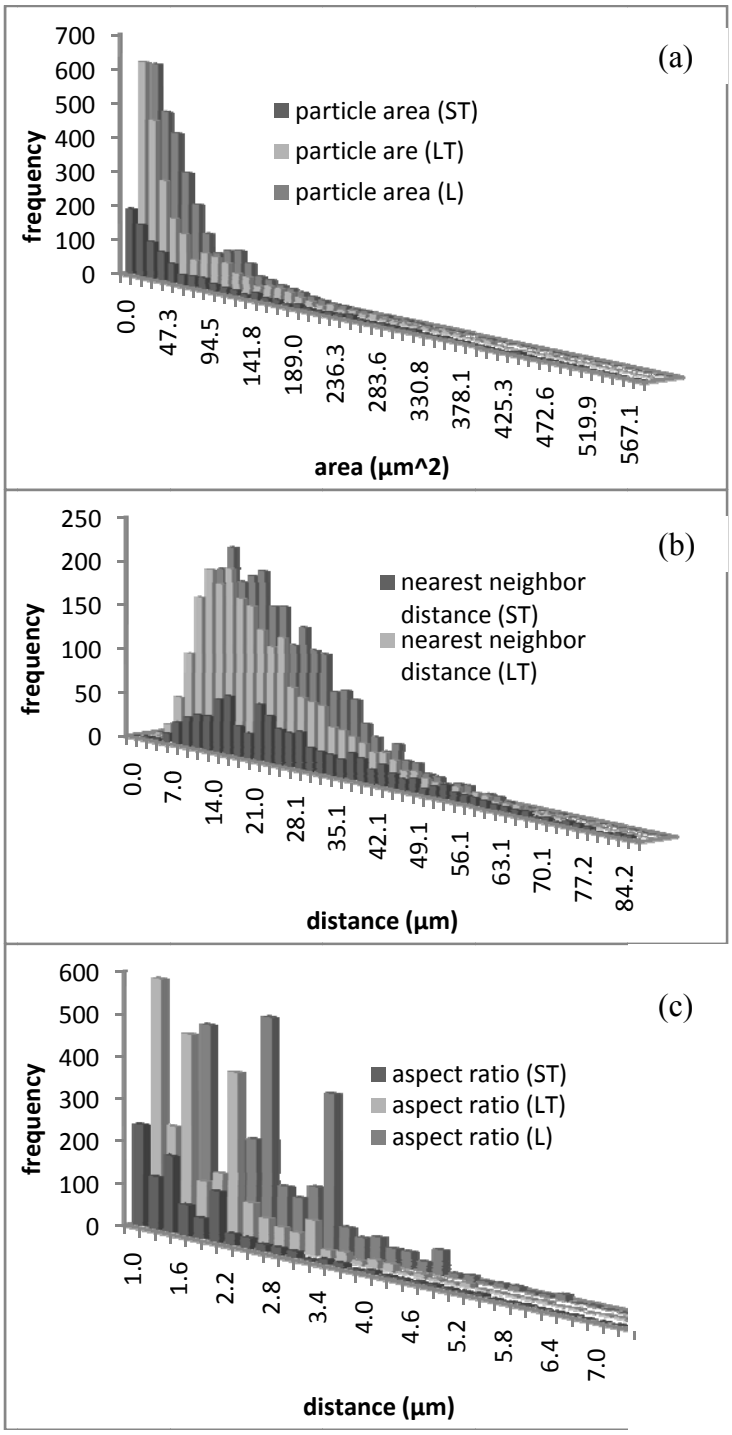

Figure 2.7 Stereological comparison of distributions of intermetallic particles (large) in 7075-T651 aluminum alloy for the longitudinal (L), long transverse (LT), and short transverse orientation (ST): a) particle area, b) nearest neighbor distance, c) aspect ratio.

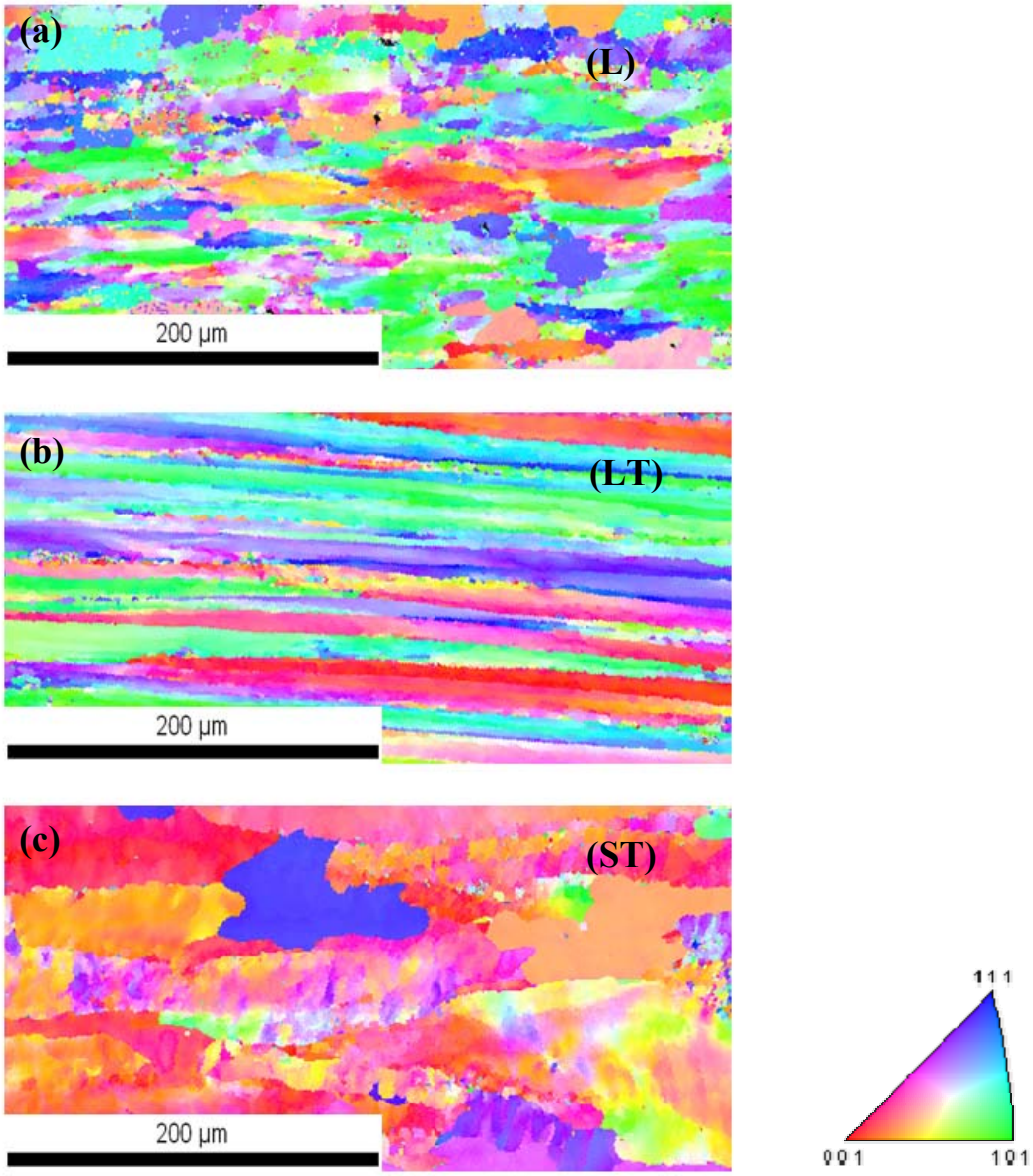

Figure 2.8 Microstructural grain orientation and size analysis for 7075-T651 aluminum alloy in the longitudinal (a), long transverse (b), and short transverse orientations (c) demonstrate the anisotropic behavior of the alloy due to the rolling process.

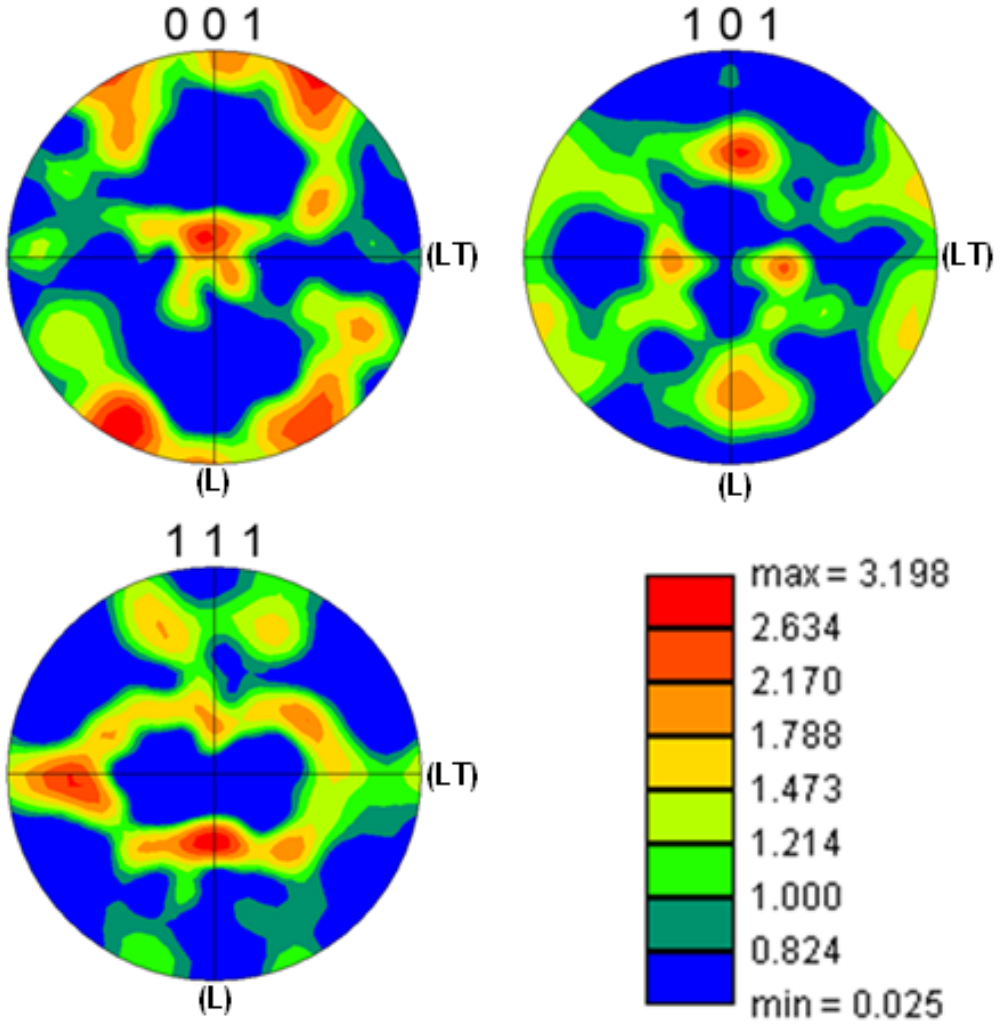

Figure 2.9 Crystal orientation of the wrought 7075-T651 alloy.

In order to properly model the 7075-T651 alloy, standard monotonic experiments were performed (ASTM E8). Due to the thickness restrictions of the rolled plate (50.8 mm), only tensile specimens in the longitudinal and long transverse directions were tested. In addition, compression and torsion tests were conducted in the longitudinal direction for further characterization of the material. All experimental specimens were

machined 2.54 mm from the rolling surface of the plate. The tension, compression, and torsion tests were performed with a strain rate of 0.001/sec in an ambient laboratory environment.

The DLT experiments were performed following the procedures presented by Oppenheimer and Berry (1968) and Berry *et al*. (1985). The testing apparatus (Fig. 2.3) was placed between the compression platens of a 5800 Instron electric mechanical test frame, and a linear variable differential transformer located within the DLT apparatus provided local displacement values of the DLT specimens. The experimental stress/strain curves were tabulated by taking load and displacement values and by using the nominal cross-sectional and ligament lengths (Oppenheimer and Berry, 1968). In order to obtain statistically accurate results, three specimens for each direction of the alloy were tested. The mean standard deviation of the DLT experimental tests were approximately 0.012 for all three orientations.

Several observations can be made from the experimental results: The percent elongation for the DLT in the longitudinal (L) direction was the greatest; next was the long transverse (LT); the short transverse (ST) had the smallest elongation. In addition, the standard deviation values of the elongation to failure showed that the DLT tests produced repeatable results regardless of the specimen orientation. The fracture surfaces of the DLT specimens were examined under the electron scanning microscope (SEM). In order to illustrate the anisotropy of the 7075-T651 aluminum alloy, triplanar micrographs of the fracture surfaces are shown in Fig. 2.10. In the (L) orientation, large fractured intermetallics were surrounded by smaller course precipitates that nucleated voids which

in turn grew and coalesced. The (LT) orientation fracture surface was similar to the (L), however, due to the alignment of the grains and stringer particles, the fracture surface was segregated more acutely into distinct areas. These distinct areas included clustering of the particles enclosed by areas that were intermetallic free. Also, the fractured intermetallics for the (LT) constituted a larger percentage of the fracture surface compared to the (L) orientation. The (ST) fracture surface revealed an anisotropic morphology arising from the stringer particles nucleating primary voids; the voids then coalesced together creating a "woody-like" fracture surface. In addition, it was found that the coalescence path between the stringer particles occurred at grain boundaries (intergranular damage) and that decohesion of the precipitates occurred (but not void growth). Also, it was observed that the course precipitates debonded in all three directions and no fracture of the particles were observed. In contrast, the large intermetallic particles fractured and debonded in all three directions. The fracture surface images were analyzed to quantify the void number density in the three orientations (L, LT, ST). The analysis quantified the damage resulting from both primary particles (intermetallics) and secondary particles (coarse precipitates) and the results are shown in Table 2.2.

Table 2.1 Metallographic analysis of un-tested aluminum 7075-T651 alloy: mean area particle fraction, particle size, nearest neighbor distance and grain size.

Specimen direction	Primary Particle Area Fraction	Secondary Particle Area Fraction	Avg. Primary Particle Size (μm²)	Avg. Secondary Particle Size (μm²)	Avg. Primary Nearest Neighbor Distance (μm)	Avg. Grain Size (μm)
Longitudinal (L)	0.025	0.032	68.2	0.0031	18.7	18.9
Long Transverse (LT)	0.029	0.032	97.9	0.0040	16.7	24.0
Short Transverse (ST)	0.028	0.032	202.0	0.0098	21	33.00

Table 2.2 Post failure Metallographic analysis of 7075-T651 alloy fracture surfaces.

Specimen direction	Primary Void Density ($\#/mm^2$)	Secondary Void Density ($\#/mm^2$)
Longitudinal (L)	2700	$8.6x10^6$
Long Transverse (LT)	1880	$5.2x10^6$
Short Transverse (ST)	383	$2.4x10^6$

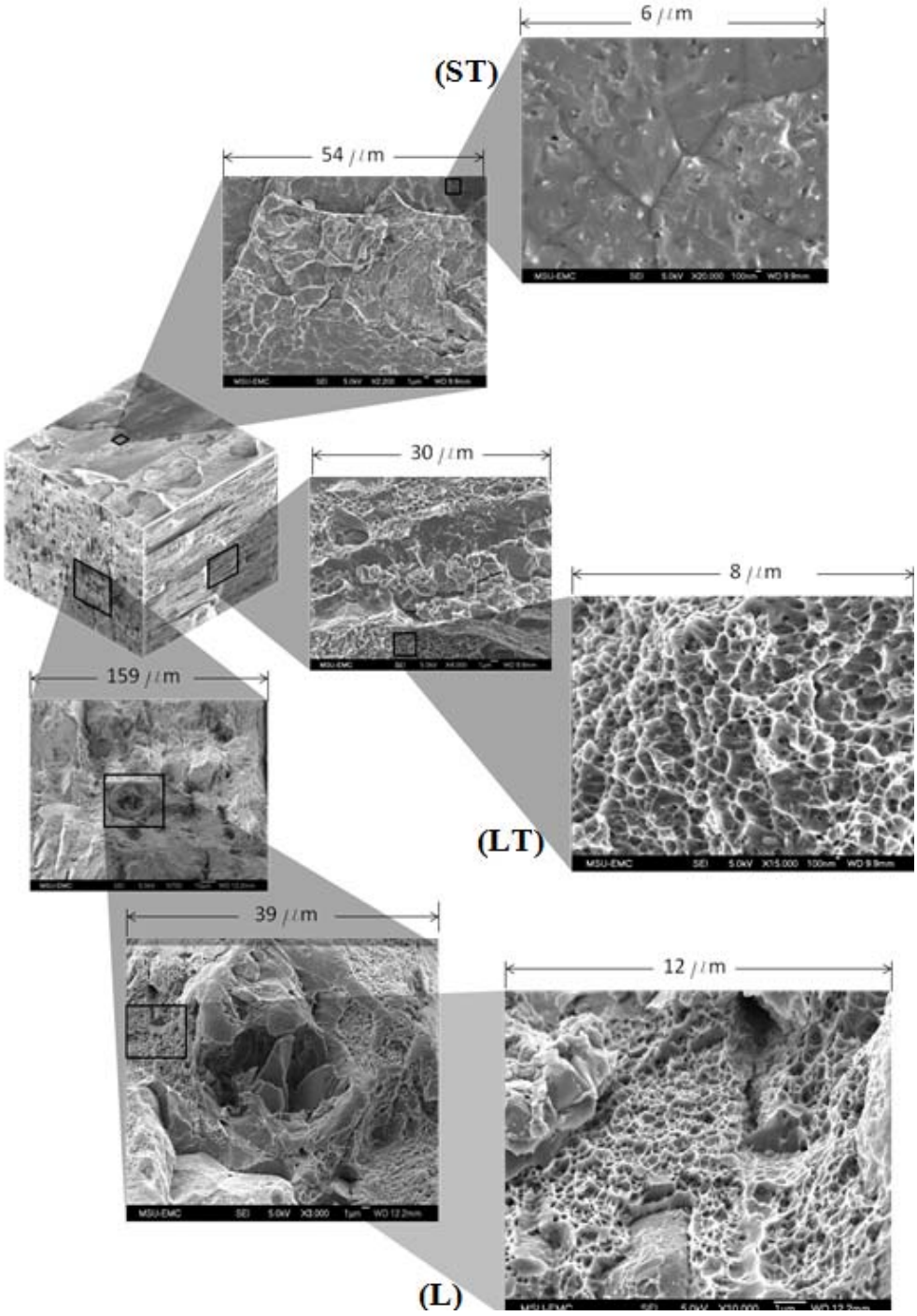

Figure 2.10 Fracture surface of 7075-T651 aluminum alloy show bi-modal fracture resulting in intermetallic fracture and void growth and coalescence of the coarse precipitates for the longitudinal (L), long transverse (LT) and short transverse (ST) orientations.

Internal State Variable Model

The material model employed in this present study is the internal state variable (ISV) plasticity/damage model introduced by Bammann et al. (1984, 1989, 1990, 1993, 1996) and later modified by Horstemeyer and Gohkale (1999) and Horstemeyer *et al*. (2000). For this study, the total damage was modified to account for damage arising from particles at different length scales: large intermetallics (5-20μm) and the coarse precipitates (0.05-0.15μm). Equation (2.1) is the total damage accumulation for void nucleation and growth from primary and secondary particles and void growth from initial pores or defects.

$$\phi = \left(\eta_{primary} \nu_{primary} + \eta_{\sec ondary} \nu_{\sec ondary} + \phi_{pore}\right) C \tag{2.1}$$

See Appendix A.1 for the related equations. For a more comprehensive review of the model, see Jordon *et al*. (2007).

Modeling Correlation and Results

The ISV plasticity/damage model constants for 7075-T651 aluminum alloy were determined from experimental data by using a least squared best-correlation method as employed by Jordon *et al*. (2007). The plasticity and damage constants are shown in Appendices A.2 and A.3. The model-experiment correlation process employed a different set of microstructural constants for each of the three different specimen orientations while keeping the yield, hardening, and damage parameters the same. The

microstructural constants that were varied were the particle area fraction and particle size. The constants for the kinematic and isotropic hardening equations were selected to produce the best fit of the reverse loading data presented by Jordon *et al*. (2007) while maintaining the same kinematic to isotropic hardening ratio. The nucleation rate for both the primary particles (intermetallics) and the secondary particles (coarse precipitates) were selected based on the fracture surface data presented in Table 2.2.

Three-dimensional finite element simulations were performed with the aforementioned constitutive model. A mesh refinement study was employed to determine the appropriate element size. The three different levels of mesh refinement were performed as shown in Fig 2.11: Mesh #1 contained 400 elements in the gage section; Mesh #2 contained 1200 elements in the gage section; and Mesh #3 contained 3600 elements in the gage section. In terms of flow stress, the results from the three different meshes showed that the numerical results converged. Thus, Mesh #2 was chosen for the remainder of the simulations, because the element size was approximately 10x the average grain size for the 7075-T651 alloy. In terms of the failure location, the stress state of the ligament at failure was not quite uniaxial, which contrasts the findings of Johnson (1994). The stress triaxiality at the location of failure from the finite element results was approximately 0.56 for all three directions, where stress triaxiality of uniaxial stress is 0.33 as defined by the hydrostatic stress divided by the deviatoric stress. SEM analysis of the fracture surfaces revealed that the model predicted the exact location of initial fracture. Comparison of the experimental DLT results to the ISV calculations for the (L), (LT), and (ST) are shown in Fig. 2.12-14, respectively. One benefit of the

model is that the final fracture surface can be used to quantify the different damage variables for the model. In terms of linking the results of the post-failure image analysis of the fracture surfaces to the model results, the experimental void number density at failure correlates to the void nucleation of the model. In addition, the experimental mean void area calculated from the image analysis correlates directly to the multiplication of the void growth and coalescence results from the model. Both the model and experimental void density values shown in Table 2.2, along with SEM analysis suggest a more prevalent nucleation dominated mechanism for 7075 aluminum alloy as opposed to a void growth and coalescence mechanism, although all three were clearly present.

Mesh 1

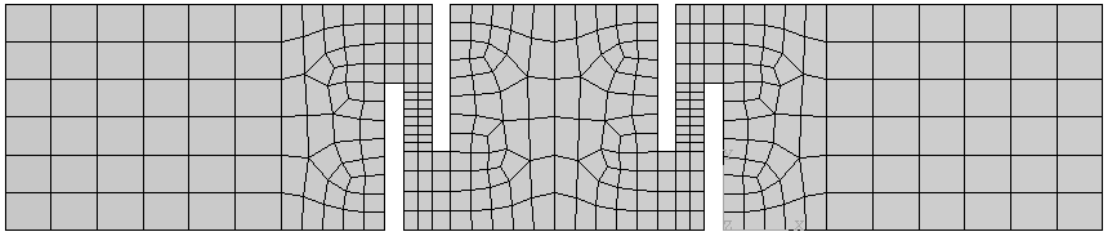

Mesh2

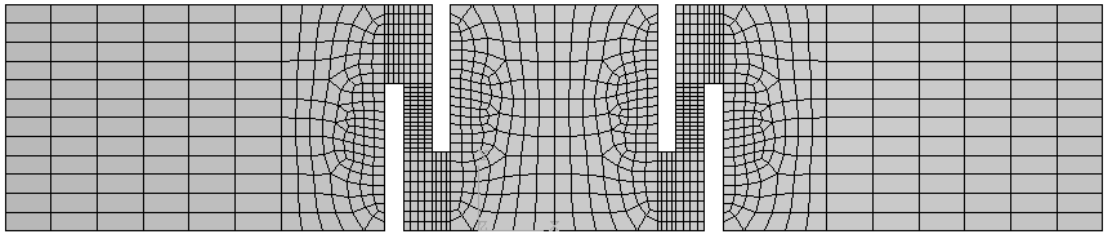

Mesh3

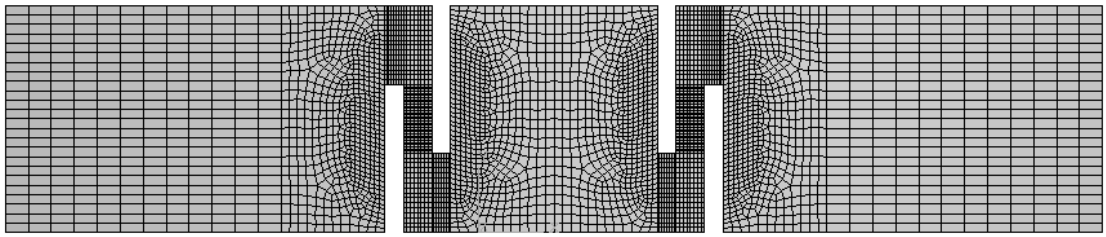

Figure 2.11 Finite Element mesh of Double Ligament Tensile Specimen: Mesh 1 contains 400 elements in the gage section; Mesh 2 contains 1200 elements in the gage section; Mesh 3 contains 3600 elements in gage section.

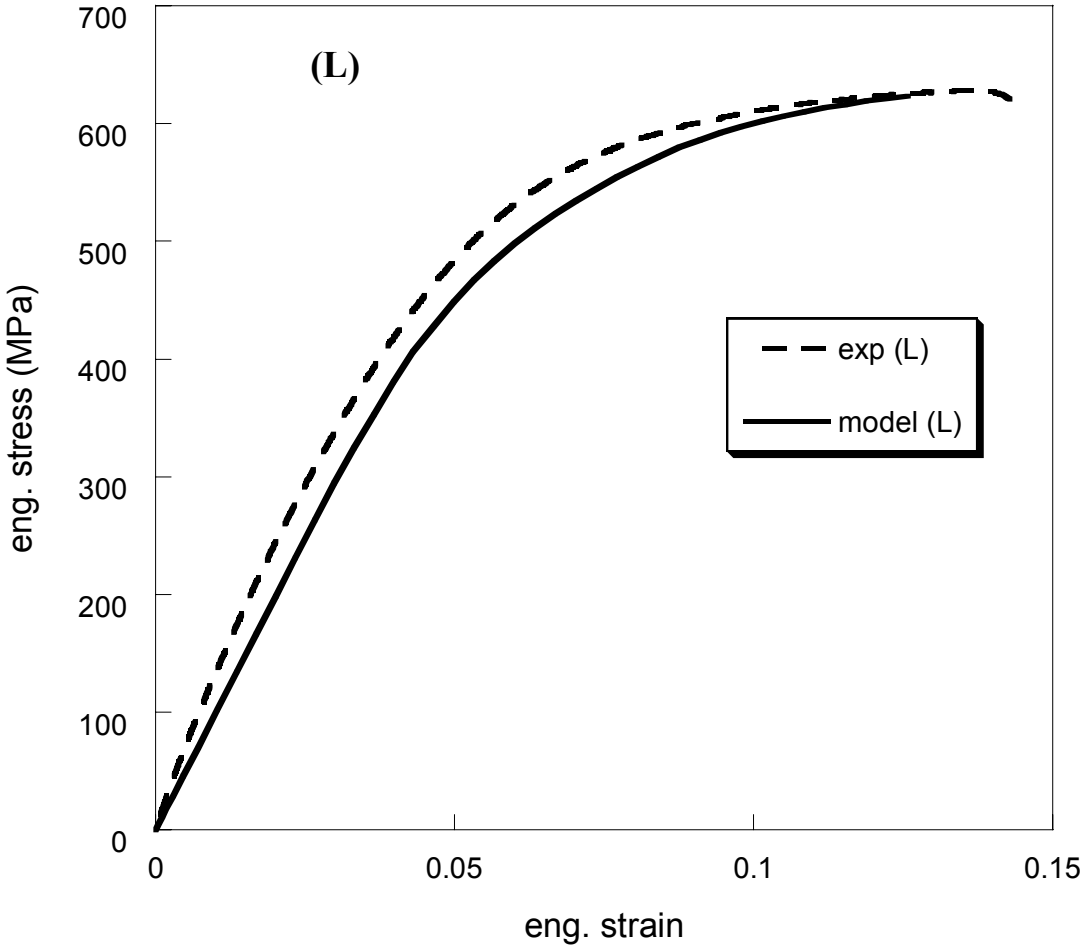

Figure 2.12 Comparison of the ISV model to the longitudinal (L) experimental results of the double ligament tension tests for the 7075-T651 aluminum alloy. This plot demonstrates that the ISV model can capture the anisotropy of the plasticity and damage associated with wrought alloys. The ISV model shows good agreement for predicting the elongation for longitudinal direction.

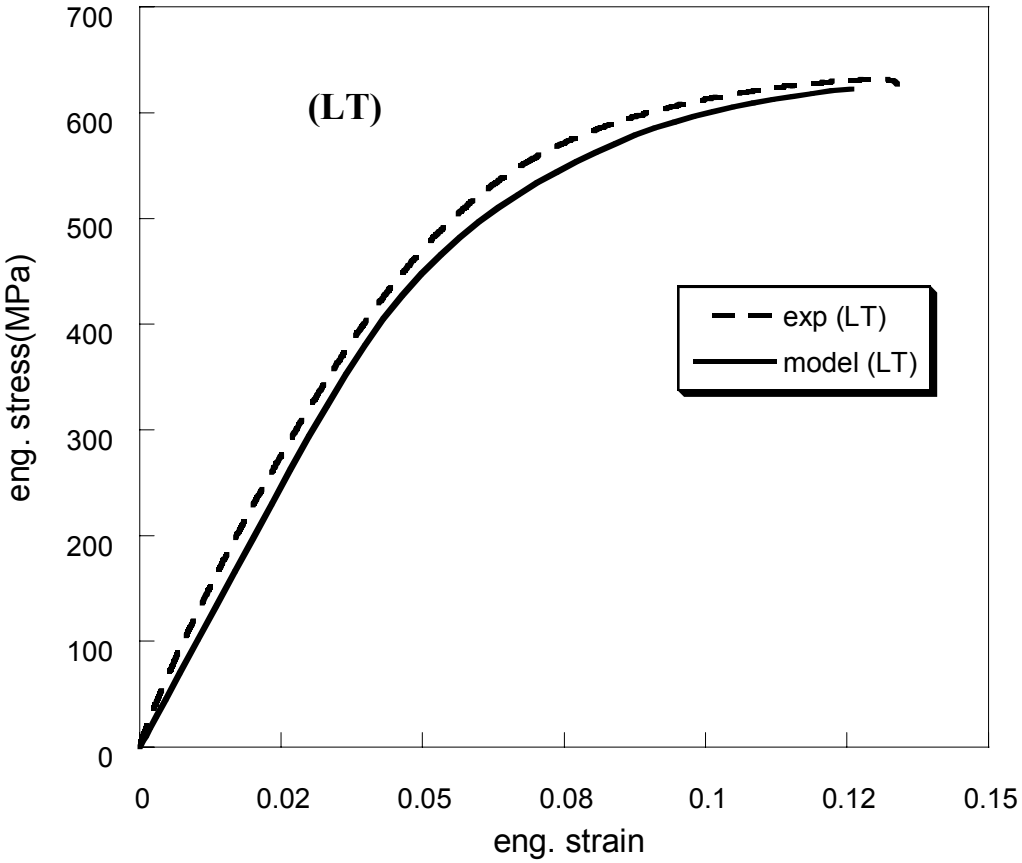

Figure 2.13 Comparison of the ISV model to the long transverse (LT) experimental results of the double ligament tension tests for the 7075-T651 aluminum alloy. This plot demonstrates that the ISV model can capture the anisotropy of the plasticity and damage associated with wrought alloys. The ISV model shows good agreement for predicting the elongation for long transverse direction.

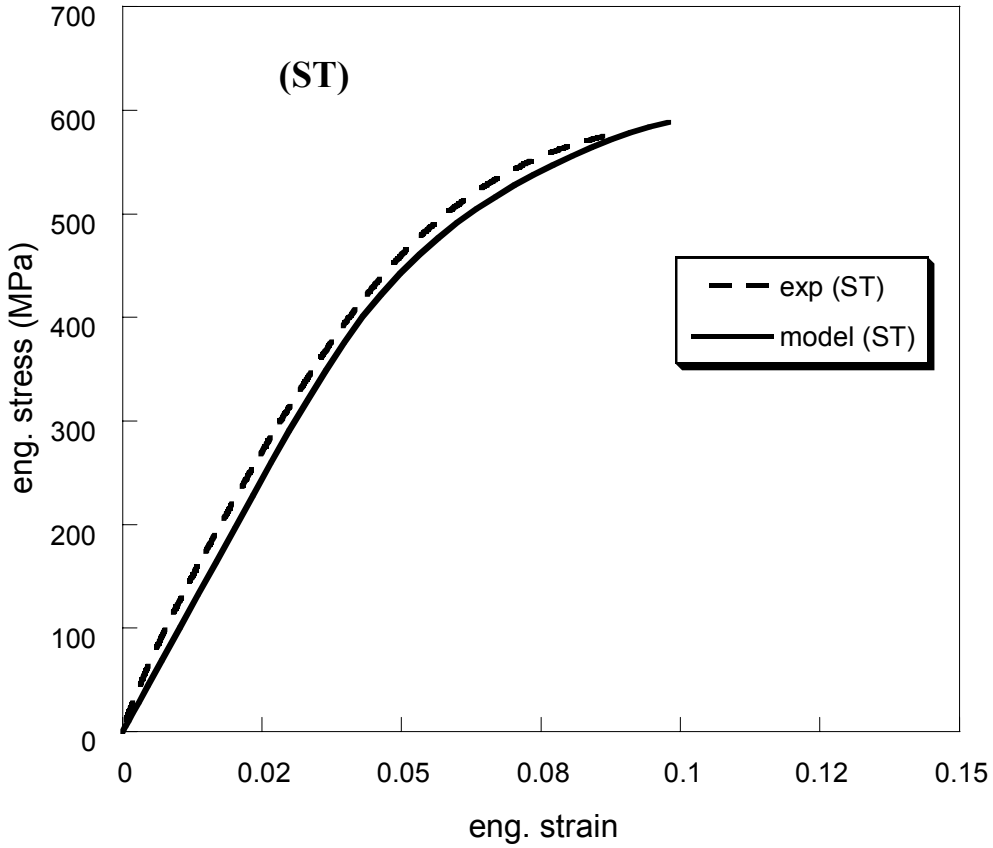

Figure 2.14 Comparison of the ISV model to the short transverse (ST) experimental results of the double ligament tension tests for the 7075-T651 aluminum alloy. This plot demonstrates that the ISV model can capture the anisotropy of the plasticity and damage associated with wrought alloys. The ISV model shows good agreement for predicting the elongation for short transverse direction.

Discussion

The main emphasis of this work is to present a model capable of capturing damage arising from entities at different length scales. The damage evolution equations provide an accurate representation of the damage progression due to large intermetallic particles and smaller course precipitates. Fig. 2.10 presents the SEM micrographs of the fracture surface of 7075-T651 aluminum alloy with the intent to demonstrate the

anisotropic nature of this wrought alloy. These micrographs clearly show that damage arose from both the intermetallic particles and the course precipitates with a varying degree, based on the orientation relative to the rolling direction. In the (L) and (LT) directions, the strengthening phases nucleated voids that grew and coalesced via void impingement. Concurrently, the relatively large iron-rich and silicon based intermetallics fractured with the larger and more elongated particles first. In the (LT) orientation, a large grouping of the stringers with greater aspect ratios led to a larger particle area fracture at a lower strain level compared to the (L) direction. Hence, the anisotropy of the intermetallic particle morphology contributed to the limited ductility. Since both (LT) and (ST) had a higher particle aspect ratio and higher nearest neighbor distance (see Fig. 2.7), the elongation to failure for these two orientations reflected the anisotropy of the mechanical behavior.

The void number density nucleating from the particle(s) was tabulated from the SEM micrographs and was used to calibrate the damage equations. While interrupted experimental data was unavailable, the validity of the final void number density determined from the fracture surface was a reasonable calibration method to determine the constants for the nucleation model. The classical dimples found on the (L) and (LT) fracture surfaces confirmed that the material experienced ductile fracture and that the plasticity/damage model presented here was applicable. In contrast, however, the lack of dimples displayed on the (ST) fracture surface was confirmed by the shorter elongation to failure compared to the other two orientations. The lack of dimples suggest that the failure occurred by intergranular fracture. The (ST) orientation displayed the greatest

area fraction of fractured intermetallics and the smallest void density of secondary particles. From the SEM micrographs, it is evident that the large stringer particle groupings created favorable sites of void nucleation. Once the stringer particles were completely fractured, they coalesced through the grain boundaries (intergranular fracture) which caused the course precipitates to decohese and leave behind the small pit as shown in Fig. 2.10. A combination of both void impingement and void sheet mechanisms bypass the strengthening phases of the matrix (precipitates that impede dislocations) which leads to lower ductility. A summary of the damage mechanism for the (L), (LT) and (ST) orientation is presented in Table 2.3

Table 2.3 Experimental observation of the particle fracture relative to orientation.

	Long Dir	Long Trans Dir	Short Trans Dir
Void nucleation	Debonding and particle fracture of large intermetallics, debonding of small ppts	Particle fracture from large particles, debonding of small ppts	Fracture of particle stringers
Void growth	Dimples from two different length scale particles	Dimples from two different length scale particles	Small dimples from large stringers
Void coalescence	Void impingement	Void impingement	Void sheet
Fracture	Intragranular	Intergranular	Intergranular
Elongation to failure	Greatest	Middle	Least

Fig. 2.15 and 2.16 display the nucleation of small and large particles, respectively, as a function of effective initial particle size for both model and experimental results. As previously mentioned, we were only able to obtain the void density values from the post-

fracture state. While the model does not compare exactly to the experimental results due to the tortuosity of the fracture surface and the high rate of change near the end of the fracture process, the model compared well with the experimental nucleation values observed from the fracture surface. The lower rate of nucleation for the (ST) and (LT) compared to (L) correlates well to the post-failure metallography results presented in Table 2.2.

The main purpose of this work is to present a model that can capture the anisotropic plasticity and the related damage associated with different size scale particles. In terms of predicting failure of the DLT specimen, the model predicted the elongation of the three different orientations with good agreement. The results of the plasticity/damage modeling of the DLT specimen showed that the damage evolution was dominated by nucleation with only little void growth as compared to A356-T6 aluminum alloy (Horstemeyer *et al*., 2000), and as such, the damage parameters for the 7075-T651 aluminum alloy reflect this difference. As previously stated, the post-failure void number density quantified from the fracture surfaces provided the damage ratio caused by this bi-modal fracture process. However, this work's most important contribution is the approach of modeling the damage from particles of two different length scales. Thus, this approach could be used to model composites and other heterogeneous materials.

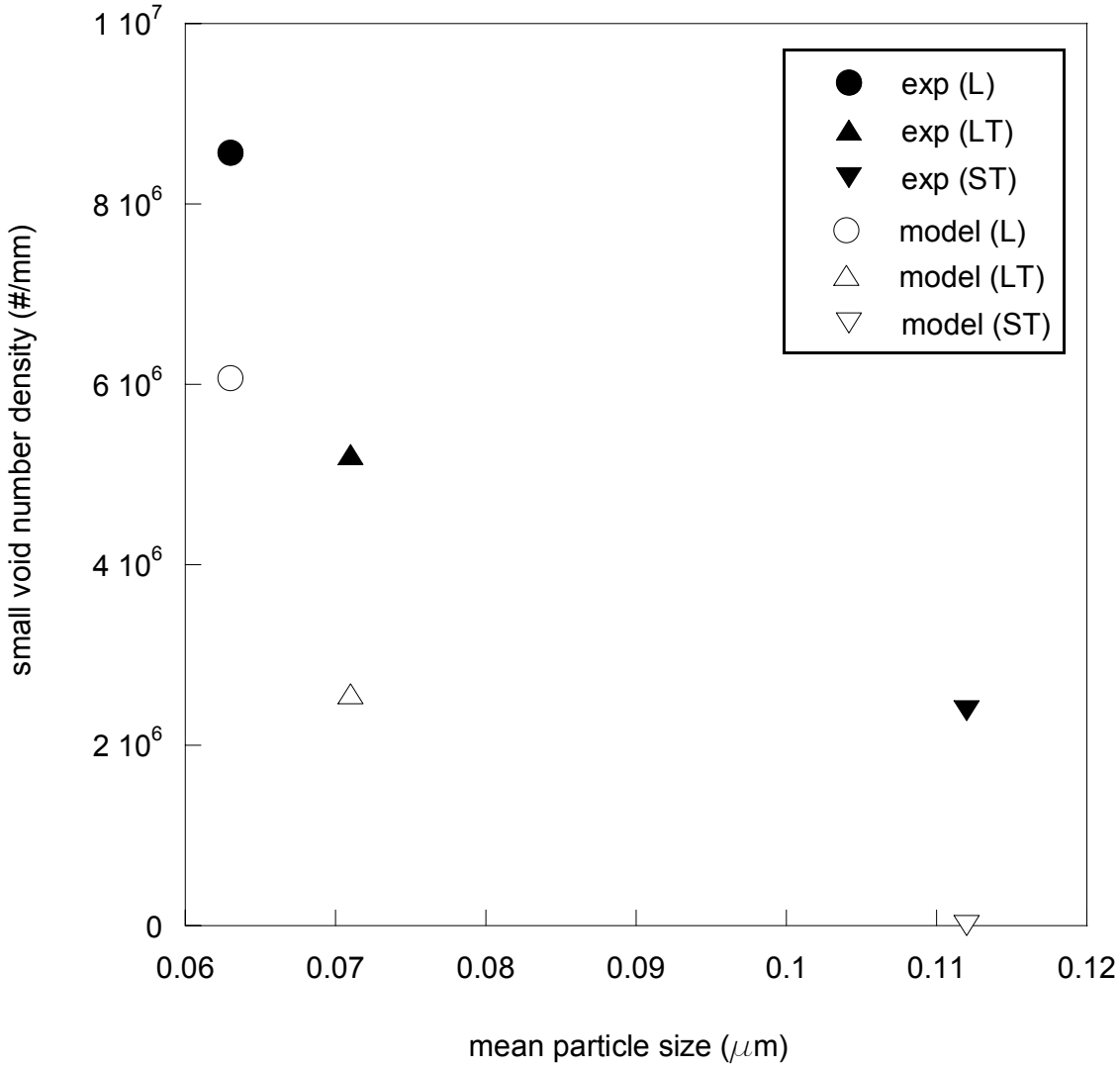

Figure 2.15 Comparing the internal state variable nucleation model results to the experimental results from the image analysis of the fracture surfaces for small void number density arising from precipitates.

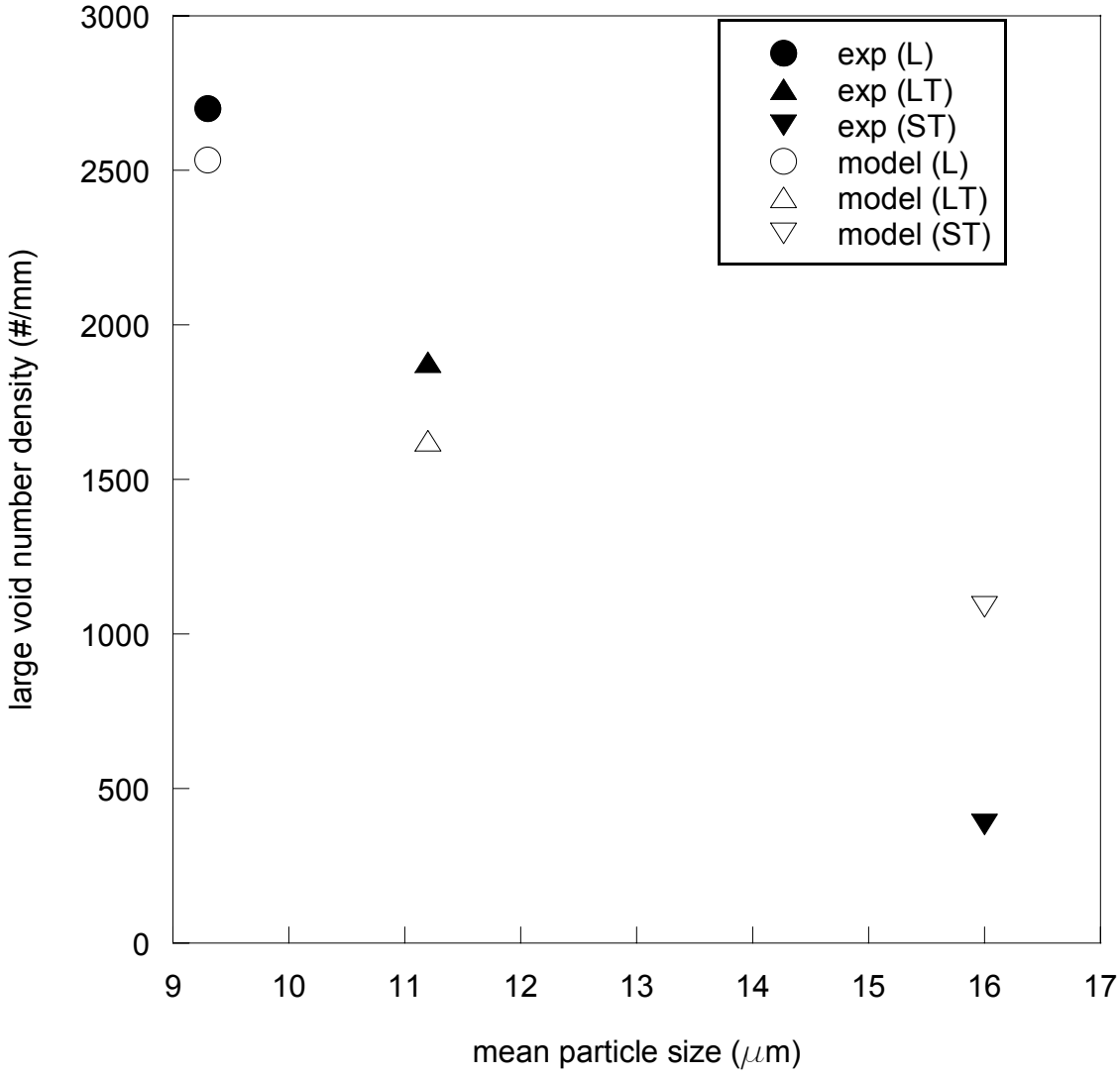

Figure 2.16 Comparing the internal state variable nucleation model results to the experimental results from the image analysis of the fracture surfaces for large void number density arising from the intermetallics.

Conclusions

The purpose of this work was to show that an internal state variable plasticity/damage model can capture the complex anisotropic stress-strain behavior and the associated bi-modal damage accumulation of a wrought aluminum alloy. The

internal state variable model constants were identical in the different directions related to yield, isotropic and kinematic hardening, void nucleation, void growth, and void coalescence with the only differences arising from the microstructural quantities of particle size and particle fraction. Optical micrographs and SEM images have further supported the conclusions that particle anisotropy is the major contributor to the varying ductility associated with the 7075-T651 aluminum alloy. The good correlation of the model to the experimental results, along with the post-failure microstructure analysis, have shown that a physically-motivated modeling approach is necessary to predict the damage arising from large intermetallics and smaller coarse precipitates.

CHAPTER III

MICROSTRUCTURAL INCLUSION INFLUENCE ON FATIGUE OF A CAST A356 ALUMINUM ALLOY

Introduction

Structural aluminum castings give a widely scattered distribution of fatigue data due to the variances of microstructures, defects, and inclusions present within the material. A widely used alloy is A356 aluminum in which the fatigue behavior was analyzed by Stephens *et al*. (1988). In an effort to link the microstructure with varying stages of crack growth of A356 aluminum, Fan *et al*. (2001), Gall et al. (1999, 2000, 2001), Horstemeyer (1998), and Horstemeyer and Gokhale (1999) performed micromechanical finite element simulations and microstructural analyses. Although a significant amount of the microstructure-property studies were focused upon porosity (void volume fraction) and/or silicon particle size, other aspects such as the synergism of the size effect of pores, nearest neighbor distances, number of pores, and void volume fraction (porosity) on the fatigue life had not been elucidated. The Dendrite Cell Size (DCS), which is related to the secondary dendrite arm spacing, has been a critical variable in fatigue life (Zhang *et al*., 1999; Lados and Apelin, 2003; Lados et al. 2005), while Major (1997) and Kumai *et al*. (1995) asserted it as the most dominate defect.

However, the DCS will be shown that it is not the only metric that should be used to relate to fatigue failure. The DCS is proportional to pore size as Major (1997) observed. Hence, pore size (Fan and Hao, 2004, Yi *et al*., 2006; Zhou *et al*., 2007) and porosity level (Bufiere *et al*., 2001; Yi *et al*., 2003, 2004, 2006; Zhou *et al*., 2007) have also been a focus of fatigue failure. However, the nearest neighbor distances, and number density of pores must also be considered along with second phase particles and oxides as well. A pore-controlled FDS map (Fan and Hao, 2004) showed that the relationship between controllable microstructural features such as largest pore size, stress amplitude, nearest neighbor distance and critical pore size can be related to cycles to failure. While these relationships are uniquely shown, DCS was not considered part of the map. Therefore, the contribution of this study is the emphasis of experimental observations relating these inclusions and their collective roles to the number of cycles until failure. The particular focus here is evidence observed by failed specimens using Scanning Electron Microscopy (SEM) along with microstructure-based fatigue modeling.

In trying to determine inclusion-property relations for fatigue, scatter must be considered in the modeling effort. Given the high levels of scatter in cast alloys, statistical methods are often employed. However, upon further examination of the microstructure-inclusion morphology present within a casting, a deterministic approach might well be in order first. The driving force for variability from inclusions can be separated, so a deterministic approach is plausible. From understanding of the deterministic cause-effect relations from the structure-property interactions, a stochastic model could be justified. In this study, the emphasis will be to show that the inclusion

relation to fatigue properties can be quantified from a deterministic frame of reference and is reflected in a model that can capture the statistical variance in the fatigue data.

This work will show that in modeling fatigue failure with different microstructure-inclusions, one should not just independently assign the final number of cycles to one parameter, for example, the pore size. Although one might examine just the pore size as the major inclusion for failure in one case, the other parameters/inclusions could play a much larger role in the outcome of the fatigue life for that particular specimen. Furthermore, other specimens may have experienced failure from an oxide which is consistent with observations made by Byczynski and Campbell (2005) and Wang *et al*. (2005).

Material and Methods

The A356 aluminum alloy cast plates were comprised mainly of an age hardenable aluminum matrix with silicon particles in the eutectic region. The aluminum alloy comprised of 7% Si, 0.4% Mg, 0.01% Fe, 0.01% Cu, 0.01% Mn, 0.01% Sr, 0.01% Ti, and 0.01% Zn. One type of plate was vertically cast after the method of Major (1997) in order to quantify the different initial porosity levels and DCS levels. Another type of plate was horizontally cast in order to give uniform microstructure and properties.

Horizontally Cast Plates

The horizontally cast plate dimensions were 20 cm by 14 cm by 5 cm and were cast in iron chill molds on the top, bottom, and end of the casting cavity to simulate a

permanent mold (not made by the method of Major, 1997). A no-bake silica sand was used to create the sides of the plate, the riser, and the down sprue. A ceramic foam filter was used between the down sprue and the riser. A356.2 ingot was melted in an induction furnace. The melt was grain refined with titanium-boron, strontium modified, and degassed using a rotary degasser. The castings were poured between 950 K and 977 K, and then cooled over a 16 hour period. The plates were removed from the mold and then heat treated to a T6 temper (solutionized at 810.8 K for 16 hrs, quenched in hot water at 344 K, and then aged for 4 hours at 427.4 K). The microstructure contained aluminum rich dendrite cells, equiaxed fine silicon particles distributed in the interdendritic regions, and sub-micron intermetallics.

Vertically Cast Plates

The vertically cast plates were produced using an end-chilled molding system comprising a resin bonded silica-sand mold that included a standard side gating system. The main mold cavity defining the plate itself was open at the bottom and the mold was set onto a heavily water cooled copper chill box which defined the bottom of the mold cavity. The A356.2 material was alloyed in an induction furnace and then transferred to an electrical resistance furnace where it was cleaned and degassed using a spinning nozzle degasser running Ar-10%Cl for fluxing, followed by pure Ar for degassing. During the degassing cycle both a 5%Ti-1%B grain refining master alloy addition and an Al-10%Sr modifying master alloy addition were made. The holding and pouring temperature was maintained in the 995 to 1015K range. The resultant plates were then

heat treated to the T61 temper. The first step was a 4 hour solution time at a temperature of 813K, followed by a 338K hot water quench. The plates were then naturally aged at room temperature for 12 hours followed by an artificial age at 428K. As a result of this casting and heat treatment, the vertically cast plates contained a range of dendrite arm spacings as a function of the distance from the chill. Samples with any desired secondary dendrite arm spacing could be machined from them simply by choosing the correct location. Porosity could also be systematically varied from plate to plate, independently of the solidification time, by varying the degassing time and residual hydrogen content.

Experiments

The specimens used for the testing were ASTM-E606 low cycle fatigue specimens with an outside diameter of 9.525 mm. They were tested at 5 Hz frequency, at an R-ratio of -1, and a strain amplitude of 0.0015. A servohydraulic Instron test frame was used to cycle the specimens under displacement control.

Fractography and Mechanical Behavior

Fig. 3.1 shows the strain-life curves from the horizontally and vertically cast plates. Note that as the DCS increased, the number of cycles (reversals) to failure decreased. Although one might be tempted to attribute the differences just to DCS, an attempt was made to distinguish the effects as a function of different microstructural inclusions. As such, many of the strain-life specimens were analyzed under SEM and

Energy Dispersive x-ray Spectoscopy (EDS) to quantify the size and type of the fatigue crack initiation site. Parameters of interest shown in Table 3.1 were the microstructural inclusion type, (in this study the term “inclusion” is employed to represent pore, oxide, silicon particle, or intermetallic), size, distance to free edge, volume fraction, and nearest neighbor distance. The nearest neighbor distance was calculated from the area of the cross section divided by the number of pores. When more than one pore was present, an average was taken to determine the pore (“inclusion”) size.

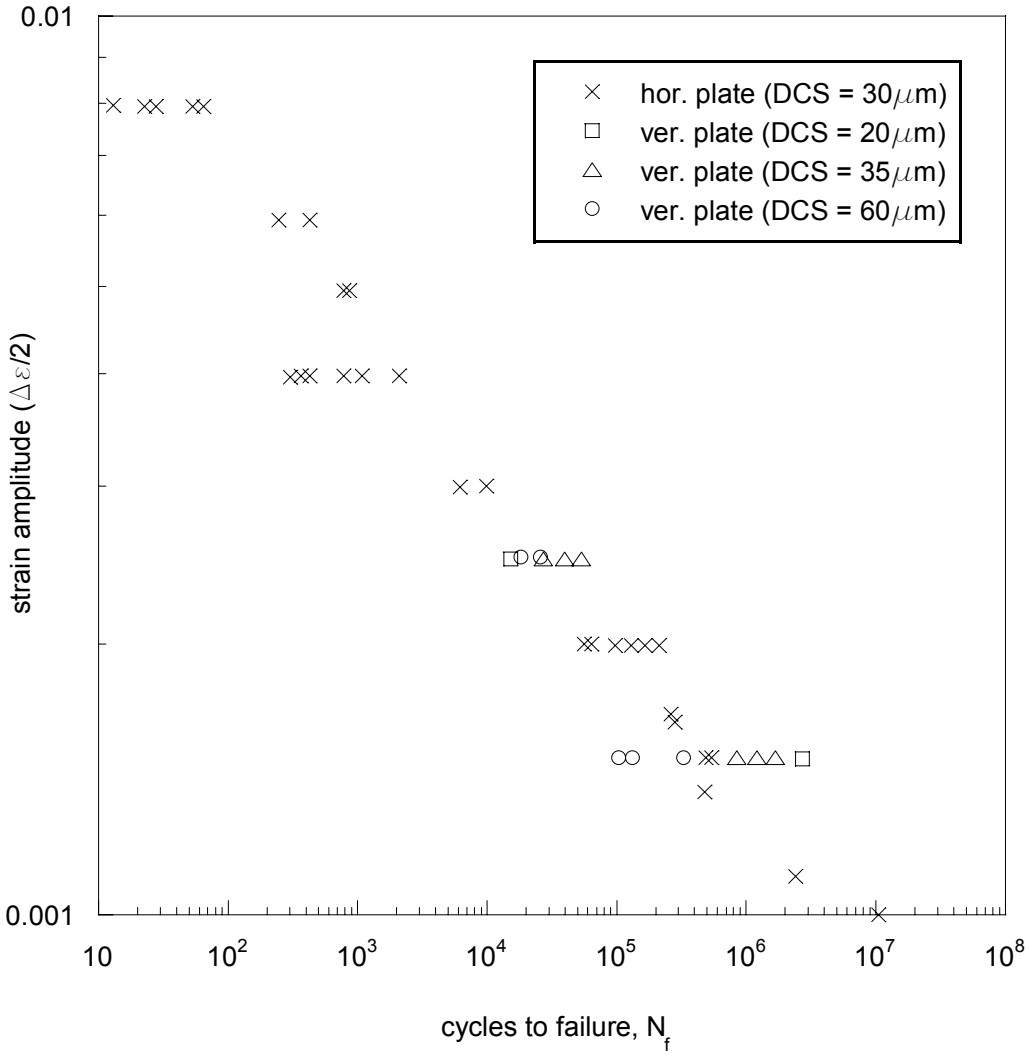

Figure 3.1 Strain-life curves from horizontally and vertically cast plates

Table 3.1 SEM results from specimens that had experienced a constant strain fatigue amplitude (R=-1) from the vertically cast A356 plate.

DCS (μm)	Cycles	Strain (%)	Inclusion Type	Inclusion Size (μm)	Porosity vol. fraction	Nearest neighbor distance
60	451,000	0.15	13 pores	265	0.0083	488
60	512,000	0.15	11 pores	255	0.0107	577
60	724,000	0.15	10 pores	250	0.0121	635
60	961,000	0.15	9 pores	240	0.0248	705
35	1,030,000	0.15	13 pores	140	0.005	488
35	1,120,000	0.15	17 pores	117	0.0059	373
35	1,140,000	0.15	12 pores	175	0.0075	529
20	1,620,000	0.15	15 pores	108	0.0019	423
20	2,070,000	0.15	8 pores	90	0.0020	794
20	1,210,000	0.15	14 pores	124	0.0048	453
20	3,210,000	0.15	15 pores	96	0.0063	423

In some castings with no pores or oxides visible, nucleation sites were determined to be less than a micron in size. Alternatively, when many pores were present, fatigue cracks nucleated at the large pores or at several pores. As illustrative examples of the size effects and different microstructural inclusions initiating fatigue failure, three specimens with a different number of cycles to failure are shown in Fig. 3.2-5. Fig. 3.2 shows a specimen that had over 1.7×10^6 cycles in which an oxide was found on the order of 5 μm. Fig. 3.3 shows a fairly large pore (150 μm) near the edge of the specimen in which the fatigue life was approximately 2.05×10^5 cycles. This specimen experienced a lesser number of cycles to failure because of the initial inclusion size was larger (150 μm) compared to less than 5 μm although the type was different, pore versus oxide, respectively. Fig. 3.4 shows a specimen that had over 5.12×10^5 cycles in which multiple interior pores ($\geq$200 μm) were found with a fairly large volume fraction of pores. When comparing the fatigue failure for specimens in Fig. 3.3 and 3.4, the fatigue life was

slightly more in Fig. 3.4 although the pore size was greater (<200 μm vs 150 μm). Furthermore, the total void volume fraction in the specimen in Fig. 3.4 is much greater than that in Fig. 3.3. As such, one might expect a lesser fatigue life for that specimen. However, another parameter, the distance to the specimen edge plays a more dominant role. McDowell et al. (2003) and Fan et al. (2003) summarized the deleterious effects on fatigue life as the inclusion is closer to the free surface. Although total void volume fraction and inclusion size play a strong role in the total fatigue life, the distance to the surface edge plays a bit stronger role when comparing the two particular specimens in Fig. 3.3 and 3.4.

Fig. 3.2-4 illustrate how different microstructural inclusions affect the fatigue life. Fatigue striations were observed locally near all of the microstructural inclusions in Fig. 3.2-4, but after a certain distance, striation differences (not shown here) arose in the samples with different microstructural inclusion types. For example, the specimens in Fig. 3.2-3 showed fatigue striations to a fairly large distance away from the nucleation site in comparison to the specimen in Fig. 3.4, which had a larger volume fraction of porosity. On the fracture surface of the specimen in Fig. 3.4, the fatigue cracks grew from the pores, and then they coalesced in a ductile fashion. Fig. 3.5a shows a close-up of Fig. 3.4 designated by casting pores "a" and "b". Fig. 3.5b is a secondary electron image (SEI) at higher magnification to illustrate the fatigue striations near pore “a”. Fig. 3.5c shows a region between two pores illustrating the ductile region where voids and broken silicon particles are observed.

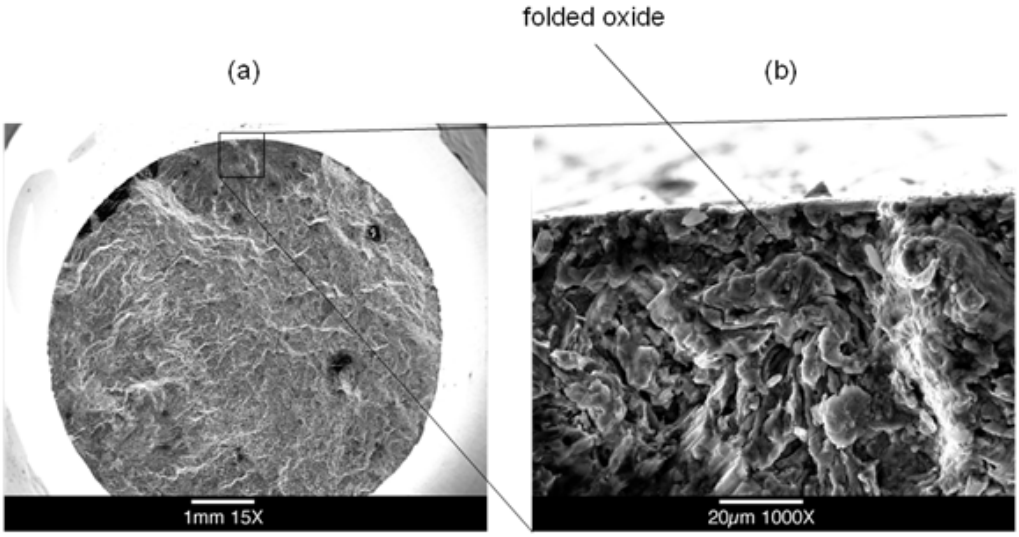

Figure 3.2 SEM pictures at (a) 15x and (b) 1000x of specimen tested under uniaxial fatigue at a strain amplitude of 0.0015 with an R-ratio of –1. This specimen ran for 1.7×10^6 cycles with the initiation site being a folded oxide film that was less than 5 microns.

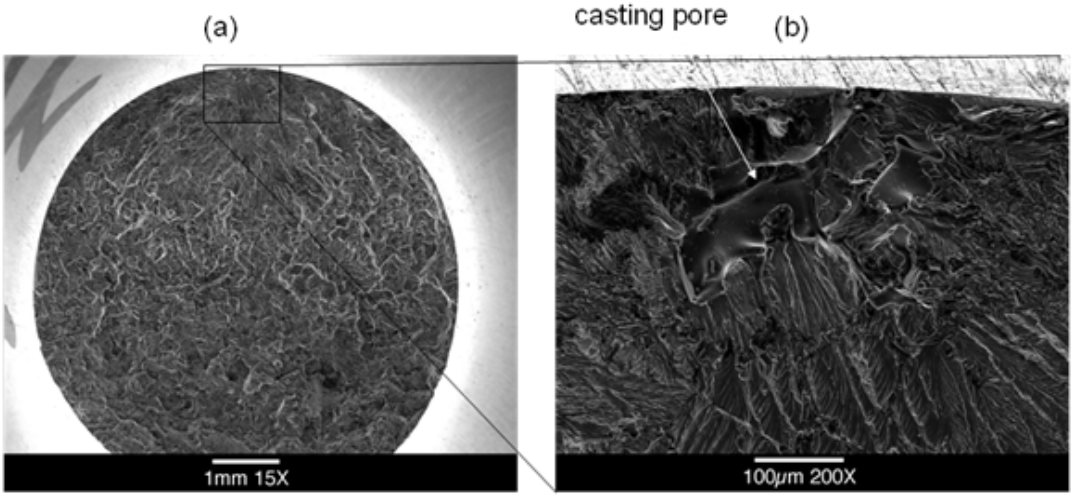

Figure 3.3 SEM pictures at (a) 15x and (b) 200x of specimen tested under uniaxial fatigue at a strain amplitude of 0.0015 with an R-ratio of –1. This specimen ran for 2.05×10^5 cycles illustrating the degrading effect of the 150 micron size casting pore.

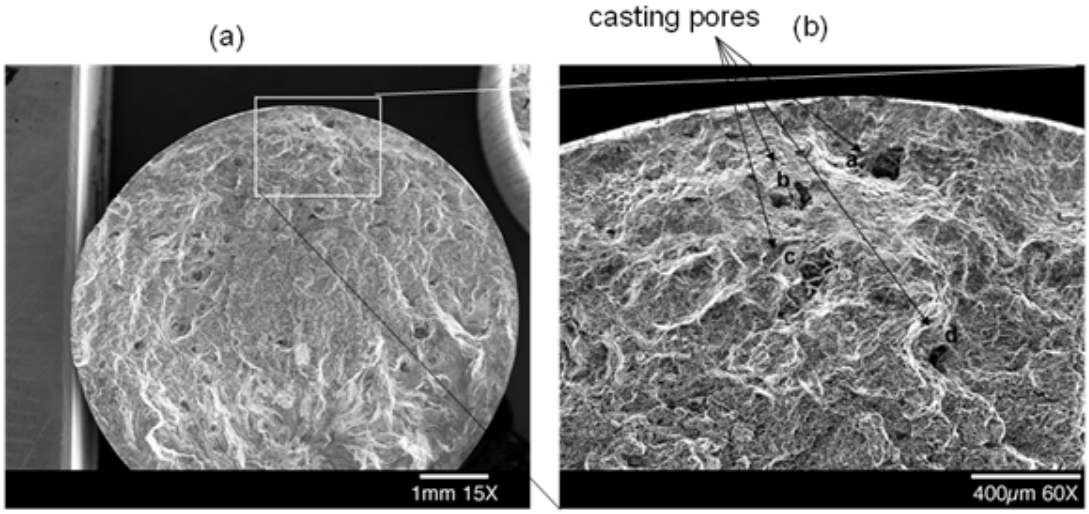

Figure 3.4 SEM pictures at (a) 15x and (b) 60x of specimen tested under uniaxial fatigue at a strain amplitude of 0.0015 with an R-ratio of –1. This specimen ran for 5.12×10^5 cycles illustrating the degrading effect of multiple casting pores in locations a, b, c, and d as shown in Illustration (b).

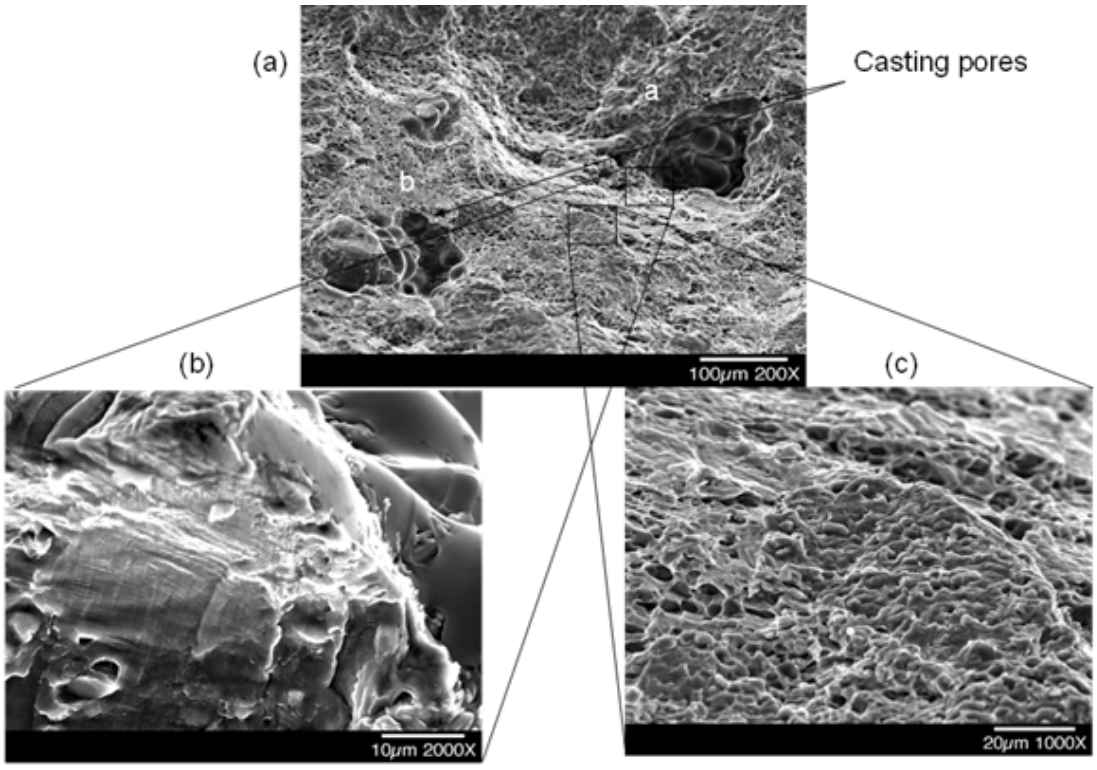

Figure 3.5 SEM pictures at (a) at 200x showing casting pores a and b, (b) at 2000x in casting pore a, and (c) location b at 1000x of specimen tested under uniaxial fatigue at a strain amplitude of 0.0015 with an R-ratio of –1. These images are zoomed in from Figure 3.4.

Fatigue Model

The basis for the MultiStage Fatigue Model (MSF) first employed by McDowell *et al*. (2003) was initially founded upon multiscale finite element simulations. More recent use of the MSF model (Xue *et al*., 2007) demonstrated the need for a multistage approach for modeling wrought aluminum alloys. The governing equations in the multistage fatigue model are:

$$N_{TOTAL} = N_{INC} + N_{MS/PSC} + N_{LC} \tag{3.1}$$

$$C_{inc}N_{inc}^{\alpha}=\beta=\frac{\Delta\gamma_{\max}^{P*}}{2} \tag{3.2}$$

$$\beta=\frac{\Delta\gamma_{\max}^{P*}}{2}=\left(\frac{PS^2}{(NND)(DCS)}\right)y_1(1+R)y_2\left(\varepsilon_a-\varepsilon_{th}\right)^q, \quad \frac{l}{D}<\eta_{\lim} \tag{3.3}$$

$$\beta=\frac{\Delta\gamma_{\max}^{P*}}{2}=\left(\frac{MPS^2}{(NND)(DCS)}\right)y_1(1+R)y_2\left(1+\xi\frac{l}{D}\right)\left(\varepsilon_a-\varepsilon_{th}\right)^q, \quad \frac{l}{D}>\eta_{\lim} \tag{3.4}$$

$$\frac{l}{D}=\eta_{\lim}\frac{\left(\hat{\varepsilon}_a-\varepsilon_{th}\right)}{\left(\varepsilon_{per}-\varepsilon_{th}\right)}, \quad \frac{l}{D}\le\eta_{\lim} \tag{3.5}$$

$$\frac{l}{D}=1-(1-\eta_{\lim})\frac{\left(\varepsilon_{per}\right)^r}{\left(\hat{\varepsilon}_a\right)}, \quad \frac{l}{D}>\eta_{\lim} \tag{3.6}$$

$$\left(\frac{da}{dN}\right)_{msc}=\chi\left(\Delta CTD-\Delta CTD_{th}\right) \tag{3.7}$$

$$_{\Delta CTD}=C_{II}\left(\frac{MPS^2}{(NND)(DCS)}\right)\left[\frac{U\Delta\hat{\sigma}}{S_{ut}}\right]^{\zeta}a+C_I\left(\frac{MPS^2}{(NND)(DCS)}\right)'\left(\left.\frac{\Delta\gamma_{\max}^{p}}{2}\right|_{macro}\right)^2 \tag{3.8}$$

$$\left(\frac{da}{dN}\right)_{LC}=A\left(\left(\Delta K_{eff}\right)^m-\left(\Delta K_{eff,th}\right)^m\right) \tag{3.9}$$

$$\frac{da}{dN}=\max\left[\left(\frac{da}{dN}\right)_{msc},\left(\frac{da}{dN}\right)_{LC}\right] \tag{3.10}$$

The total fatigue life (Equation 3.1) comprises incubation, microstructurally small/ physically small crack growth, and long crack growth. Equation (3.2) is employed to model the incubation life due to cyclic plastic deformation from micronotches and is

based on a modified Coffin-Manson law that links microplasticity to incubation life. As in the Coffin-Manson law, α is selected and is identical to the macroscopic Coffin-Manson law and $C_{inc} = C_n + z(C_m - C_n)$, where $C_n = 0.24(1 - \langle R \rangle)$, R is the load ratio, C_m is a model constant, and z is a variable related to the plastic zone size. The $\beta = \frac{\Delta\gamma^{P*}_{\max}}{2}$ term in Equation (3.3) and (3.4) is the nonlocal maximum plastic shear strain amplitude located around the particle or defect and depends on the nominal ratio of the plastic zone to the particle size or defect (l/D). The parameters ε_{th}, ε_{per}, η_{lim}, and q, are used to describe the ratio of the plastic zone to the particle size as a function of applied strain amplitude ($\hat{\varepsilon}_a$). The parameter Y is used to capture the load ratio effects and is correlated as $Y = y_1 + (1+R)y_2$, where y_1 and y_2 are model constants, and R is the load ratio. MPS is the maximum pore size, NND is the nearest neighbor distance, and DCS is the dendrite cell size, where the above constants are microstructural parameters determined from fracture surface analysis. The MSC/PSC growth is a function of the crack tip displacement (Equation 3.7) and describes the crack growth regime, where ΔCTD is the crack tip displacement range, χ is a material constant, and ΔCTD_{th} is the threshold for crack tip displacement. The crack tip displacement, shown in Equation (3.8), is a function of remote loading where C_I, C_{II}, and ζ are constants based on small crack growth experiments. The long crack growth behavior is presented in Equation (3.9) and is based a modified Paris law. The effective stress intensity factor is defined as $\Delta K_{eff} = K_{max} - K_{op}$, where K_{max} is the maximum stress intensity factor, and K_{op} is the opening

stress intensity factor. Finally, the higher rate of growth between the small crack and long crack calculated growth rates is used for the transition between MSC and LC regimes for constant amplitude fatigue life predictions (Equation 3.10).

Note in the incubation law in Equation (3.3) and the MSC growth law in Equation (3.8) that the term $MPS^2/(NND*DCS)$ is employed. This is a modeling contribution in this research which modifies the works of McDowell *et al*. (2003) and Xue *et al*. (2007). Experimental fracture surface results and strain-life curves were used to motivate this form of the equations as shown next.

Analysis and Discussion

One main emphasis of this writing is to show that the DCS is not a robust metric for correlation to fatigue life. Major (1997) performed a quantitative experimental study using the DCS as a metric to evaluate the fatigue life of this cast A356-T6 aluminum alloy. Interestingly, the data in Table 3.1 shows that the porosity (void volume fraction) and pore size is often correlated to the DCS. It certainly may be true that the DCS is a length scale related to fatigue life since it represents a boundary to dislocations much like a grain boundary, but it is clouded by the direct link to the porosity volume fraction which is related to the number density of pores and nearest neighbor distances. Fig. 3.6 shows a plot of the number of cycles versus inclusion size for different DCSs in order to show the interactive effects. Included in this figure are data from Major *et al*. (1997) and Zhang *et al*. (1999), who performed similar studies but not down to the size scale that

was performed here. Here, the trend is not obvious regarding the DCS but the size of the inclusion is clear until a certain volume fraction of porosity is reached.

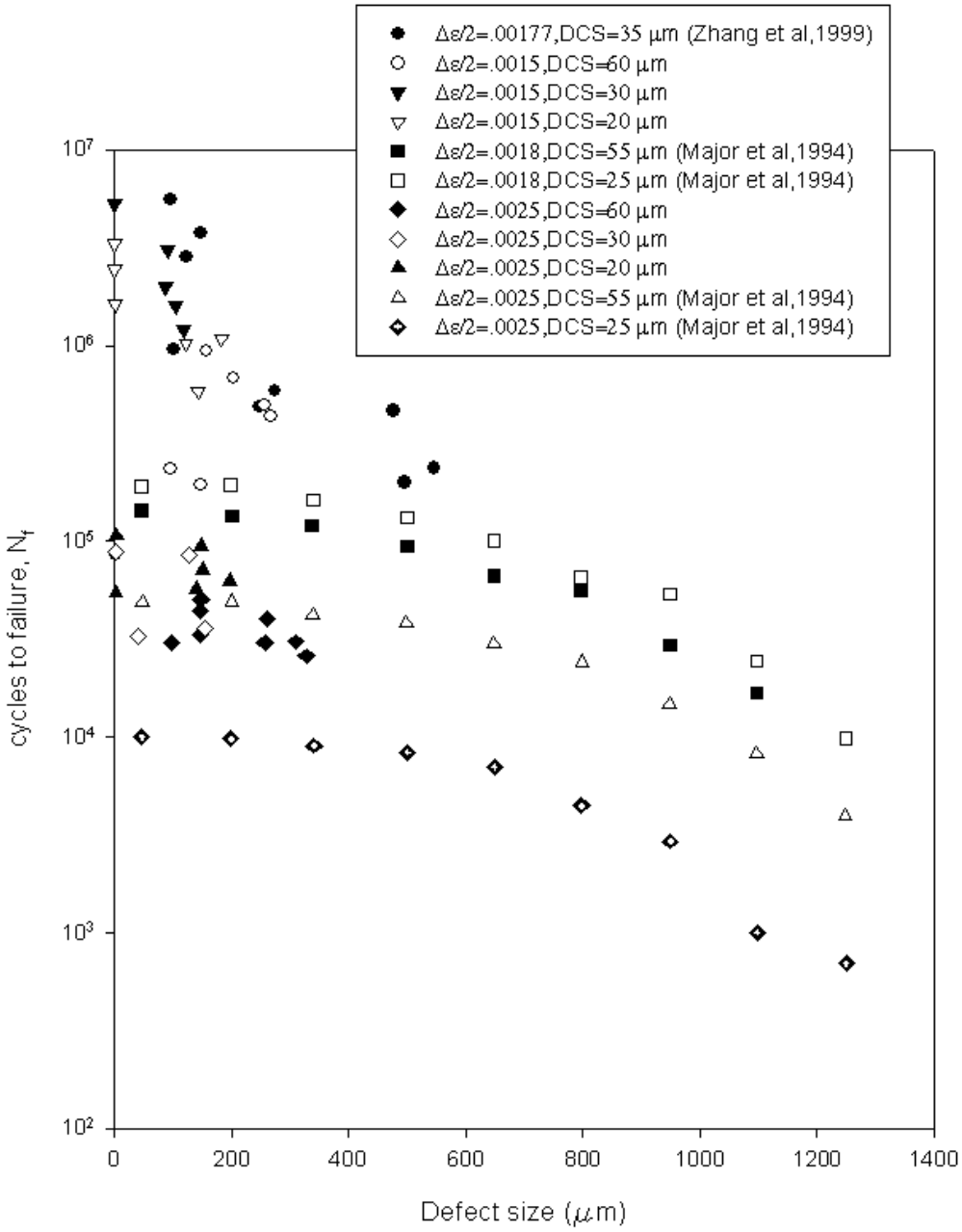

Figure 3.6 Number of cycles versus defect size at different dendrite cell sizes for the vertically cast plate and literature data.

Fig. 3.6 also illustrates that most of Major's data included microstructural inclusions that were only pores and most of them larger than 200 μm. When adding in the Zhang et al. (1999) data and the data within this work, a nonlinear relation is clearly seen that has curvature of opposite sign than that above 200 μm. The data from Major (1997) does not show this trend, because he did not observe other microstructural inclusions in his study below 200 μm. The additional data provided in this study with that of Zhang *et al*. (1999) illustrates that other mechanisms can dominate as the inclusion size decreases causing this nonlinear relation with opposite curvature as illustrated in Fig. 3.6, which was confirmed by fractography of all of the specimens in the study.

Fig. 3.7 shows just the maximum pore size versus the number of cycles (from Table 3.1) to give insight into the relation of the driving force for fatigue crack growth. Clearly, Fig. 3.7 shows that fatigue life degrades exponentially as the pore size increases. As mentioned before, DCS is used in practice to help casting designers assess the viability of a component. However, the DCS is shown to not to be the main driving force for fatigue failure but in fact the pore size is. It is just serendipitous that the DCS correlates with the maximum pore size usually attributed to gas pores. The pore size is related to the DCS, because they form at the end of the solidification process around the dendrite circumferences.

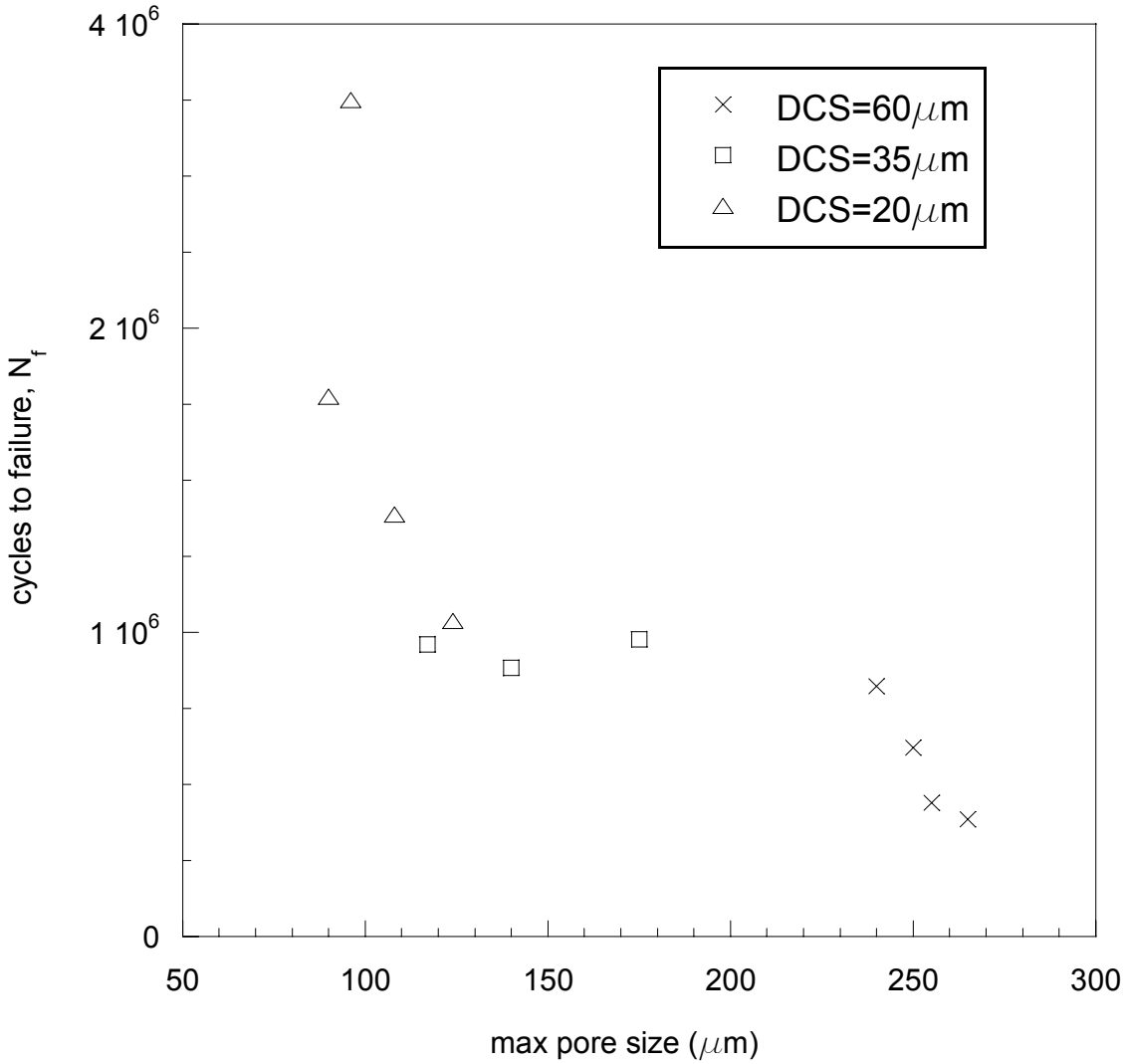

Figure 3.7 Number of cycles versus maximum pore size (micron) measured for specimens tested at a strain amplitude of 0.0015.

The previous arguments were mainly based on size effects of the microstructural inclusion. Another parameter not generally considered is the nearest neighbor distance. Fig. 3.8 shows that as the nearest neighbor distance increases, the fatigue life increases. In a casting, pores are distributed throughout a component. Moreover, shrinkage has very

close neighboring pores. When pores are close enough, their local stress field may affect the neighboring void if it lies within the field. The coupled stress field effect arising from close neighboring voids can enhance the crack driving force and thus reduce the fatigue life. Figure 8 indicates that this is true.

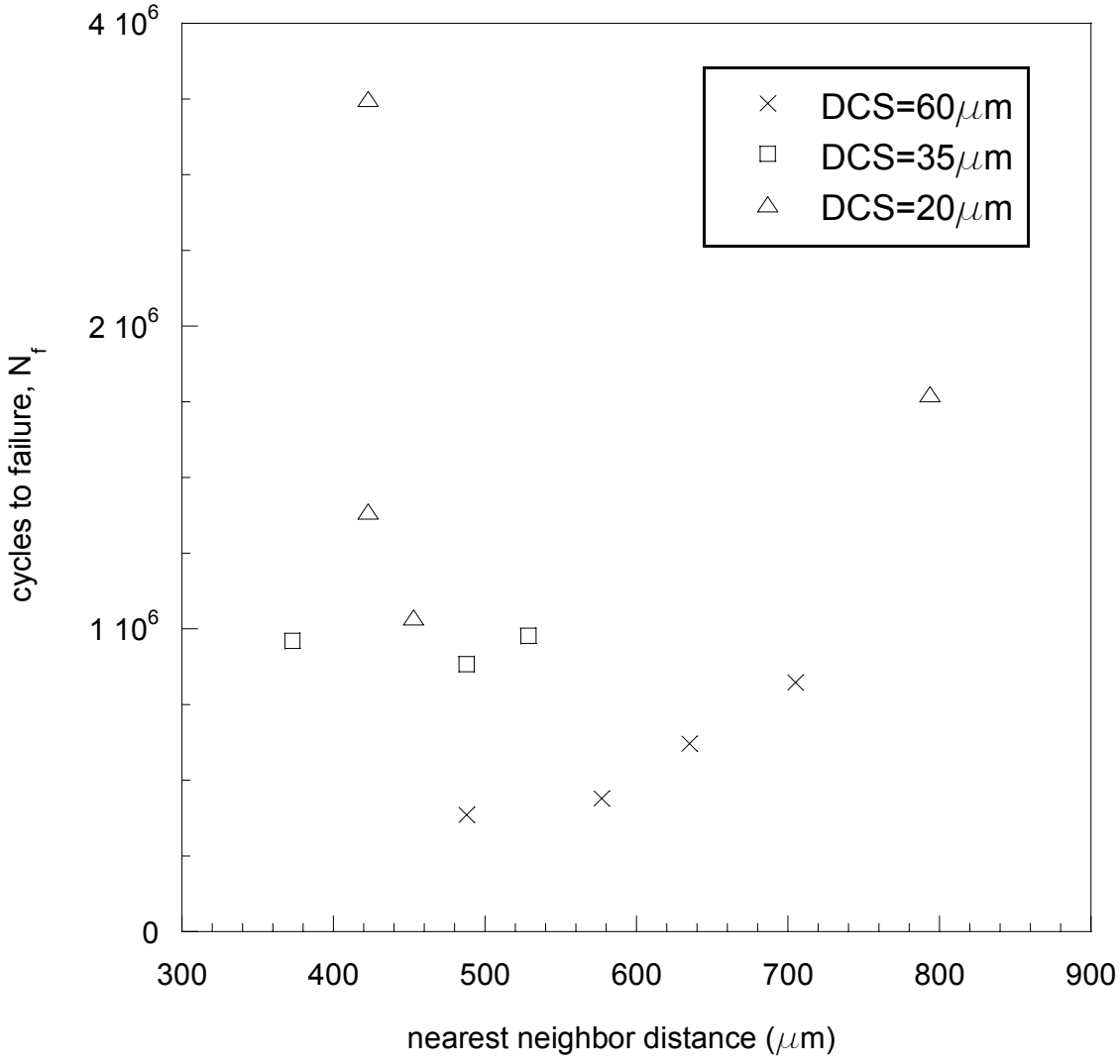

Figure 3.8 Number of cycles versus nearest neighbor distance (microns) measured for specimens tested at a strain amplitude of 0.0015.

Another important parameter besides the pore sizes and nearest neighbor distance is the number density of inclusions. In monotonic conditions the number density of inclusions is related to the nucleation of new cracks/voids (cf., Horstemeyer *et al*., 1999). In this study, the number of inclusions (most of which were pores) on the fracture surfaces were counted and the results are shown in Fig. 3.9. One would expect that as the number of pores increased the fatigue life decreased. However, this was not observed clearly suggesting that number density should not be included as a metric for evaluation fatigue damage.

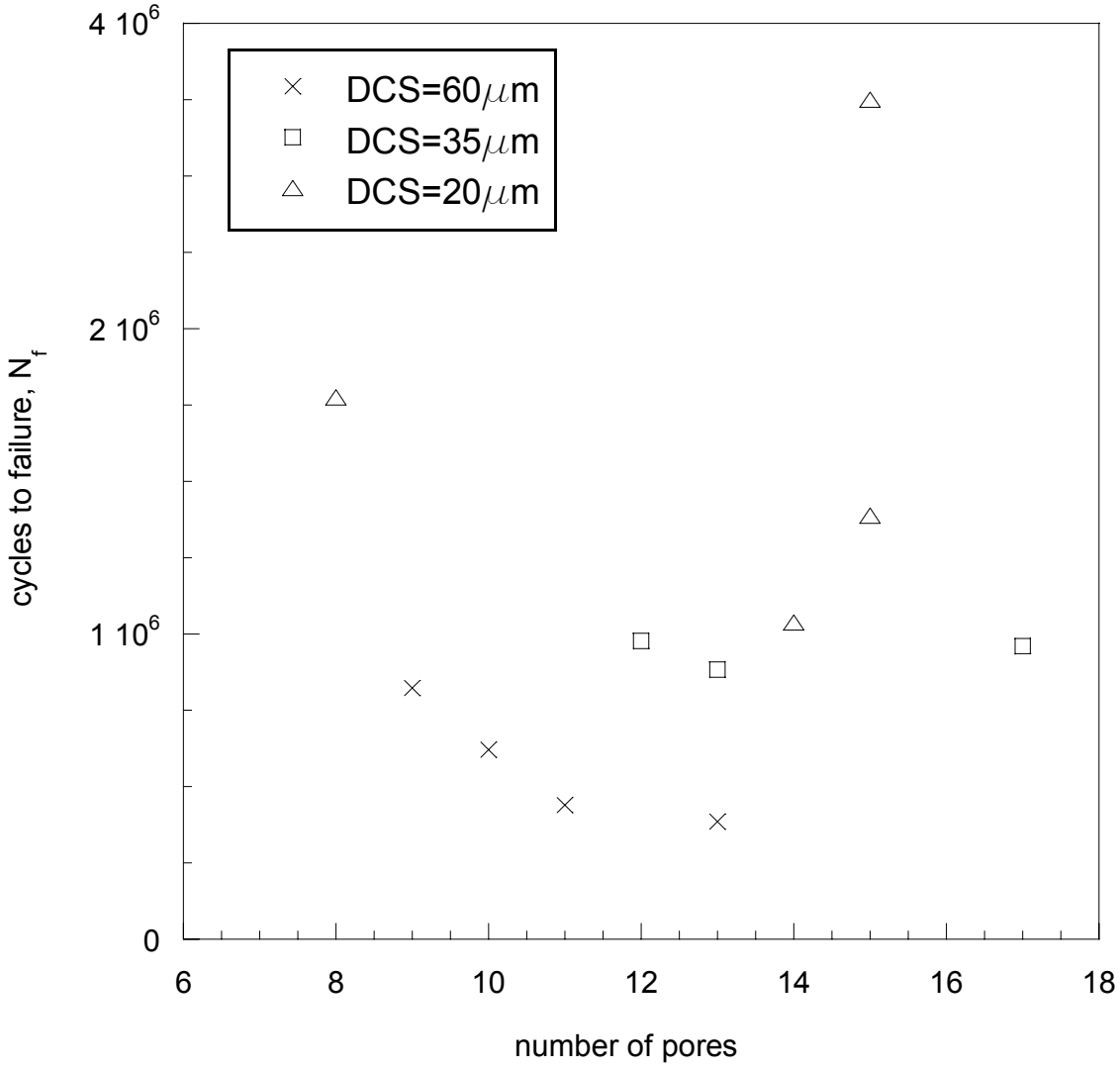

Figure 3.9 Number of cycles versus number of pores measured for specimens tested at a strain amplitude of 0.0015.

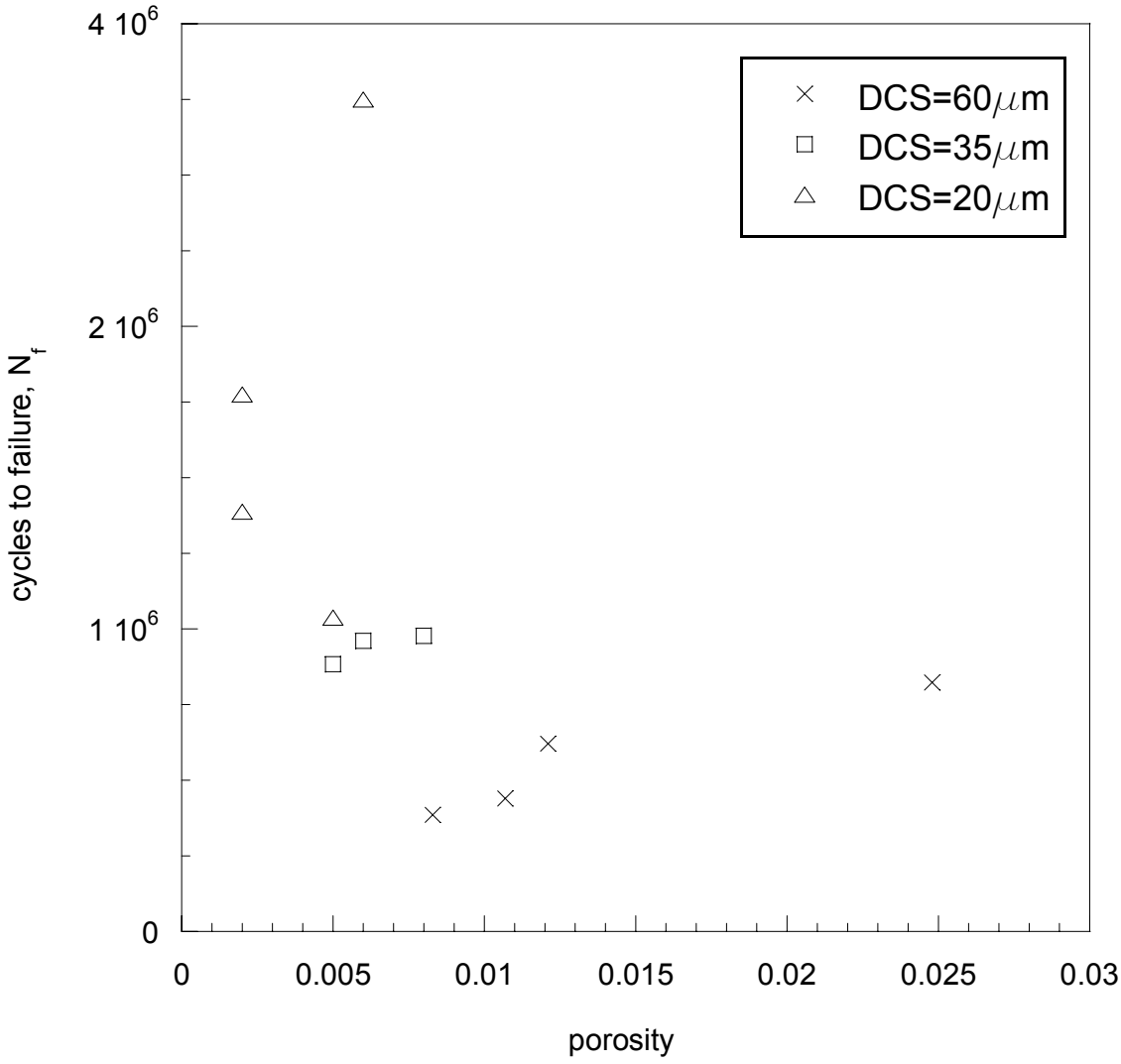

Figure 3.10 Number of cycles versus porosity (void volume fraction) measured for specimens tested at a strain amplitude of 0.0015.

The final parameter examined in the context of metrics for use in fatigue damage assessment is the porosity (void volume fraction). Fig. 3.10 shows the number of cycles versus porosity volume fraction for the case when the strain amplitude was 0.0015. The maximum pore sizes counted earlier are related to what is here termed "casting pores,"

but the porosity is often attributed to shrinkage, which are very small pores distributed in close regions within the material, and the large casting pores. Fig. 3.10 shows the fatigue life versus the porosity for the specimens observed in this study. No clear trend can be observed in Fig. 3.10, probably because the casting pores were observed in almost all of the specimens. However, one can imagine from the trends that as the porosity increased, the fatigue life decreased. Further studies that would be useful would be to reduce the casting pores such that only shrinkage would be present. In this way, one could distinguish between the effects of the porosity levels to a better degree.

In trying to determine the inclusion-property relations with the most pertinent defects, one can nondimensionalize the deleterious entities. The first of the two nondimensionalized parameters is the maximum pore size normalized by the nearest neighbor distance. A second nondimensionalized parameter is the maximum pore size normalized by the dendrite cell spacing. When these two nondimensionalized parameters are combined into the incubation equation (3.3) and microstructurally small crack growth equation (3.8) and are plotted with respect to fatigue life, one can see in Fig. 3.11 that a clear nonlinear relationship arises. This behavior, as illustrated in Fig. 3.11, combines the main aspects of the strongest inclusion parameters in the study to fatigue life. Note that as the life increased, the scatter in the data increased. As such, one would expect more scatter in high cycle fatigue when compared to low cycle fatigue as is observed in general. These microstructure-property data clearly demonstrate the cause-effect relations of the scatter in fatigue data.

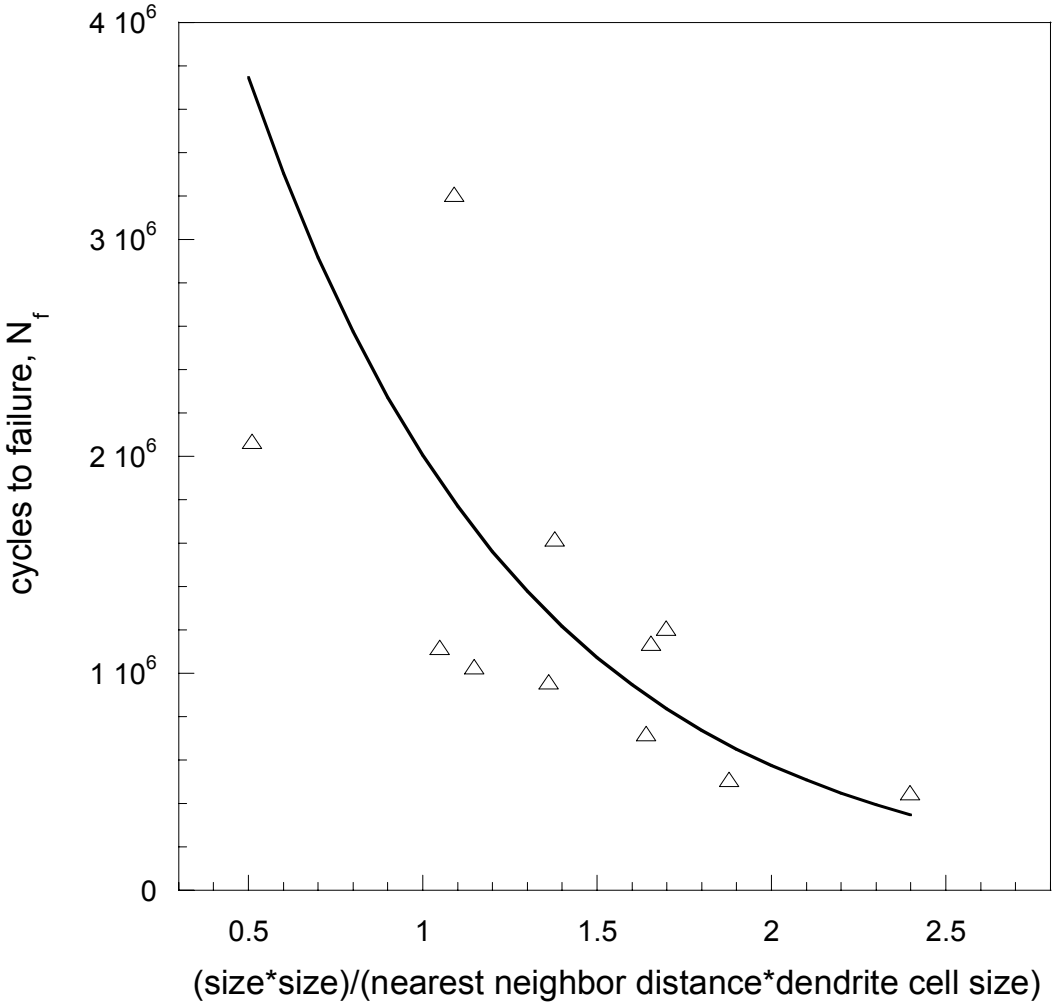

Figure 3.11 Number of cycles versus (pore size*pore size)/(nearest neighbor distance*dendrite cell size) measured for specimens tested at a strain amplitude of 0.0015.

This quantification of the structure-property relations can also be used for fatigue modeling. As such, this nondimensionalized entity was implemented into both the incubation and MSC/PSC equations of the MSF model (See Appendix B for model constants). For the incubation life, the nondimensionalized term was employed to magnify the maximum plastic shear strain amplitude around the "inclusion" where the

inclusion can be a constituent intermetallic particle, oxide film, or pore. This addition to the model appears reasonable since local shear strain at the inclusion was influenced by neighboring inclusions, pore size and the surrounding dendrite cell size. Once a crack is incubated, the growth rate of the MSC/PSC was also influenced by the local stress field that is altered by the aforementioned deleterious entities. The results of these changes to the MSF model allow a deterministic approach that achieves good agreement in predicting the scatter in the fatigue data. Fig. 3.12 displays the data presented in Fig. 3.1 along with the MSF model for the upper and lower bounds of the nondimensionalized term. The upper and lower bounds of the model represent the extreme deleterious effect of the maximum pore size, nearest neighbor distance, and dendrite cell size and correlate well to the experimental data.

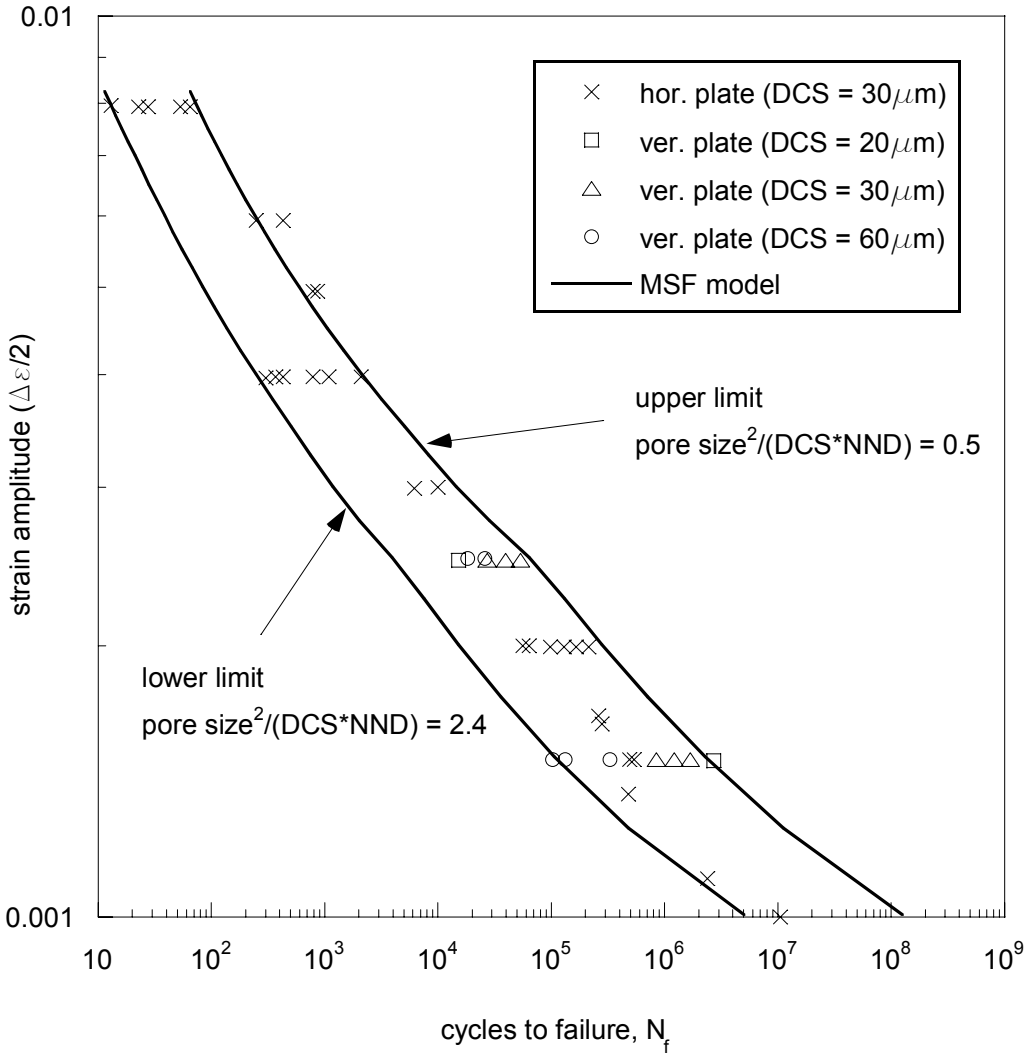

Figure 3.12 Strain-life curves from horizontally and vertically cast plates with the upper and lower bound of the MultiStage Fatigue model predictions

Conclusions

Inclusion quantification has been performed on a cast A356 aluminum alloy related to the fatigue properties under high cycle uniaxial conditions. The trend for industry to use the dendrite cell size as the main metric only for evaluating fatigue life that has been shown to be serendipitous with the actual cause: mainly the maximum pore

size, secondarily the nearest neighbor distance, and finally the porosity. The dendrite cell size can be used to normalize the effects of the various inclusion features as shown in this writing due to the boundary causing dislocation build-up and/or dislocation nucleation. Scanning Electron Microscopy was used on a multitude of specimens in order to quantify the inclusion-property relations. As such, the microstructural inclusion effect on fatigue life shows a confounding influence of several parameters, not just the DCS. The nondimensional term of that includes the combination of maximum pore size, nearest neighbor distance, and DCS was implemented into the incubation and MSC/PSC formulation of the MSF model and correlated well to experiments.

CHAPTER IV

MICROSTRUCTURALLY SMALL FATIGUE CRACK GROWTH OF 7075-T651 ALUMINUM ALLOY

Introduction

Fatigue is essentially a driving force versus resistance in a given material. Clearly, at different length scales various "resistances" exist that can alter the failure path and crack growth rates. Some microstructural features include grain size, particle size, particle volume fraction, misorientation of grain boundaries, and crystallographic orientation of grains. Once a fatigue crack meanders through this maze of resistances, it can reach a level where the resistance is minimal compared to the driving force. At this point, a transition is made from a small crack to a long crack.

Attempts to correlate small cracks to long cracks in terms of da/dN for ΔK have led to a so-called small crack anomaly. Some possible explanations to the small crack problem have been attributed to plasticity-induced closure transients, roughness induced closure, microstructural interaction, violation of LEFM and EPFM, and mixed mode effects (McDowell, 1997). It is important to note that it has been argued that the calculation of the ΔK concept and its use (cf., Schijve, 1984; McDowell, 1997) may not be appropriate for small cracks. Possibly a more appropriate driving force parameter in

characterizing the growth of small cracks is crack tip displacements (CTD). Despite this ongoing debate, work using the ΔK concept has been proven successful in modeling the growth of small fatigue cracks (cf., Lankford, 1982, 1983; Newman and Edwards, 1988; Edwards and Newman, 1990; Newman *et al*., 1994).

Pearson (1975) was the first to report on the faster growth rates of small fatigue cracks by showing that these smaller cracks grew much faster than long cracks at the same ΔK. While fatigue crack growth rates in some materials are higher for small cracks, many alloys (cf., Lankford, 1982; Tanaka, *et al*., 1983; Newman 1994) have displayed notable acceleration and deceleration in terms of crack growth rates for a single crack. This small crack acceleration/deceleration, or rather "scatter", has been associated with several factors including grain boundary interaction and microstructural barriers. Crystal plasticity simulations performed by Potirniche (2004) and Wang *et al*. (2007) and experiments (Gregory *et al*., 1984; Gungor and Edwards, 1993; Przystupa *et al*., 1997; Zhai *et al*., 2001) showed that texture influences the growth of microstructurally small fatigue cracks. In terms of grain boundary interaction, Zhai *et al*. (2005), through the use of a crystallographic model, showed that the grain boundaries caused cracks to arrest and become non-propagating. These small cracks grew where there was a low energy path at a grain boundary (they studied al-li 8090 alloy and 2026 aluminum alloy). They also demonstrated that these small cracks typically grew along slip planes within a grain and were deflected by grain boundaries. They concluded that small crack growth is microstructure-sensitive and that the variance of the microstructure near the crack tip is responsible for the observed scatter of the small fatigue crack data.

Microstructural barriers, such as intermetallics (Yi *et al*., 2004), influence small crack growth as well as triple points (Picu, 1996; Picu and Gupta, 1996). Small crack growth rates have been shown to decline as the volume fraction of intermetallics is increased (Yi *et al*., 2004). More intermetallics create more barriers for dislocations which reduce their movement and the overall accumulation of cracks. Thus, the higher concentration of intermetallics leads to crack retardation and a slower damage accumulation rate.

Lastly, research performed by Forth *et al*. (2003) and Newman *et al*. (2005) has shown that the traditional load-reduction method employed in generating large-crack data results in higher thresholds and slower fatigue-crack-growth rates in the near-threshold regime. As such, this perceived difference may actually be caused by the long crack test procedure itself.

A common long crack growth rate test typically involves a compact tension specimen and various instrumentations to monitor the crack length. There are several commercial products which automate the recording process of measuring the crack length versus cycles, thus greatly simplifying the process. While generating long crack growth data is a relatively straightforward approach, small crack testing can be more cumbersome and involves several methods. These methods include plastic replicas (Brown and Smith, 1984), marker bands (Swain and Newman, 1984), electrical potential (Gangloff, 1981), and ultrasonic surface waves (Walker, 1983). However, only the replica method can generate crack growth results for initial crack lengths in the range of 10-20μm. The replica method involves making replicas of the area of interest using

various fast drying/curing or impression materials. Small crack testing programs have employed the use of an acetyl cellulose film as the replica material (Newman *et al*., 1988; Newman and Edwards, 1988). This method involves pressing the film onto the specimen after swabbing the area with acetone. After the film has dried, it can be removed and viewed under high magnification in a scanning electron microscope (SEM). However, the use of the acetyl cellulose film has several drawbacks. The first issue involves the crack lengths that are impressed on the film. Newman *et al*. (1994) reported that the acetyl cellulose film shrinks by about 10%, thus any crack lengths measured from these replicas are smaller by 10% compared to the actual crack length. The other issue is an apparent increase in fatigue life compared to non-replica tests due to the acetone being applied to the notch surface during the replica process and protecting the small crack from the laboratory environment (Newman *et al*., 1994).

Despite the aforementioned problems associated with acetyl cellulose film, the basic idea of surface replication is still a valid approach. As an alternative to the acetyl cellulose film, a two-part silicone mixture (Repliset®) was recently employed with good success. Newman *et al*., (2006) conducted a study to determine the feasibility of using Repliset® to detect cracks in a NASA related reliability project. They found that Repliset®, through the use of SEM analysis, could detect cracks less than 25 μm with a resolution of 0.1μm and was highly accurate when compared to destructive analysis. While their purpose was not in generating small crack growth rates but rather crack

detection, they had generated enough da/dN vs ΔK data points for Inconel 178 to demonstrate the usefulness of using this silicone mixture for generating small crack data.

The emphasis of this work is to present a variation of the replica method for generating small fatigue crack data for notch specimens under constant amplitude loading. Since prior replica methods involving acetyl cellulose film may have influenced the crack growth rates, an alternative method using Repliset® for making replicas provided the basis for the motivation of this research. Additionally, the results of the small crack experiments will be used to provide a baseline for fatigue life for the notched specimens with two types of surface preparation over a range of stress levels. Also, fatigue life predictions using FASTRAN were made based on observed inclusion/particle sizes. While small fatigue crack growth results for the 7075-T6 aluminum alloy exist, an additional contribution of this work is to present experimental small crack growth results for the T651 temper.

Experiments and Materials

The 7075-T651 aluminum alloy is a fairly high strength material used heavily in the aircraft industry. This wrought alloy was examined in its as-received condition using a scanning electron microscope (SEM) and an optical microscope. The grains and particles of this wrought material were found to be pancake shaped and were aligned in the rolling direction of the plate. It is also apparent from microstructural analysis that many inclusions were broken during the manufacturing process and distributed along the

rolling direction, creating a non-uniform particle distribution process. The yield stress and the ultimate tensile strength was 510 and 558 MPa, respectively.

The single-edge-notch tension, SEN(T), specimen as shown in Fig. 4.1, was employed in this study and was also used in previous small-crack test programs (cf., Newman and Edwards, 1988). The semi-circular notch radius, r = 2.41 mm, was selected based on a fastener-hole size in a particular aircraft application. A majority of fatigue failures in winged aircraft are a result of high stress concentration locations like fastener holes. The applied loading for specimens in this testing program was selected to represent the type of loading that is typical of aircraft fastener holes. Standard stress-life fatigue tests were conducted over a range of applied stress levels. Tests were conducted on two notch preparation procedures: (1) as-machined to represent actual manufacturing procedures and (2) as-machined and chemically polished. The chemical polishing procedure included submerging the specimens in a chemical bath at a temperature of 85C for five minutes. The chemical solution used to polish the notch surfaces contained the following chemical composition: 94% Phosphoric Acid and 6% Nitric Acid. SEM analysis of the notch surface in the as-machined (Fig. 4.2) and polished condition (Fig. 4.3) show the difference in the two surfaces. The chemical polishing removed the residual machining marks and burs as a result of the drilling procedure.

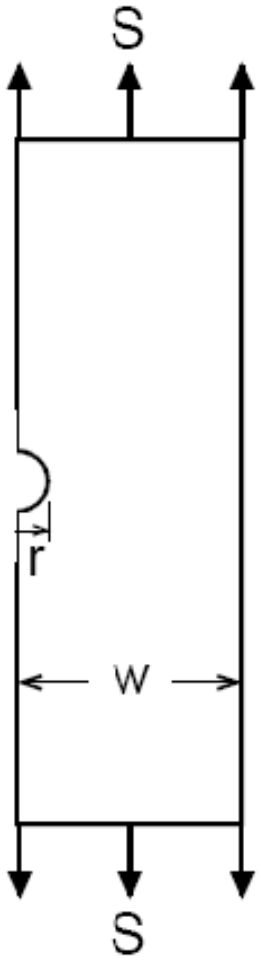

Figure 4.1 Single-edge-notch tension, SEN(T), specimen configuration for constant-amplitude loading (Newman *et al*., 1994).

Figure 4.2 Scanning electron microscope analysis of the notch surface of the SEN(T) specimen in the as-machined condition.

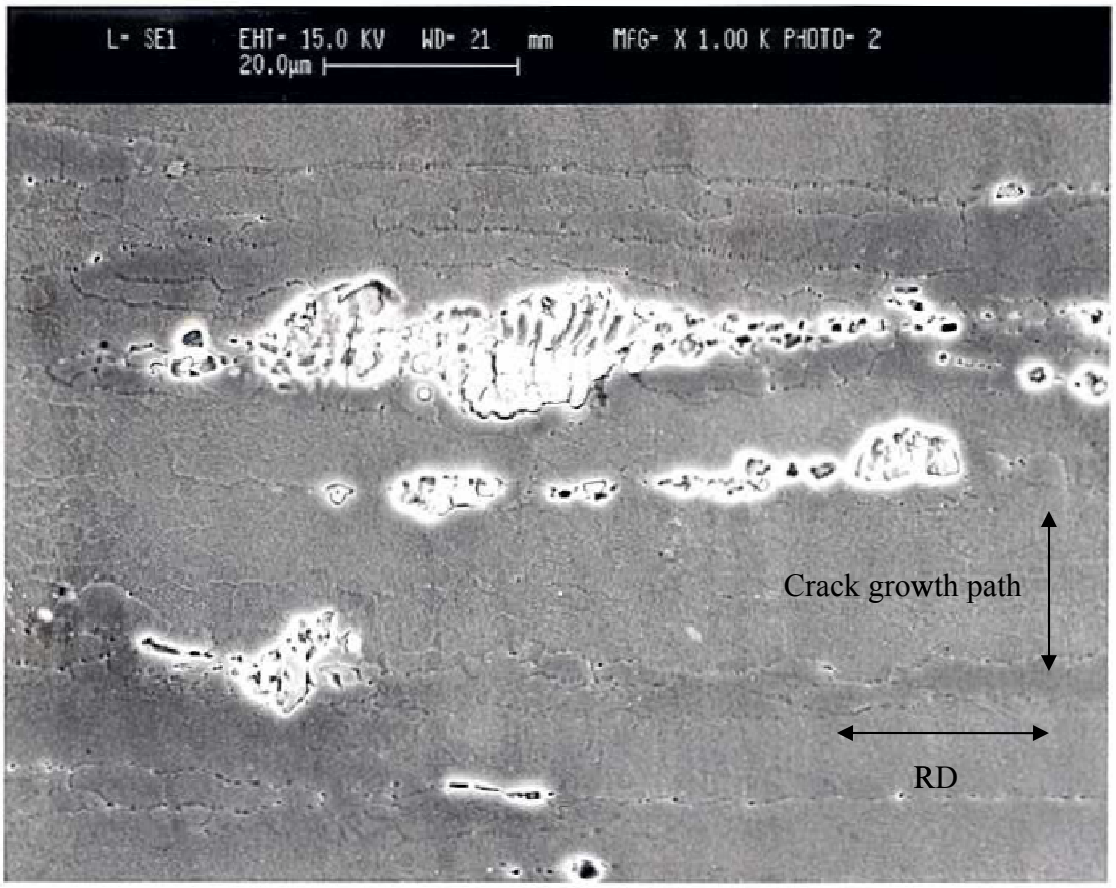

Figure 4.3 Scanning electron microscope analysis of the notch surface of the SEN(T) specimen in the chemically polished condition.

A replica method was employed to monitor the growth of small cracks-10 µm to 2 mm in length along the notch bore. The replica method is a non-destructive method of recording the crack initiation and growth in the circular notch area. The replica process required applying the Repliset® (two-part silicone mixture) material into the notch region and allowing for the silicone replica to set (approximately 10 minutes). A static tip mixing nozzle and dispensing gun, as shown in Fig. 4.4, were used to dispense the Repliset® material onto the notch and tape was applied over the notch to support the

silicon mixture as it set. Once the replica had solidified, the replica was removed and an inverted image of the notch surface was preserved. Typically, replicas were taken at approximately 1,000 cyclic intervals, such that at least 25 to 30 replicas were obtained during the fatigue life of a particular specimen. After the last replica had been taken, the replicas were coated in gold-palladium and then examined in a scanning-electron microscope (starting from the last replica and proceeding backwards to the earliest replica) to record the crack length along the bore of the notch. Fig. 4.5 shows a representative set of replicas for the small crack study. Finally, it is necessary to note that a non-interaction criterion was used to exempt crack growth rates that may have been influenced by neighboring cracks. See Newman *et al*. (1994) for details regarding this criterion.

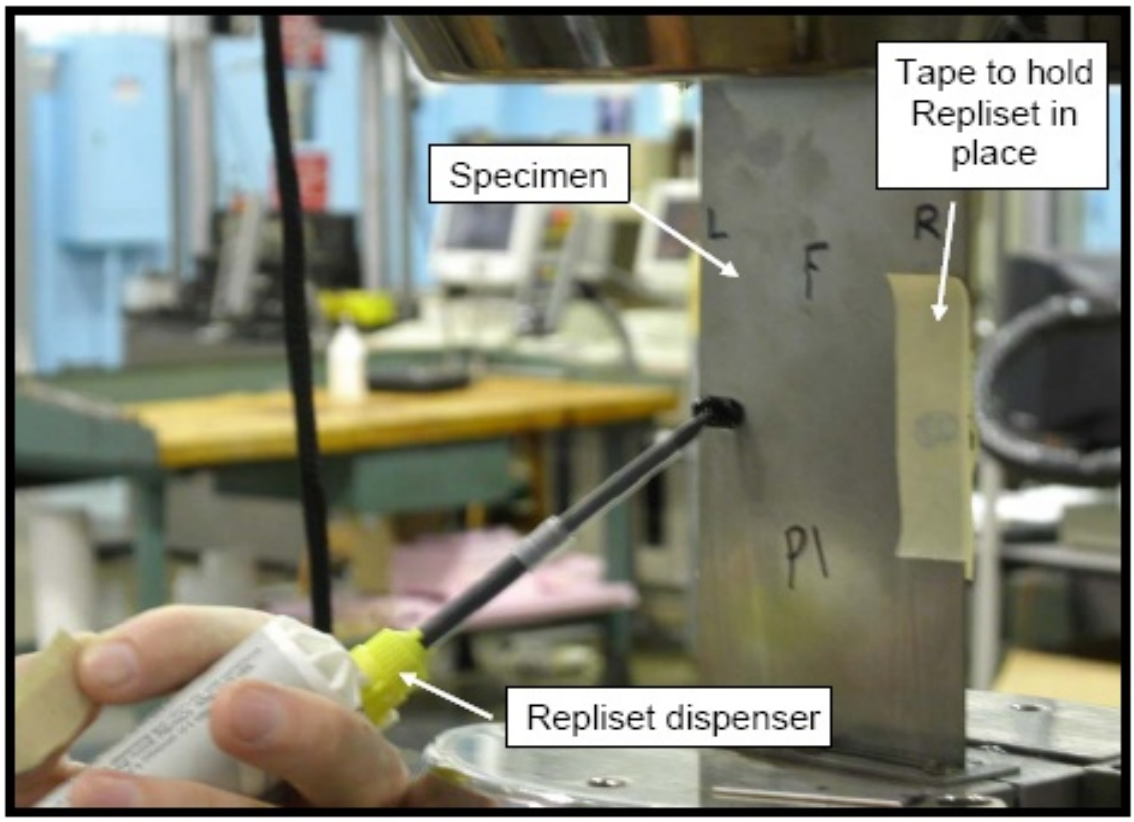

Figure 4.4 A representative view of the procedure for applying Repliset®, which involves using a static tip mixing nozzle and tape to hold the Repliset® material in place (Newman *et al*., 2006).

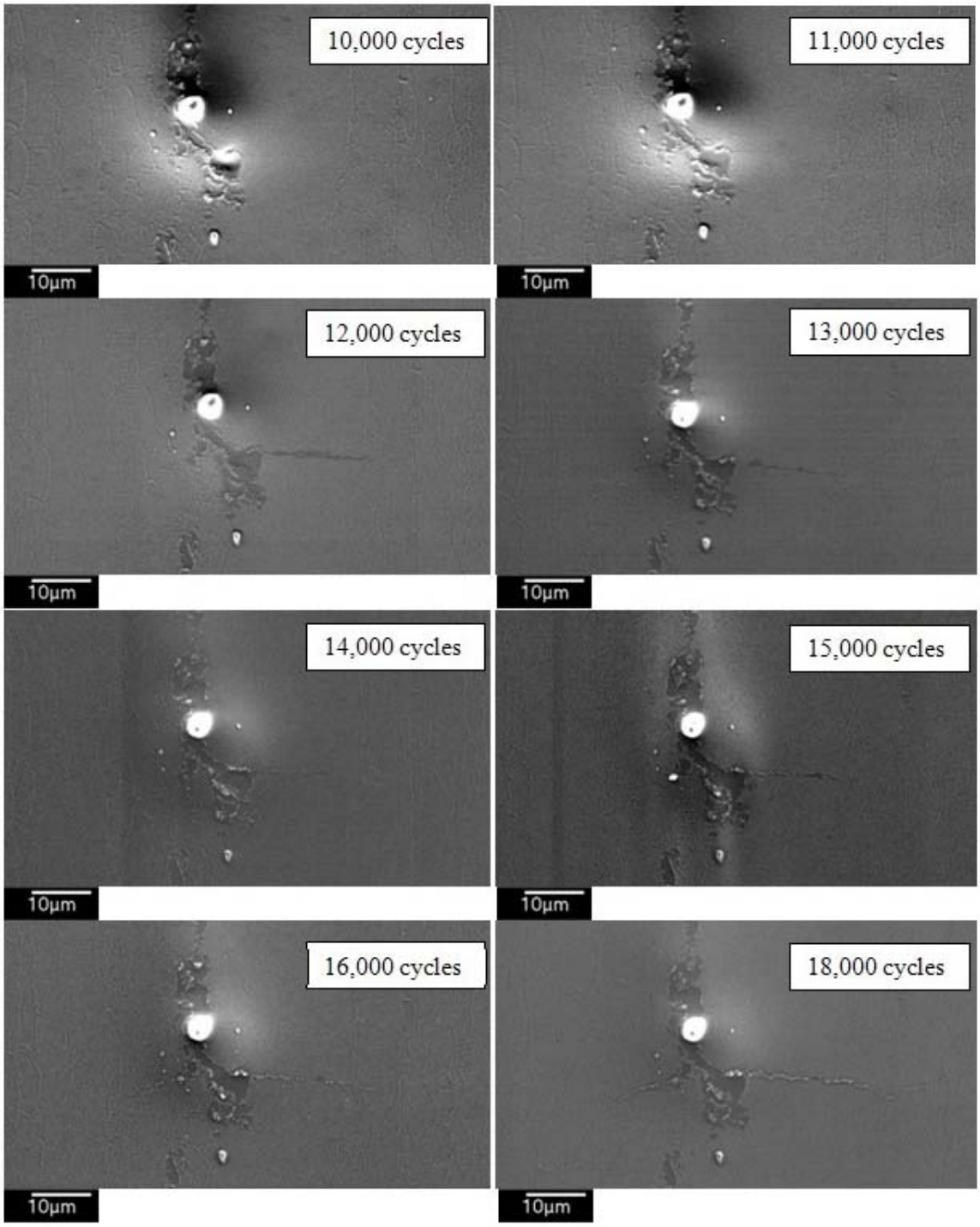

Figure 4.5 SEM images of replicas for SEN(T) specimen in the polished condition for a crack growing from an intermetallic particle over a range of 8,000 cycles.

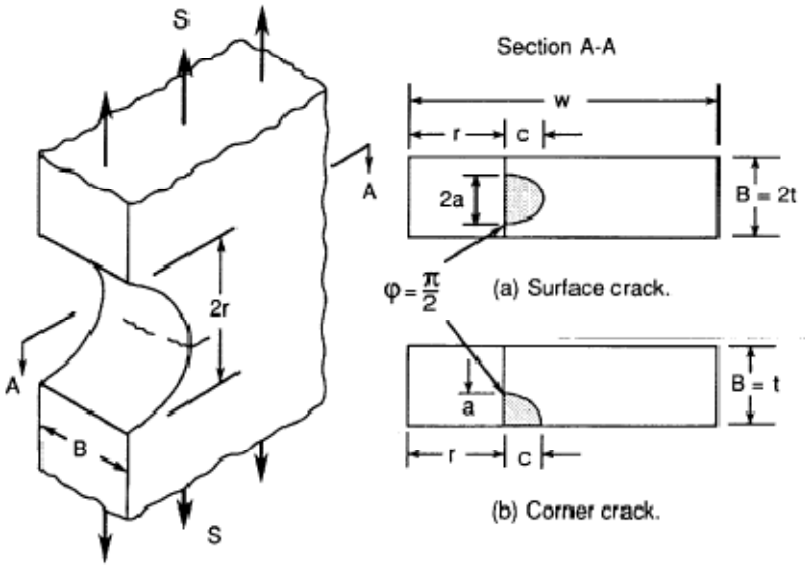

Figure 4.6 Single-edge-notch tension, SEN(T), specimen configuration (Newman *et al*., 1994).

Fig. 4.6 displays the nomenclature associated with SEN(T) specimens, where 2a represent the surface crack length, c is the crack depth, w is the specimen width, B is the specimen thickness, and r is the notch radius. In this particular study, w= 43.18mm, B= 5.715mm, and r= 2.413mm. The calculation of the stress intensity factor range (ΔK) follows that of Newman *et al*. (1994). The stress intensity factor range is

$$\Delta K = \Delta S \left(\frac{\pi a}{Q} \right)^{1/2} F \tag{4.1}$$

where ΔS is uniform gross remote stress range (S_{max}-S_{min}), a is the crack length, Q is a shape factor and F is a correction factor for either a surface (F_s) or corner crack (F_c). In

order to calculate the crack-growth rates, a simple point-to-point method was employed from

$$\frac{da}{dN} = \frac{\Delta a}{\Delta N} = \frac{a_{i+1} - a_i}{N_{i+1} - N_i} \tag{4.2}$$

where ΔN and Δa are the cyclic interval and crack length, respectively, and a_i is the crack length at N_i cycles.

Plasticity-Induced Crack Closure Model

The FASTRAN fatigue life-prediction model is based upon the Dugdale strip-yield model (1960). The Dugdale model approximates the plastic yielding and plastic deformation ahead of the crack tip using the strip-yield concept. The FASTRAN fatigue crack growth model builds on the Dugdale model by including the effect of plasticity induced wake behind the crack tip. Originally, the FASTRAN model (Newman, 1981) was developed to predict crack growth from a centrally located crack in a finite-width specimen. The model was updated to account for other through cracks (Newman, 1983), and later was modified to predict crack growth in two dimensions and to distinguish between surface and corner cracks (Newman 1992). Additionally, the model was applied to small cracks with good agreement (Newman *et al*., 1994, 2008). In order to model stress ratio effects on crack growth rate data, a constraint factor (α) is used to correlate constant amplitude fatigue crack growth rate data to effective stress intensity factor (ΔK_{eff}), developed by Elber (1971). The FASTRAN model employed in this study is

version 4.46 and was calibrated with small and long crack 7075-T651 aluminum data presented in Newman *et al*. (2008).

Results and Discussion

Fatigue life tests were performed on the SEN(T) specimen to determine the appropriate stress level for the replica tests and to evaluate the difference in the fatigue life for the as-machined and polished specimens. The results of the stress-life tests for the SEN(T) specimens are shown in Fig. 4.7, where S_{max} is the maximum gross stress, and N_f is the number of cycles to failure. The solid symbol represents the as-machined condition and the open symbol is the specimen subjected to chemical polishing. The results show that chemical polishing reduced the fatigue life for the higher stress levels by half, but for the lower stress levels, the life was lower by as much as an order of magnitude. This difference in fatigue life is likely attributed to a reduction of the surface residual stresses via the polishing process. The as-machined surface of the notch will inherently contain more surface residual stresses due to the drilling procedure. As such, the chemical polishing process reduced the surface residual stress by removing several microns of material- thus eliminating the fatigue resistance provided by the machining process. The polishing process also revealed many inclusions/flaws at or near the surface that were covered by the plastically deformed material due to the machining. As such, a greater percentage of inclusions were exposed to the free surface which created more areas for crack initiation. In addition, the polished surface also contained pits that were

created by intermetallics becoming dislodged and falling out of the matrix during specimen preparation.

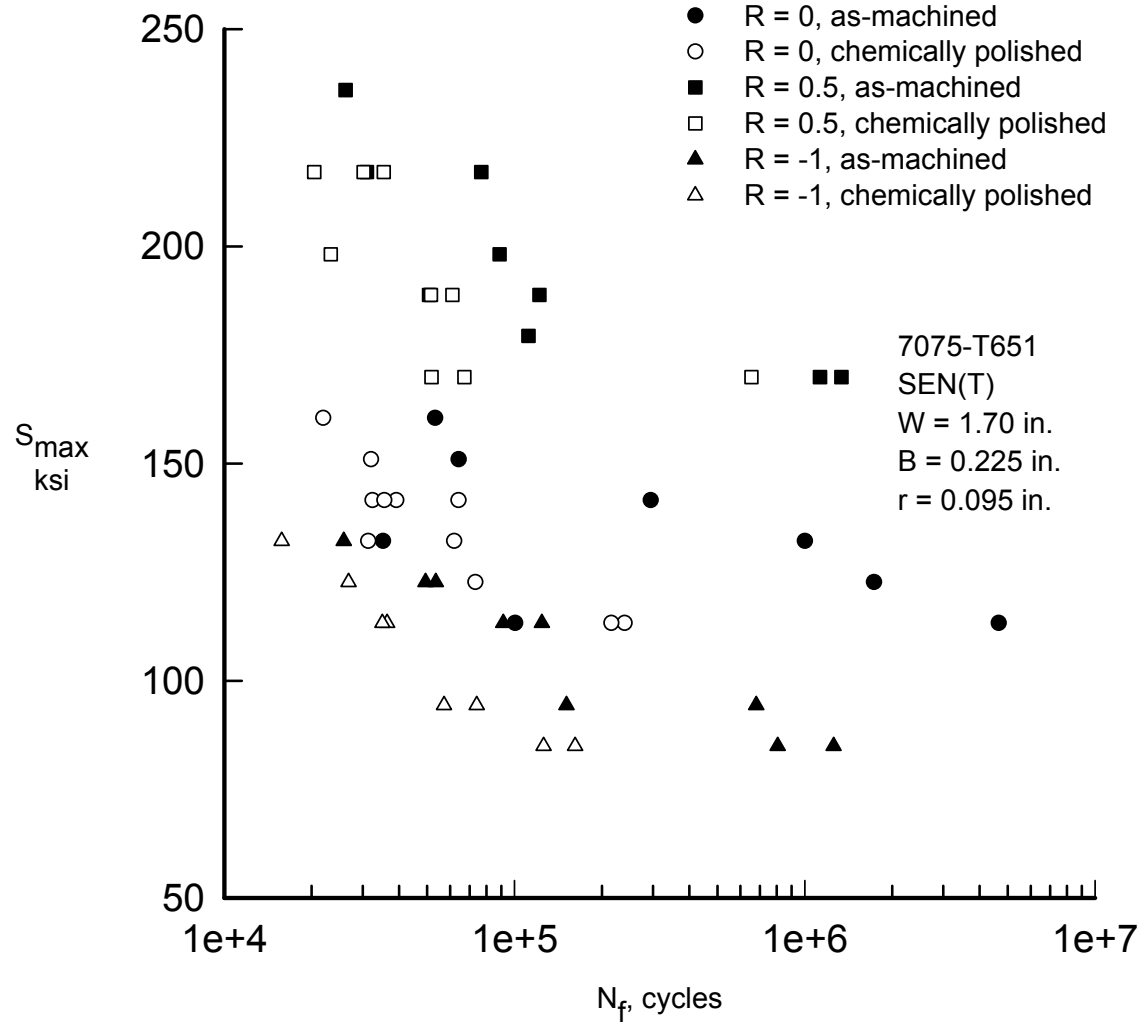

Figure 4.7 Fatigue life results of the single-edge-notch tension specimen for both polished and as-machined at various stress levels for 7075-T651 aluminum alloy.

In order to determine how much of an affect the replica process had on fatigue life, the results of the fatigue life replica experiments were compared to non-replica tests.

Fig. 4.8 compares the average failure cycle along with the upper and lower bounds for the replica and non-replica tests. This comparison shows that the replica procedure had little if any affect on the fatigue life. While the maximum and minimum fatigue life for some of the replica tests were outside the bounds of non-replica tests, overall the replica tests compared very closely to the non-replica tests and the differences could be attributed to statistical variance.

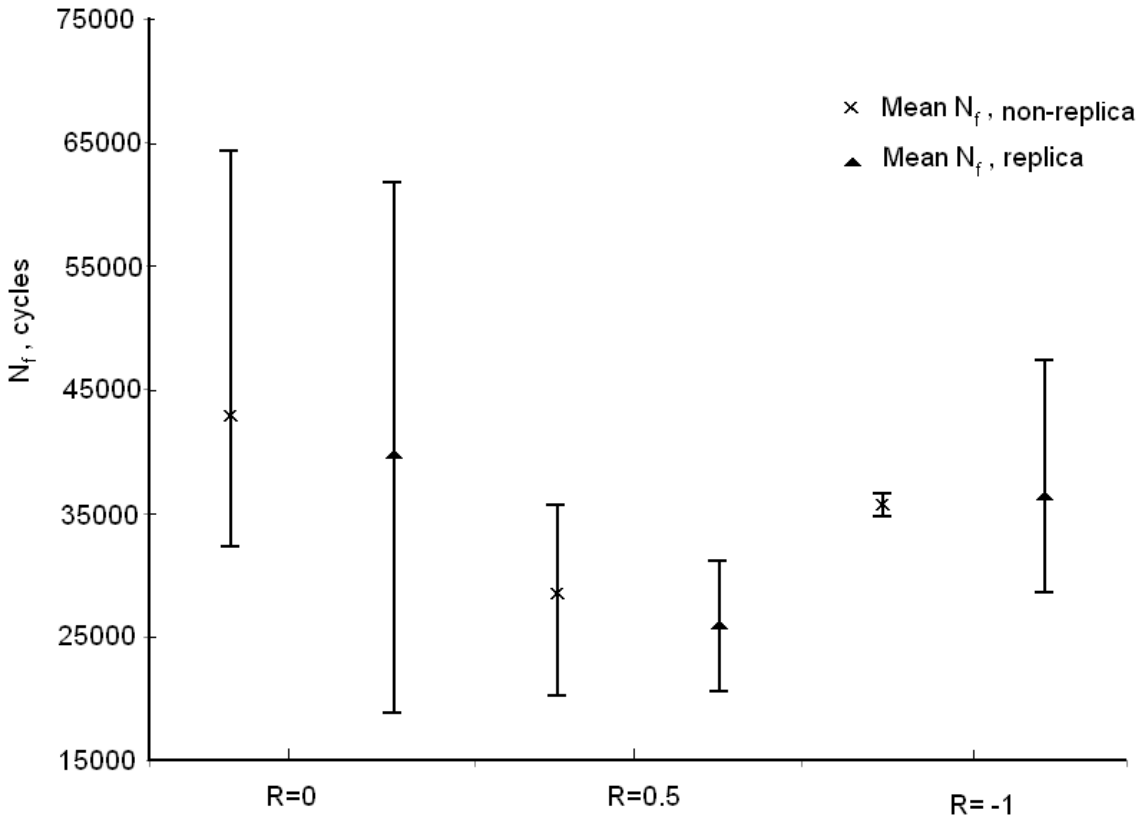

Figure 4.8 Fatigue life results for single-edge-notch specimens comparing replica tests to non-replica tests for 7075-T651 aluminum alloy. Both replica and non-replica tests had a chemically polished notch.

To determine the factors responsible for the large discrepancy in fatigue life results for the as-machined and chemically polished specimens, initial flaw sizes for the chemically polished SEN(T) specimens are presented in Fig. 4.9. SEM analysis of the fracture surface of the chemically polished SEN(T) specimens cyclically loaded to failure showed that the critical surface inclusion/flaw ($2a_i$) ranged from 7.7 to 31.1 μm, and the depth (c_i) of the flaw varied from 7.4 to 38.8 μm. These results compared well with test results conducted at NAVAIR (Newman et al, 2008), where the critical inclusion had a surface length ($2a_i$) that ranged from 6-35 μm and a depth (c_i) of 12-55 μm as shown in Fig. 4.10. While the surface of NAVIAR specimens were not chemically polished, the critical inclusion sizes were very similar to sizes observed in this study.

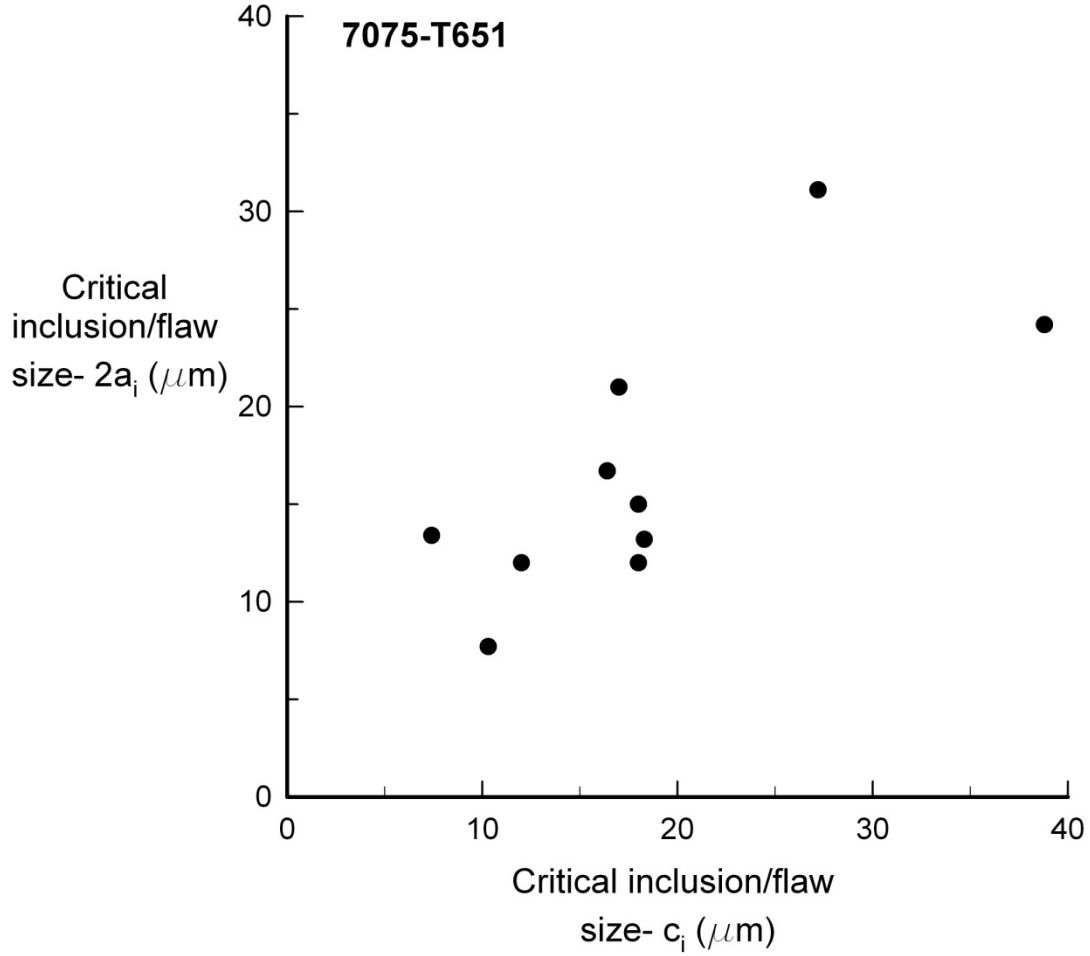

Figure 4.9 The 7075-T651 aluminum alloy critical inclusion size ($2a_i$ and c_i) was based on SEM analysis of the fracture surface of the single-edge-notch specimens. The notch surface was chemically polished.

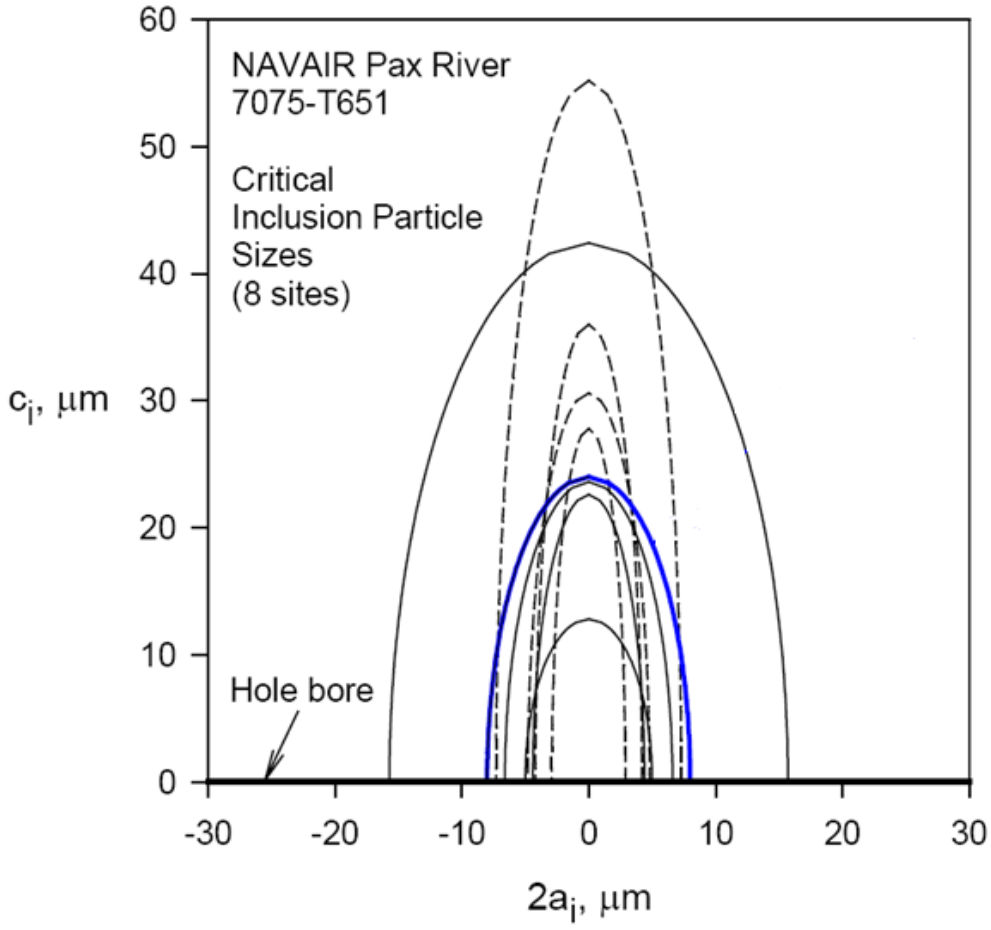

Figure 4.10 Inclusion-particle or cluster sizes and shapes for eight cracks monitored at NAVAIR (Newman *et al.*, 2008).

The results of the SEN(T) small fatigue growth rates calculated from the replicas for R=0, R=0.5, and R=-1 load ratios are presented in Fig. 4.11, Fig, 4.12 and Fig. 4.13, respectively. The maximum stress levels and the load ratios for the replica tests are presented in Table 4.1. In addition, for each of the load ratios, the replicas were taken at the same maximum stress level to maintain consistency in comparing the experimental results. The different symbols used to display the small crack growth results represent

individual specimens. Also, the data points presented for each of the load ratios represent several cracks, as multiple cracks were monitored for most specimens. The most obvious observation for the crack growth rates is the large amount of scatter at the lower rates. This is not surprising considering that the crack at this stage has the same characteristic length as the surrounding microstructure and thus is greatly influenced by grain boundaries and inclusion barriers which account for the acceleration and deceleration of the cracks. In addition the small crack data displayed a load ratio effect similar to the long crack results presented in Newman *et al*. (2008). The smallest crack lengths observed on the replicas were 10-20μm in length (2a) and these small cracks grew from smaller surface inclusions/flaws (surface length range of 3-10μm). In contrast, the critical/dominant crack typically grew from the larger surface particles/flaws which were in the range of 7μm-32μm. Lastly, as a general observation, the first surface cracks typically initiated early- at about 5-30% of the total fatigue life with the rest of the fatigue life comprised of crack growth.

Table 4.1 Small Crack Test Summary for 7075-T651 Aluminum Alloy

Load Ratio	Maximum Stress (MPa)	Number of tests
R=0	141.3	3
R=0.5	213.7	3
R= -1	113.1	2

For additional comparison, the FASTRAN model was employed to predict the replica small crack growth rate results (Fig. 4.11-13). The max load used in the

FASTRAN calculations was the same load that the replica tests were conducted at for each of the load ratios. In order to make crack growth rate predictions, the K_{eff}-rate relation (not shown) was estimated based on the small crack data. An initial flaw size was chosen to represent the defect in the chemically polished specimen. The critical flaw sizes presented in Fig. 4.9 for surface crack lengths ($2a_i$) and the depth of the crack (c_i) were used to estimate a minimum flaw size for the model predictions. For the FASTRAN calculations the initial flaw size was chosen: $a_i = 3.8\mu m$; $c_i = 8.4\mu m$. In terms of comparing the model predictions to the experiments, the FASTRAN model was able to capture the change in rate at 9E-09 m/cycle for the three load ratios. At this level, the model predicted a sharp initial decrease or "dip" for R=0 and R=-1 load ratios. As the crack grew, the closure level increased faster than the ΔK level and as such the crack growth rate rapidly decreased until the crack opening stresses had stabilized. Thus, this "dip" in the crack growth rates is primarily a result of the closure transient. In contrast, the crack is fully opened for the R=0.5 loading and the model does not show a "dip" or "sharp decrease" because the ΔK and ΔK_{eff} rates at this load ratio are essentially the same (Fig 4.13).

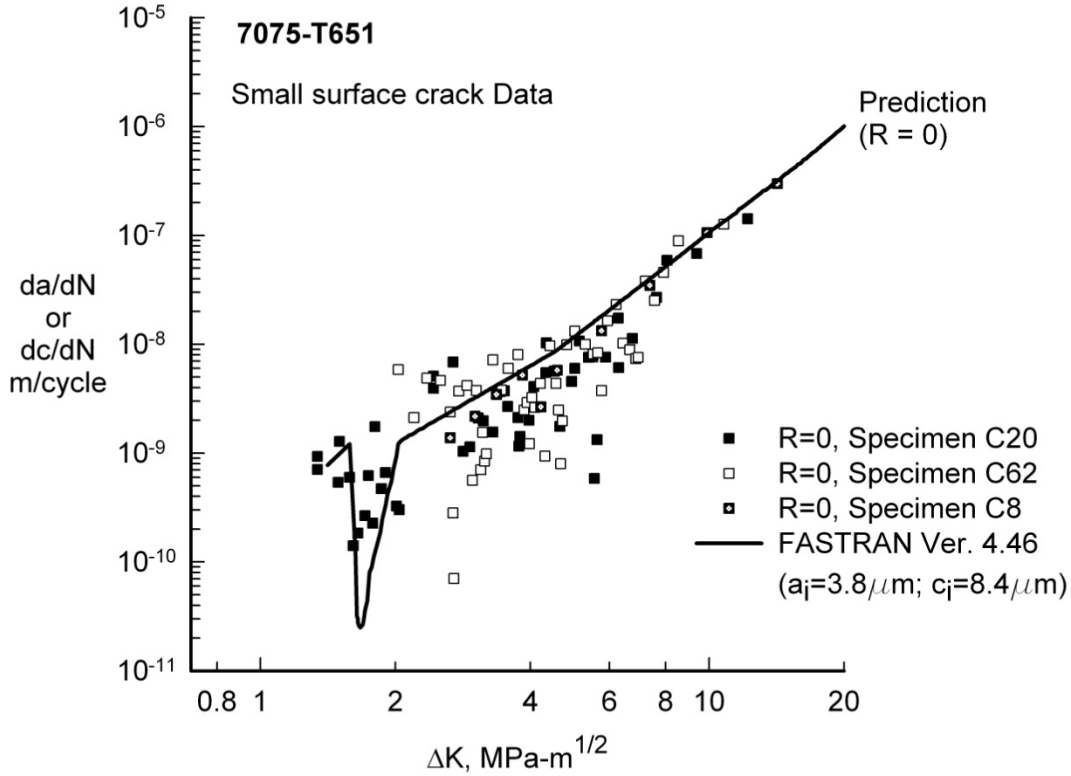

Figure 4.11 Small surface crack (Smax = 141 MPa) and FASTRAN model for crack growth rates against $\triangle K$ for 7075-T651 aluminum alloy for R = 0.

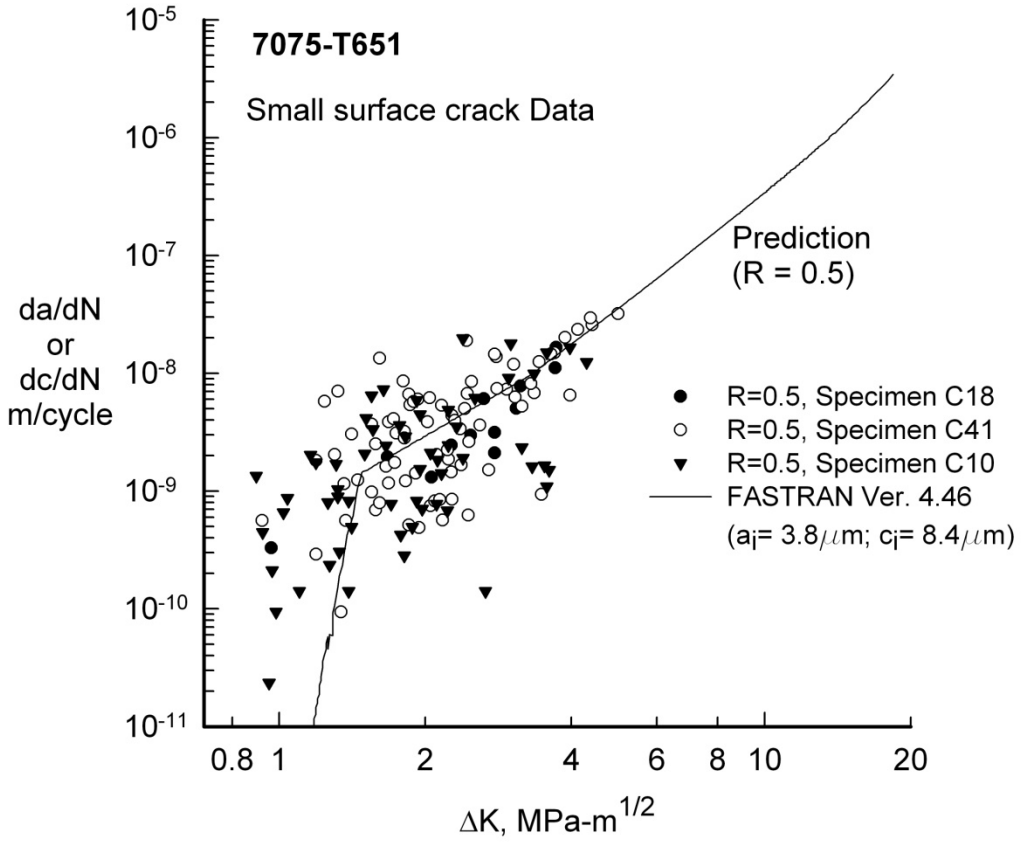

Figure 4.12 Small surface crack (Smax = 213 MPa) and FASTRAN model for crack growth rates against ΔK for 7075-T651 aluminum alloy for R = 0.5.

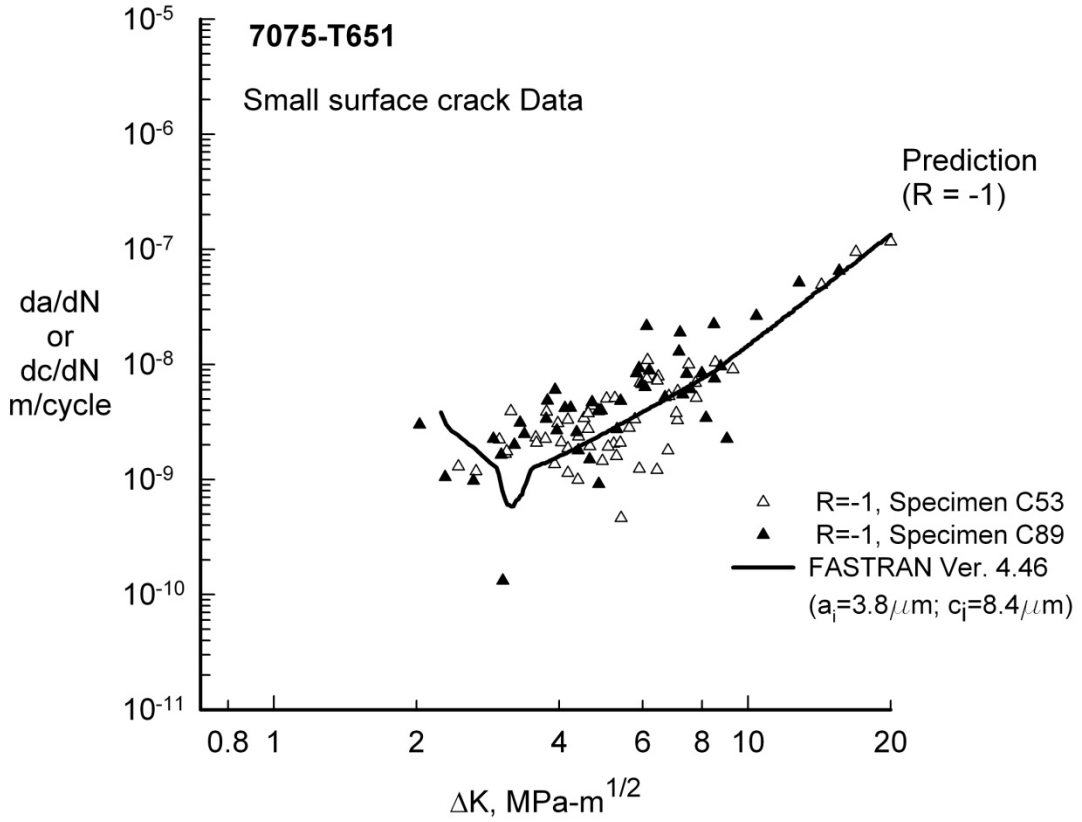

Figure 4.13 Small surface crack (Smax = 110 MPa) and FASTRAN model for crack growth rates against ΔK for 7075-T651 aluminum alloy for R = -1.

The last stage of this study was to use the FASTRAN model to predict the upper and lower bounds of fatigue-life results for the as-machined and polished SEN(T) specimens. In order to account for the discrepancy between the polished and as-machined, two initial flaw sizes were used in an attempt to predict the differences in the results. For the as-machined specimens, a minimum flaw size, where a_i= 2 μm and c_i= 4.5 μm was chosen based on work by Newman *at al*. (2008) where the particle aspect ratio of c_i to a_i was 2.25:1. For the chemically polished specimens, a flaw size used to predict the lower bounds was chosen based on the aspect ratio of 2.25:1 and information

presented in Fig. 4.9, where a_i= 17.5 μm and c_i= 39 μm. The fatigue-life predictions made by FASTRAN for the chemically polished and as-machined specimens are presented in Fig. 4.14-16. Based on the two different critical flaw sizes, the model was able to bound the experimental results for all three load ratios. At the higher stress levels for R=0 and R=-1, the model showed the most agreement with the experimental results. For the lower stress levels of all three load ratios, the model did not bound the experiments very well. However, if more experiments were conducted on the polished specimens at the lower stress levels, the fatigue life results may show better agreement to the model predictions. In addition, for the R=0.5 test, the model predicted more scatter in the fatigue results than experimentally observed. While no explanation for this discrepancy is given here, future work will attempt to determine the cause. In any case, the modeling effort presented here suggests that the difference in the as-machined versus chemically polished specimens is a function of the initial flaw/inclusion size. As previously stated, there are residual stresses on the notch surface due to the drilling procedure. However, the FASTRAN model did not include these residual stresses in the calculations, and as such, future modeling could include the effect of the drilling process to improve the fatigue-life predictions.

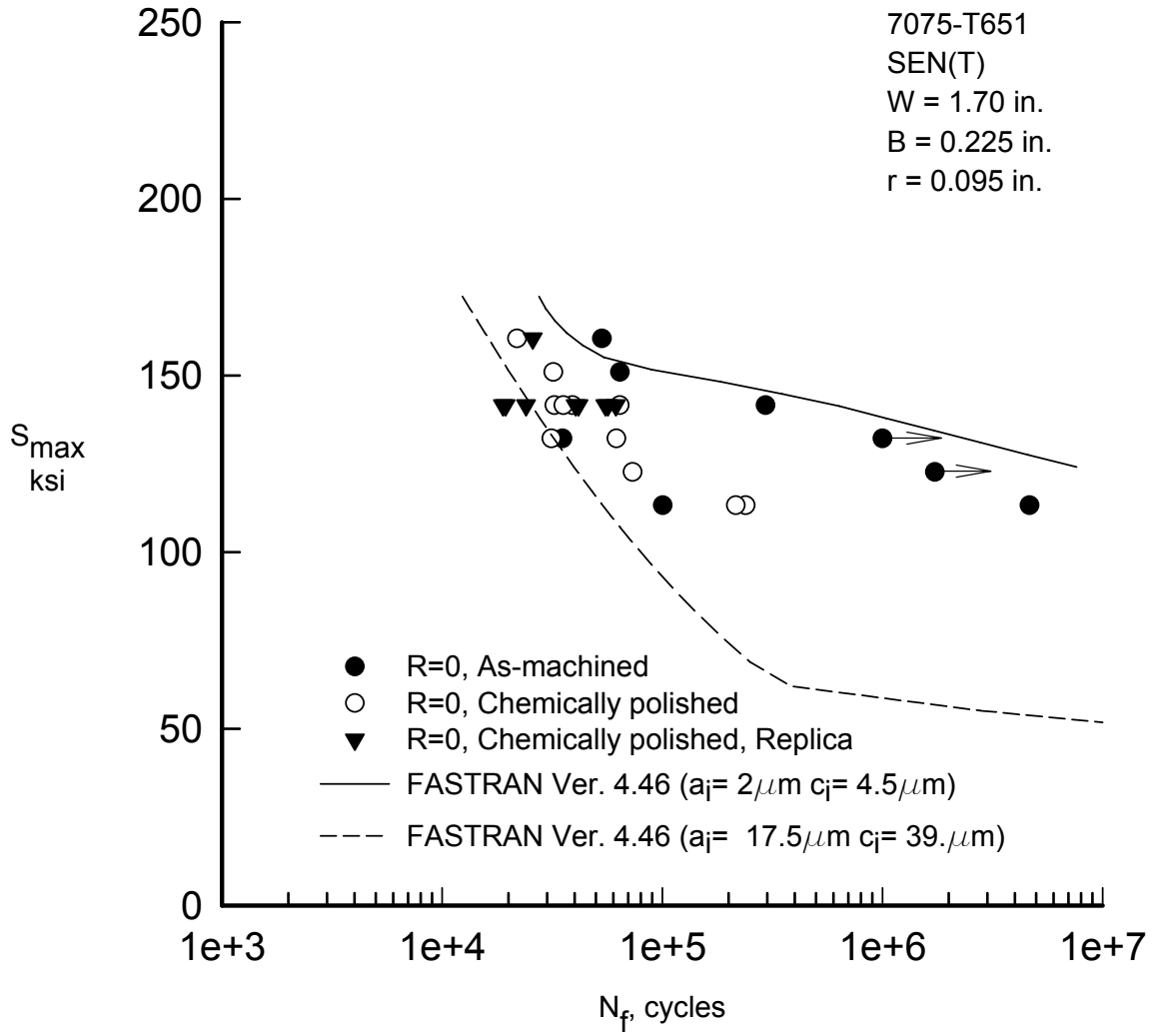

Figure 4.14 Comparison of experimental fatigue results of the SEN(T) specimens for R=0 and the FASTRAN model for 7075-T651 aluminum alloy.

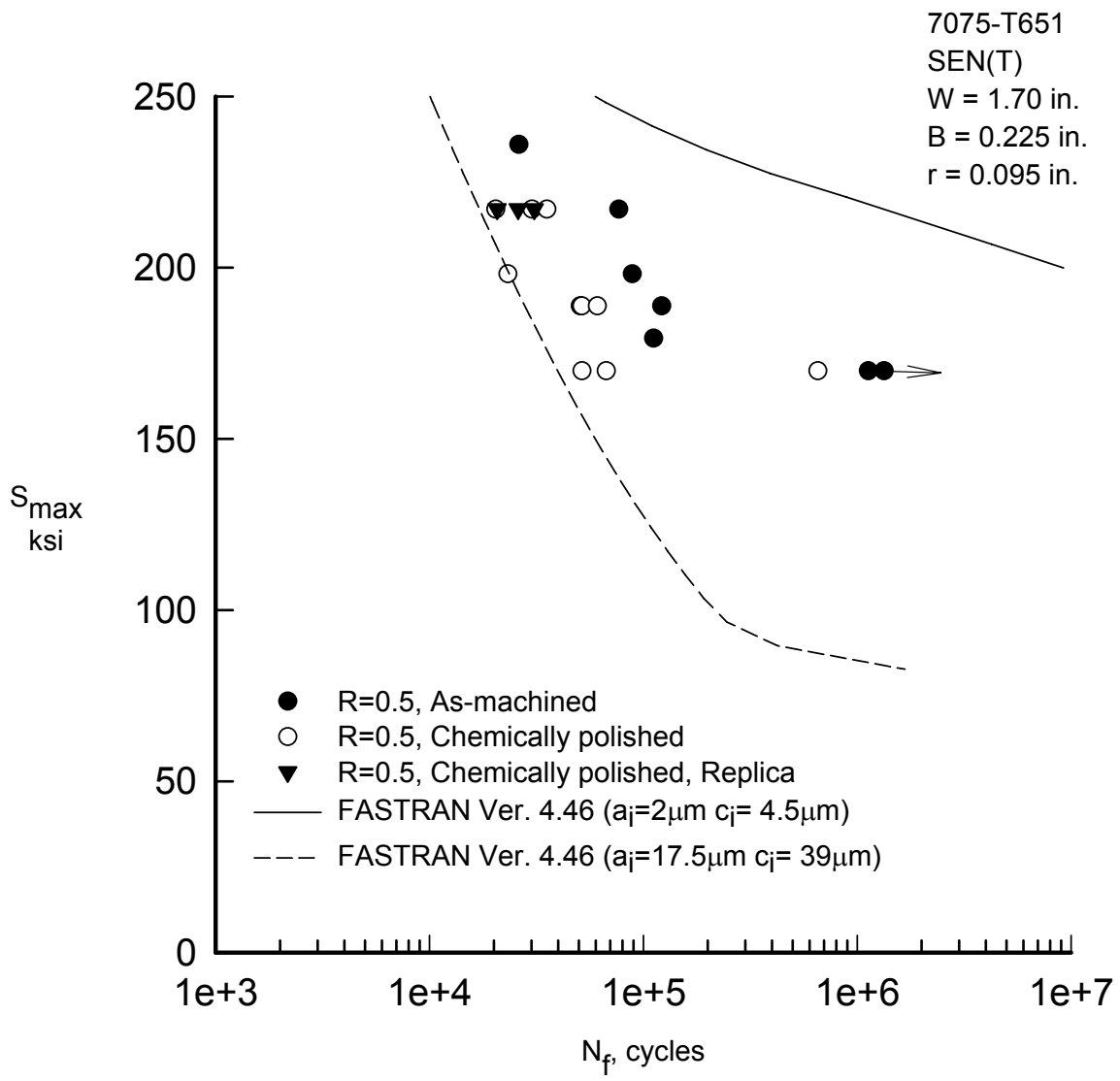

Figure 4.15 Comparison of experimental fatigue results of the SEN(T) specimens for R=0.5 and the FASTRAN model for 7075-T651 aluminum alloy.

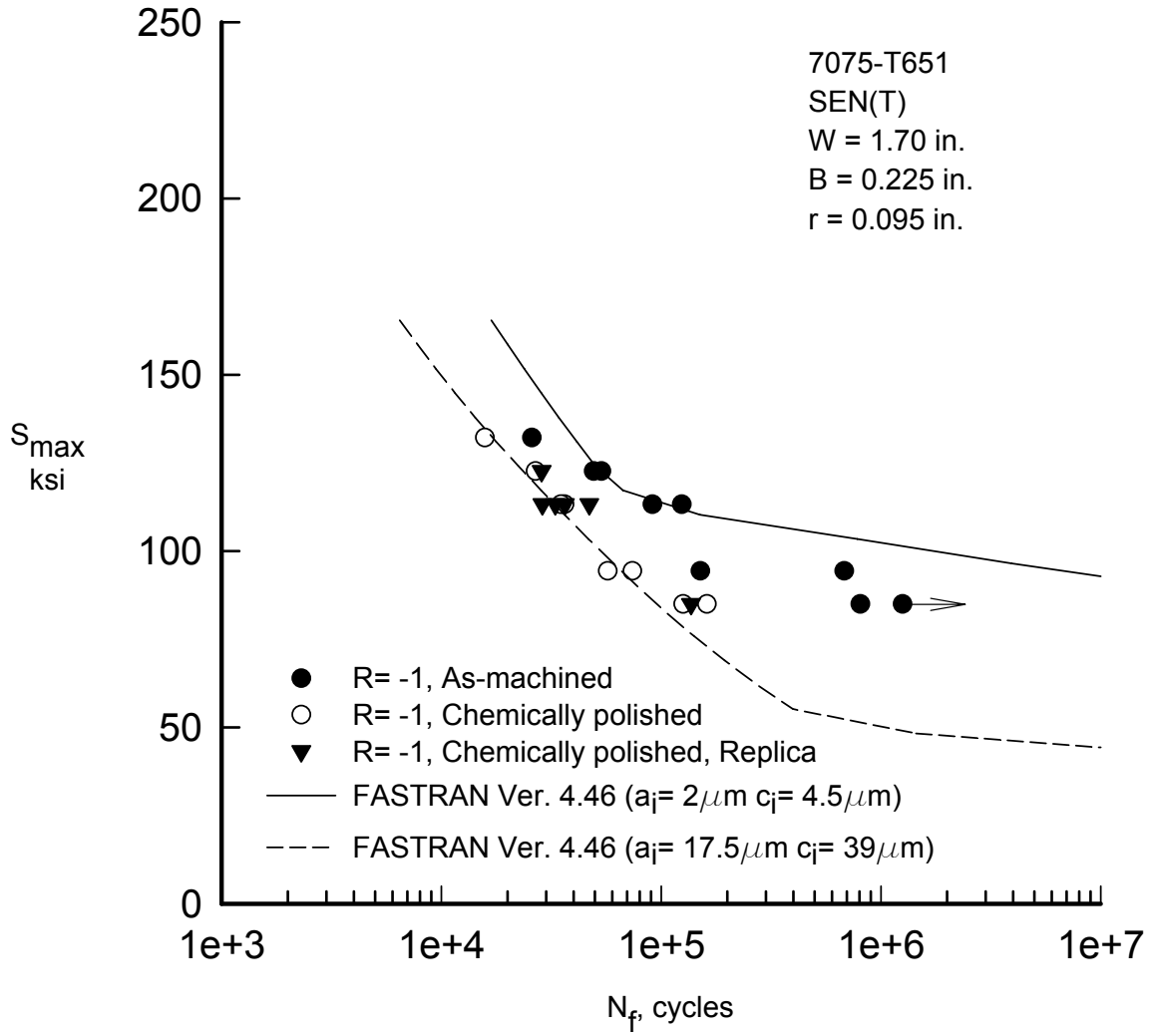

Figure 4.16 Comparison of experimental fatigue results of the SEN(T) specimens for R= -1 and the FASTRAN model for 7075-T651 aluminum alloy.

Conclusions

The purpose of this work was to present small fatigue crack growth results for single-edge-notch tension specimens on the 7075-T651 wrought aluminum alloy. A two-part silicon based replica method was employed to measure microstructurally small fatigue cracks emanating from surface inclusion particles. The small crack growth results

displayed a large amount of scatter at near-threshold levels due to grain boundary blocking and other microstructural barriers. In addition, tests were conducted to determine the effect of the replica process on fatigue life compared to non-replica specimens. The fatigue life results show that the replica method had little or no effect on fatigue life. As such, the replica method presented here offers a valid method for generating small crack growth results on notch specimens. Lastly, the FASTRAN model was employed to predict the upper and lower bounds of the fatigue-life results for the as-machined and chemically polished specimens by using initial flaw sizes determined from scanning electron microscope analysis.

CHAPTER V

MICROSTRUCTURAL DAMAGE HISTORY EFFECT ON ALUMINUM ALLOYS

Introduction

Failure of metallic components due to fatigue damage is a common engineering problem and much effort has been put forth to understand and predict damage due to cyclic loading. A review by Suresh (1991) of fatigue of metals covers many topics including crack initiation, microstructurally small fatigue crack growth, long crack growth, and different inclusions types related to failure. One area not frequently studied is related to predicting failure of a component or specimens that have preexisting damage from an overload or prestrain. An example of this type of scenario might include a premature failure of a critical automobile component under normal use, arising from an earlier "fender bender," which essentially caused an overload or prestrain. A recent literature search revealed that much of the research with regard to overloads is related to modeling crack growth retardation from tensile overload during cyclic loading (cf. Venkateswara Rao and Ritchie, 1988; Manjunatha and Parida, 2004). Depending on the magnitude of the overload, retardation of the crack growth rate arises as the compressive unloading inhibits crack growth resulting in longer fatigue life. The modeling attempts have focused on crack tip plasticity and its effect on crack growth.

On the contrary, the strength and ductility of some metals is reduced due to damage from cyclic loading prior to tensile loading. This type of loading is also representative of today's engineering problems. A material's strength and ductility is a function of its prior history and being able to model past damage accumulation is essential for safe designs. While limited, there is some research involving the effect of pre-fatiguing on tensile ductility. Recently, work by Tsuda *et al.* (2006) has shown that high strength steel alloys display lower elongation to failure after pre-cycling under low cycle fatigue. While this is not entirely surprising considering that fatigue damage accumulation can occur at intermetallics (Suresh, 1991), the extent that pre-fatiguing has on tensile properties has not been readily studied even though many mechanical components are designed to withstand large deformations and are also subjected to cyclic loading below the material's yield (i.e., bridges, automobiles, bicycles, etc.)

Under monotonic, quasi-static loading, the method of failure in ductile aluminum alloys is commonly described as a process that involves void initiation, void growth, and finally void coalescence (Garrison and Moody, 1987). In wrought alloys, the damage process is primarily a result of the fracture of intermetallics and/or second phases. In cast alloys, damage arises from both particles and casting pores. In both cases, particles crack at various rates under applied tensile, compression, and torsion loads. Like quasi-static loading, cyclic loading induces damage arising from the same microstructural features: particles and pores. However, in low cycle fatigue, particles tend to crack at lower applied strain compared to monotonic tensile loading, and experiments conducted on aluminum alloy 7075-T651 confirm this phenomenon (Harris, 2005). While the rate of

nucleation of particle fracture during low cycle fatigue loading is much less compared to monotonic loading, the damage is unmistakably present.

In this work, modeling efforts will focus on two types of loading: a) pre-fatiguing followed by tensile loading and b) prestraining followed by cyclic loading. While these types of tests are not unique, to the author's knowledge, no one has compared these types of experimental results for both a wrought and cast aluminum alloy. Thus, the purpose of this work is to explore the influence that past loading histories have on the damage mechanism of tensile and fatigue failures.

Materials

Two types of aluminum alloys were experimentally tested in this research: 7075-T651 and A356-T6 aluminum alloys. The 7075-T651 is a lightweight but high strength aluminum alloy employed heavily in the aerospace industry. A scanning electron microscope and an optical microscope were used to examine the alloy to quantify the microstructural features such as particle size and grain size. Fig. 5.1 displays the grains of this wrought material which were found to be pancake shaped and were aligned in the rolling direction of the wrought plate. In addition, iron-rich and silicon-based constituent particles were scattered throughout the alloy. Also, many of these particles were broken during the manufacturing process and distributed along the rolling direction creating an anisotropic distribution.

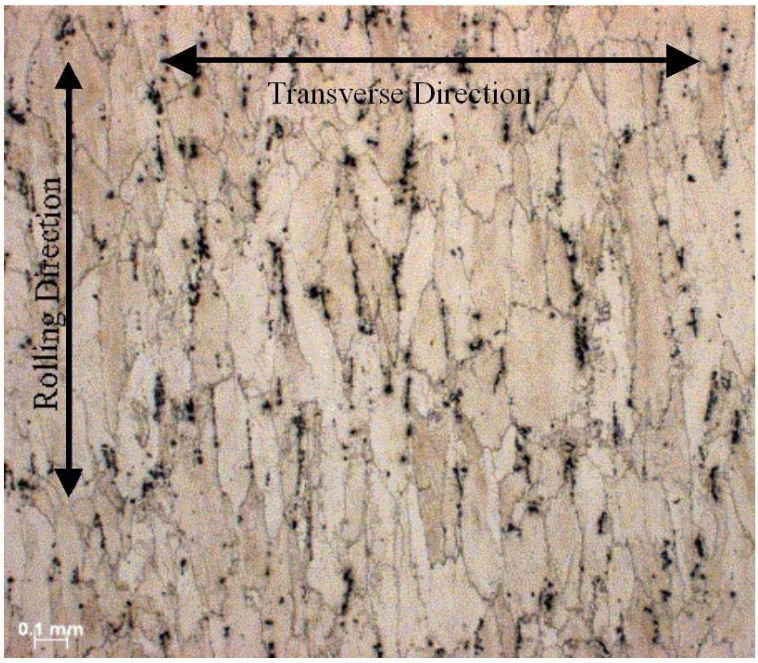

Figure 5.1 Optical micrograph of the grain structure in the rolling direction of 7075-T651 aluminum alloy (Jordon *et al*. 2007).

Similar to the wrought alloy, a scanning electron microscope and an optical microscope were employed to metallographically examine the cast A356-T6 in the billet form, as shown in Fig. 5.2. Because no rolling procedure was applied to the material, the cast alloy microstructure was naturally more isotropic compared to the wrought material as observed from the equiaxed particles and secondary dendrite arms.

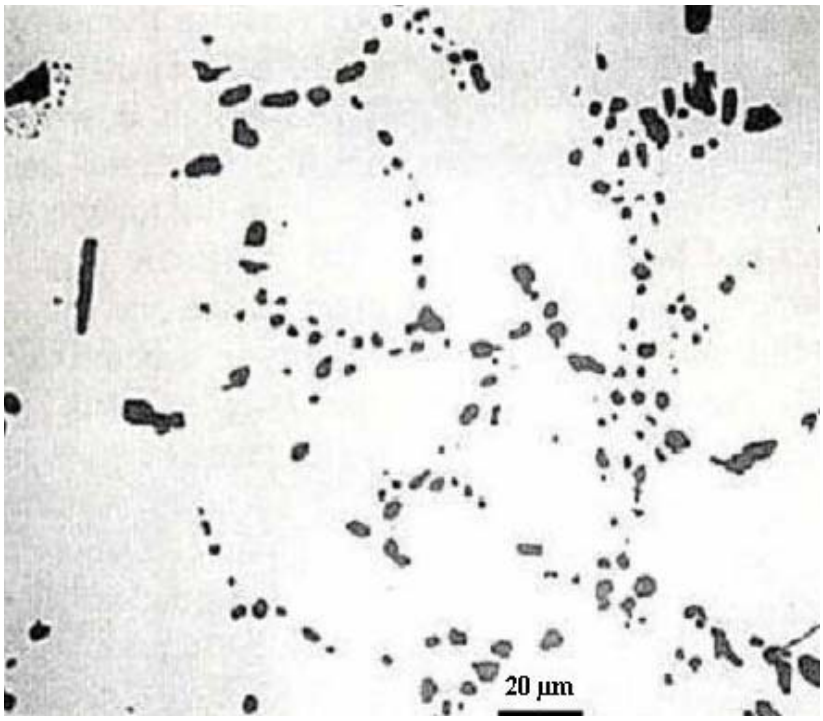

Figure 5.2 Optical micrograph A356-T6 cast aluminum alloy which shows second phase particles (Horstemeyer *et al.,* 2003).

Experiments

Two types of experiments using cylindrical specimens made of 7075-T651 and A356-T6 aluminum alloy were tested. The first set of specimens were pre-fatigued at specific strain amplitudes under fully reversible conditions and then stopped at predetermined cycles and pulled to failure. For the A356 alloy, eight specimens were pre-fatigued at a strain amplitude of 0.002, under fully reversible conditions, to 100, 1000, 10,000, and 100,000 cycles. The cyclic tests were conducted based on ASTM standard [E 606-99] at room temperature and a servo-hydraulic load frame was employed at 0.5 hertz. After completing the pre-fatiguing, the specimens were tensile tested at

room temperature. The 7075-T651 aluminum alloy was subjected to the same type loading sequence. Five specimens were pre-fatigued at a strain amplitude of 0.075 under fully reversible conditions to 100, 300, 500, 800 and 1,000 cycles. The cyclic tests were conducted based on ASTM standard [E 606-99] at room temperature and a servo-hydraulic load frame was employed at 2 hertz. After completing the pre-fatiguing, the specimens were tensile tested at room temperature. The experimental results of the tensile tests following low cycle fatigue for the 7075-T651 and the A356 aluminum alloys demonstrated a cyclic damage accumulation effect, as shown in Fig 5.3. For the A356 alloy, the failure strain was about 8.5% for the first 10,000 cycles. At 100,000 cycles, the specimens failed at about 4% strain. In contrast, the wrought alloy displayed a more immediate drop in failure strain with about 2% strain at 800 and 1,000 cycles. While the strain amplitude for the 7075-T651 alloy was higher than the cast alloy, both alloys displayed a degraded ductility due to the cyclic damage. Also for both alloys, specimens were cyclically loaded and then stopped, but instead of conducting a tensile test, the specimens were sectioned to quantify the microstructural damage evolution and the results are shown in Fig. 5.4.

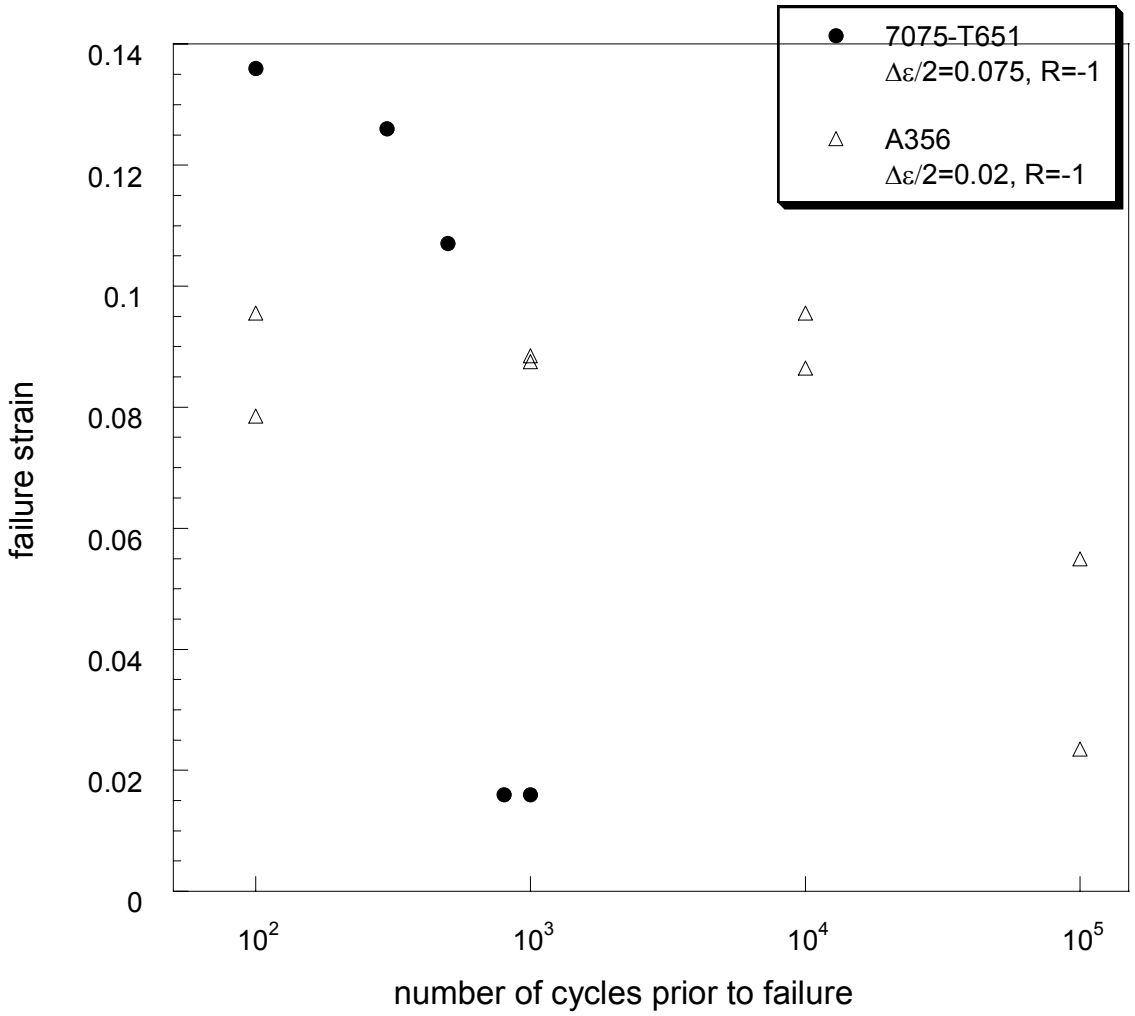

Figure 5.3 Failure strain as a function of pre-fatiguing for both 7075-T651 and A356 aluminum alloys.

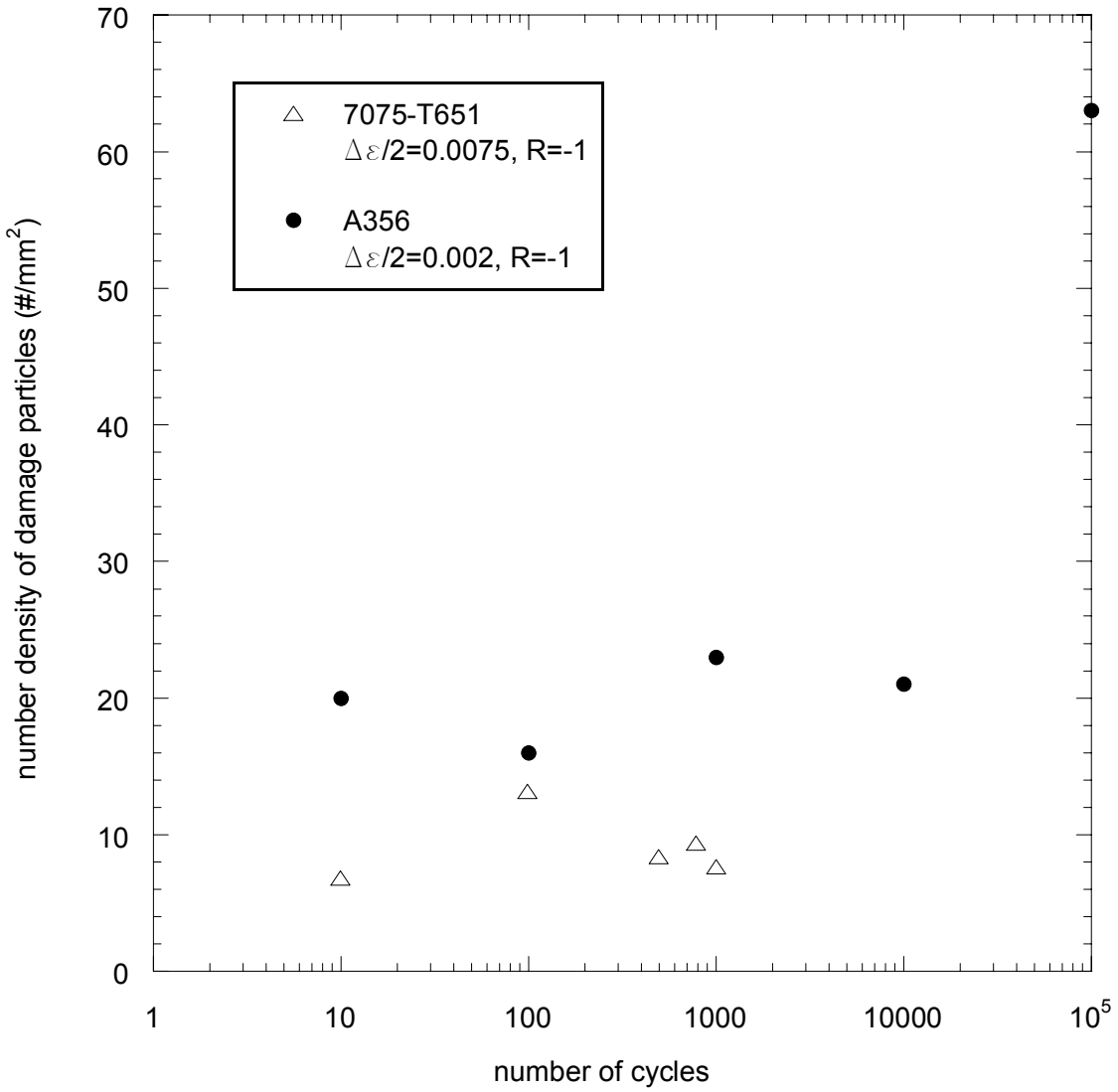

Figure 5.4 Number density per unit area versus applied cycles for both 7075-T651 and A356 aluminum alloys.

The second set of experiments for the wrought and cast alloys involved prestraining and then fatiguing the specimens until failure under fully reversible and strain controlled conditions. For the A356 alloy, eight specimens were tensile prestrained to levels of 1%, 2%, 3% and 3.6% at room temperature. After completing the

prestraining, the specimens were fatigue tested under fully reversible conditions at room temperature and at a strain controlled amplitude of 0.002. The fatigue tests were conducted based on ASTM standard [E 606-92] and a servo-hydraulic load frame was employed at 0.5 hertz. Again, the 7075-T651 aluminum alloy was subjected to the same type of loading sequence. For the wrought alloy, twenty specimens were tensile prestrained to levels of 1% (12 specimens), 5% (4 specimens), 10% (4 specimens) at room temperature. After completing the prestraining, the specimens were fatigue tested under fully reversible conditions at room temperature and at a strain controlled amplitude of 0.002. The fatigue tests were conducted based on ASTM standard [E 606-92] and a servo-hydraulic load frame was employed at 5 hertz. In order to compare the effect of the prestraining on the fatigue life for the 7075-T651 and A356 aluminum alloys, the strain-life results were compared to the fatigue results of specimens with no prestraining and are presented in Fig. 5.5 and 5.6, respectively. For A356 aluminum, the prestrained results fall within the scatter of the nonstrained specimens, indicating that no realizable effect occurred. However, for the 7075-T651 aluminum alloy, the prestrained specimens showed a distinct, degraded effect, with the 5% and 10% prestrained specimens having the shortest life. In addition to strain-life results presented, the fracture surfaces of the prestrained specimens for the 7075-T651 alloy were examined under the scanning electron microscope. Fig. 5.7 shows a debonded particle that initiated a fatigue crack for a specimen that was tensile prestrained to 10% and then fatigue tested at a strain amplitude of 0.0025. The specimen failed at 200,450 cycles.

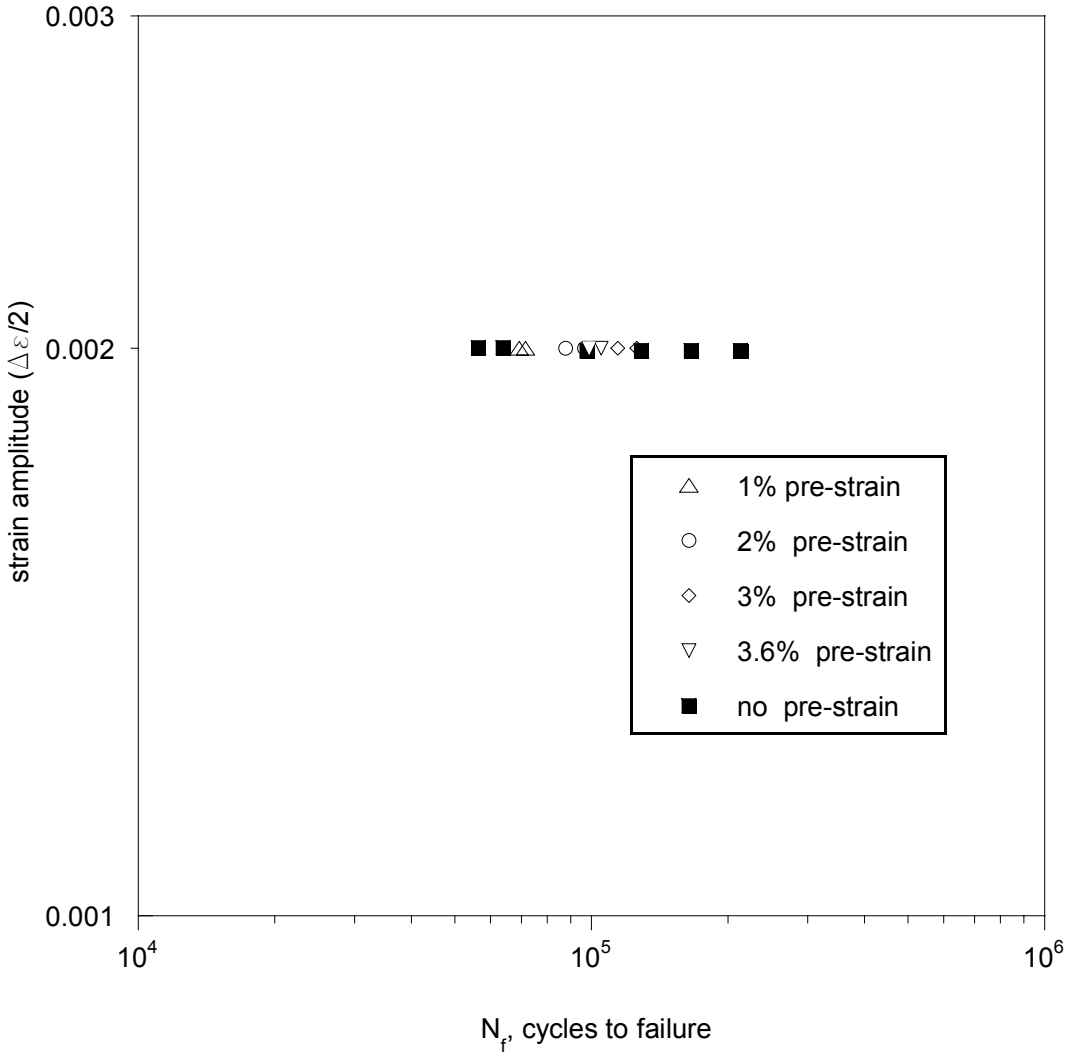

Figure 5.5 Strain-life results for prestrained and non-prestrained tests for A356 aluminum alloy show almost technical differences between the prestraining and non- prestrain cases.

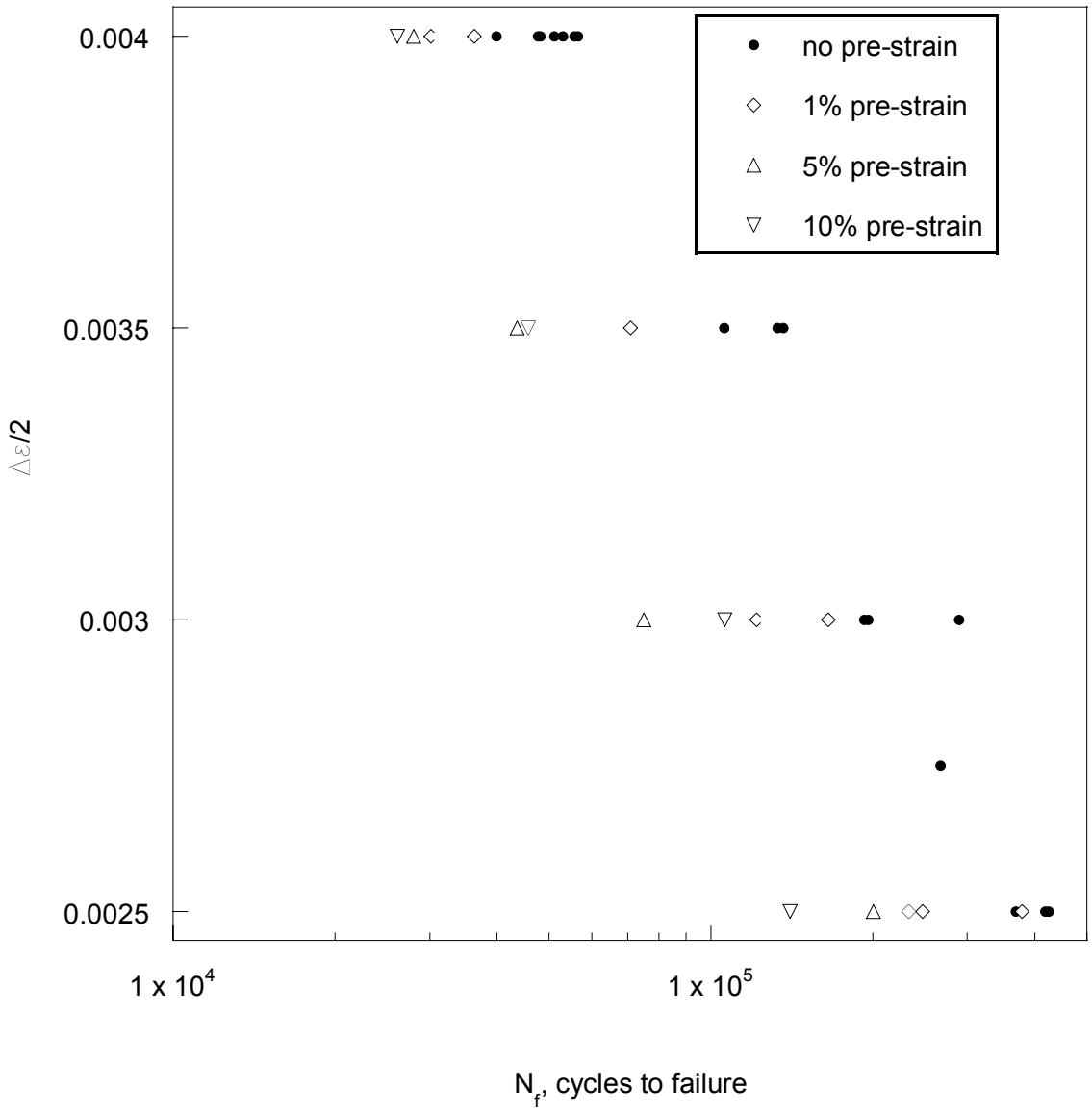

Figure 5.6 Strain-life results for prestrained and non-prestrained tests for 7075-T651 aluminum alloy indicate a strong relation of the prestraining on the final fatigue failure.

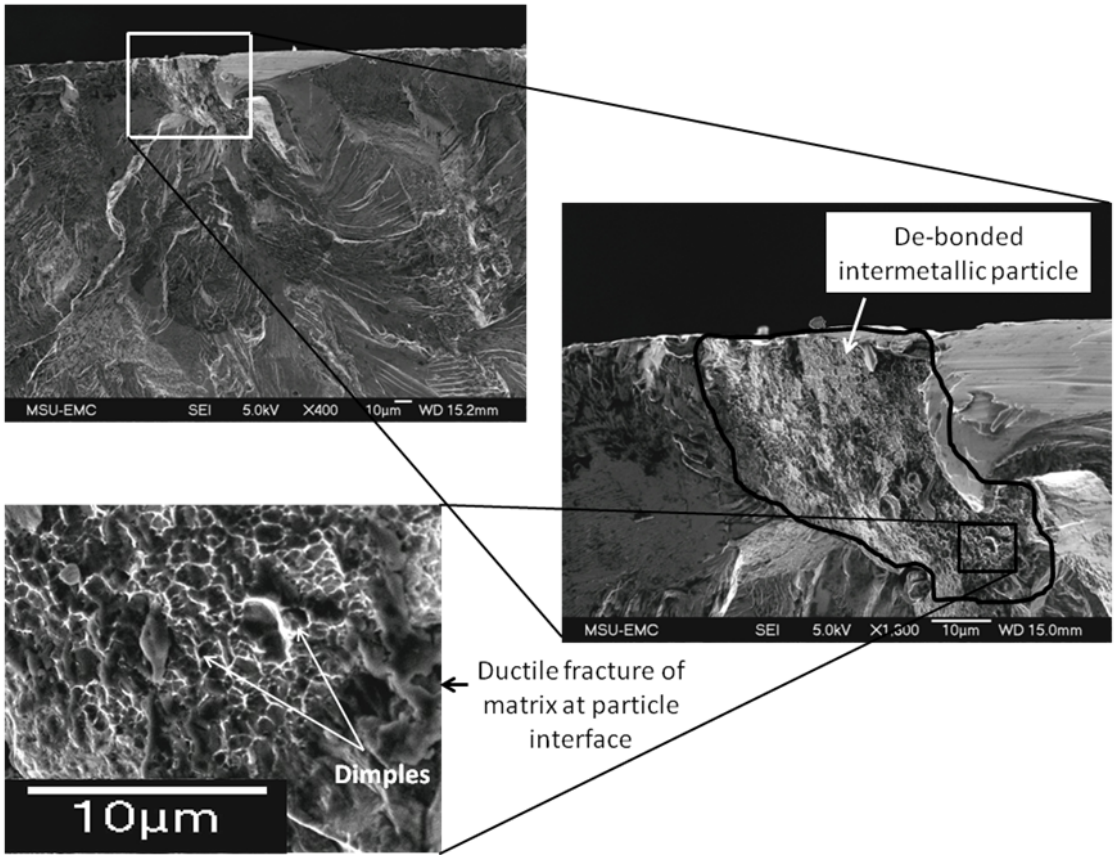

Figure 5.7 7075-T651 aluminum alloy fatigue crack initiation site. A fatigue crack initiated from a debonded particle as a result of the 10% prestrain. The dimples on the particle show that the prestraining caused the particle to debond. After 10% prestrain, the specimen was fatigued until failure with a strain amplitude of 0.0025 at R=-1. The specimen failed at 200,540 cycles.

Plasticity and Damage Model

The internal state variable (ISV) model employed in the study was first induced by Bammann and Aifantis (1989), Bammann (1990), and Bammann *et al*. (1996) and later modified to describe the nucleation, growth, and coalescence phenomenon (Horstemeyer *et al*., 2000a) arising from both large and small particles (see Chapter 2).

The ISV plasticity-damage model constants for 7075-T651 aluminum alloy were determined from experimental data by using a least sum-squared best-fit method. The plasticity equations are shown in Appendix A.2. The constants for the kinematic and isotropic hardening equations were selected to produce the best fit of the experimental tension, compression, and torsion data in the longitudinal direction. The damage constants were chosen based on experimental analysis of the fracture surface (see Chapter 2). The damage model constants are shown in Appendix C.1. A single-element finite element model was employed to model the stress and damage state.

MultiStage Fatigue (MSF) Model

The microstructurally-based multistage fatigue (MSF) model was developed based on the observations of four-stage fatigue damage evolutions at various scales (McDowell *et al.* 2003): nucleation, microstructurally small crack growth, physically small crack growth, and long crack growth. The fatigue damage driving mechanisms for each stage varies as the interaction of microscale-loading and microstructural features change. Based on microscale physics, the first MSF model was developed for a cast A356 Al alloy suitable for constant amplitude loading cases for various cast microscale features (McDowell, *et. al*., 2003). Later, this MSF model was extended to a wrought 7075-T651 aluminum alloy that captures the grain size and texture effects on fatigue lives under constant loading cases (Xue, *et. al*., 2007 a, b). A brief explanation of the MSF model is given below. The total fatigue life is decomposed into three stages,

$$N_{\text{Total}} = N_{\text{Inc}} + N_{\text{MSC/PSC}} + N_{\text{LC}} . \tag{5.1}$$

Here, N_{Total} is the total fatigue life. N_{Inc} is the number of cycles to incubate a crack at a micronotch formed by an inclusion, which can be a relatively large constituent particle, a large pore, or a cluster of each or both. The incubated crack extends from the inclusion into the matrix and propagates through a region of the micronotch root influence. $N_{\text{MSC/PSC}}$ is the number of cycles required for propagation of a microstructurally small/ physically small crack. Finally, N_{LC} is number of cycles required for long crack (LC) propagation to final failure, which depends on the amplitude of loading and the corresponding extent of microplasticity ahead of the crack tip. The MSC/PSC growth is a function of the crack tip displacement (Equation 5.2) and describes the crack growth regime, where ΔCTD is the crack tip displacement range, χ is a material constant, and ΔCTD_{th} is the threshold for crack tip displacement. The crack tip displacement, shown in Equation (5.3), is a function of remote loading where CI, CII, and ζ are constants based on small crack growth experiments

$$\left(\frac{da}{dN}\right)_{msc} = \chi\left(\Delta CTD - \Delta CTD_{th}\right) \tag{5.2}$$

$$_{\Delta CTD} = C_{II} f(\varphi)\left[\frac{U\Delta\hat{\sigma}}{S_{ut}}\right]^{\zeta} a + C_I\left(\left.\frac{\Delta\gamma^{p}_{\max}}{2}\right|_{macro}\right)^{2} \tag{5.3}$$

In this work, the microstructurally small crack formulation was modified to account for an initial damage state due to cracked or debonded particles. Thus, the $f(\varphi)$ function was altered as shown

$$f(\varphi) = 1 + \varpi(1-\varphi)^{\psi} \tag{5.4}$$

Where ϕ represents a void volume fraction or rather damage fraction, and ω and ψ are material modeling parameters. It is important to note that in Chapter 3, the MPS^2/(NND*DCS) term was implemented to capture the microstructural variance on fatigue life for the cast A356-T6 aluminum alloy. However, the MPS^2/(NND*DCS) term was not employed in this study. Lastly, Appendix C.2 lists the MSF model parameters which are based on work by Xue *et al*. (2007b).

Results and Discussion

The pre-fatiguing-followed-by-tension and prestraining-followed-by-fatiguing reveal a distinct difference for the two alloys studied in this work. The most obvious observation made from the experimental results was that the 7075-T651 alloy displayed a degraded strain at failure as a function of the pre-fatiguing and a lower fatigue life when prestrained prior to loading. While the A356 aluminum alloy also displayed a degraded strain at failure as a function of pre-fatiguing, the prestraining-followed-by-fatigue showed no effect compared to non-prestrained specimens. Therefore, for the modeling effort, we only focused on the 7075-T651 aluminum alloy in terms of predicting the fatigue-life for specimens subjected to prestraining. In addition, the ISV plasticity/damage model was employed to predict the strain at failure for the 7075-T651 alloy that was subjected to pre-fatiguing.

To predict the degradation in fatigue life for the prestrain specimens for the 7075-T651 alloy, knowing the initial damage state of microstructure was essential. First, based on work by Harris (2005), at 1% 5% and 10% pre-strain, the volume fraction of the

broken intermetallics was approximately 0.05, 0.35 and 0.7, respectively. Also, the volume fraction of intermetallics for this alloy in the untested state was about 0.025. Once the damage fraction was known, the effect of the prestrain on fatigue life was modeled. Fig. 5.8 displays the experimental results of the specimens that were prestrained followed by cyclic loading, along with non-prestrained specimens and the corresponding MSF model for 7075-T651 aluminum alloy. The model showed good agreement and followed the same trend as the experiments. However, the underlining point of the modeling was to show that the MSF could show a degraded fatigue life based on an initial damage fraction. This modeling approach seems reasonable considering the increased void volume acts like newly nucleated cracks. Hence, this deleterious effect of increased cracked particles only affects the incubation and microstructurally small crack growth regimes. Of course, the next obvious question is why did the A356 not show an effect from the prestraining? The answer lies in the fact that it was the maximum pore size that dominated the fatigue life of the A356 aluminum alloy in contrast to the larger intermetallics in the 7075-T651 alloy. The prestraining in the A356 aluminum alloy fractured and debonded the second phase silicon particles but did not really affect the porosity that was present. As such, the nucleation of smaller voids arising from the particles fracturing or debonding had really little effect on the fatigue life when you have larger voids dominating the process. On the other hand, when the fatigue occurred first for the A356 aluminum alloy, silicon particles were fractured and debonded and this played a big role in the ductile fracture of A356 aluminum alloy. Essentially in fatigue, the largest defect size is the most important factor (McDowell *et al*. 2003), but the total

porosity arising from pre-existing pores and pores nucleated from particles is the most important factor for monotonic ductility (Horstemeyer *et al*., 2000b). The 7075-T651 aluminum alloy had no pre-existing pores, so the second phase intermetallics were the main defect inducing failure for both the fatigue and monotonic loading conditions.

The next modeling thrust of this work was to compare the ISV model to the pre-fatigue-followed-by-tension experiments. As expected, the specimens not subjected to pre-fatigue or relatively few cycles (100) showed the largest strain to failure, while the specimens pre-fatigued to 800 and 1000 cycles showed the least ductility. The ISV model showed good agreement to the experiments for pre-fatiguing of 100, 300, 500, and 1,000 cycles. The set of constants for each specimen were identical, except for the nucleation rate constant, η, (see Appendix C) which was adjusted to obtain a good fit to the experimental results. The amount initial nucleation predicted by the model (Equation A.1.6) prior to the tensile loading was not comparable to the experimental void number density values shown Fig. 5.5. However, the approach employed here shows potential for predicting the strength and ductility for a material subjected to pre-fatiguing. In addition, the numerical and experimental results suggest that the elongation of the 7075-T651 alloy subjected to pre-fatiguing is dependent on void nucleation from cracked or debonded particles due to cyclic loading.

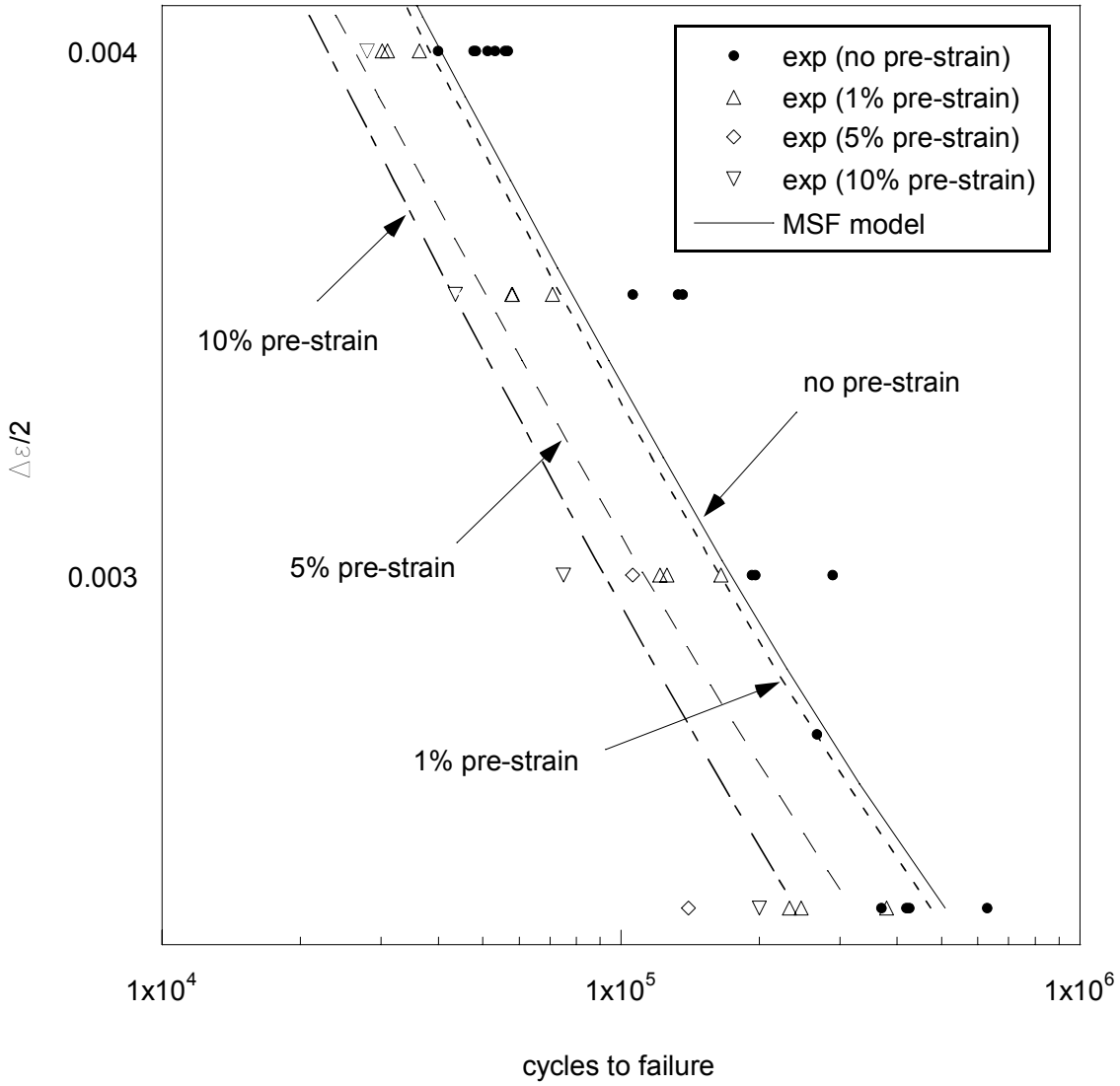

Figure 5.8 Predicted fatigue-life results for prestrain levels of 1%, 5%, and 10% and for specimen with no prestrain for 7075-T651 aluminum alloy.

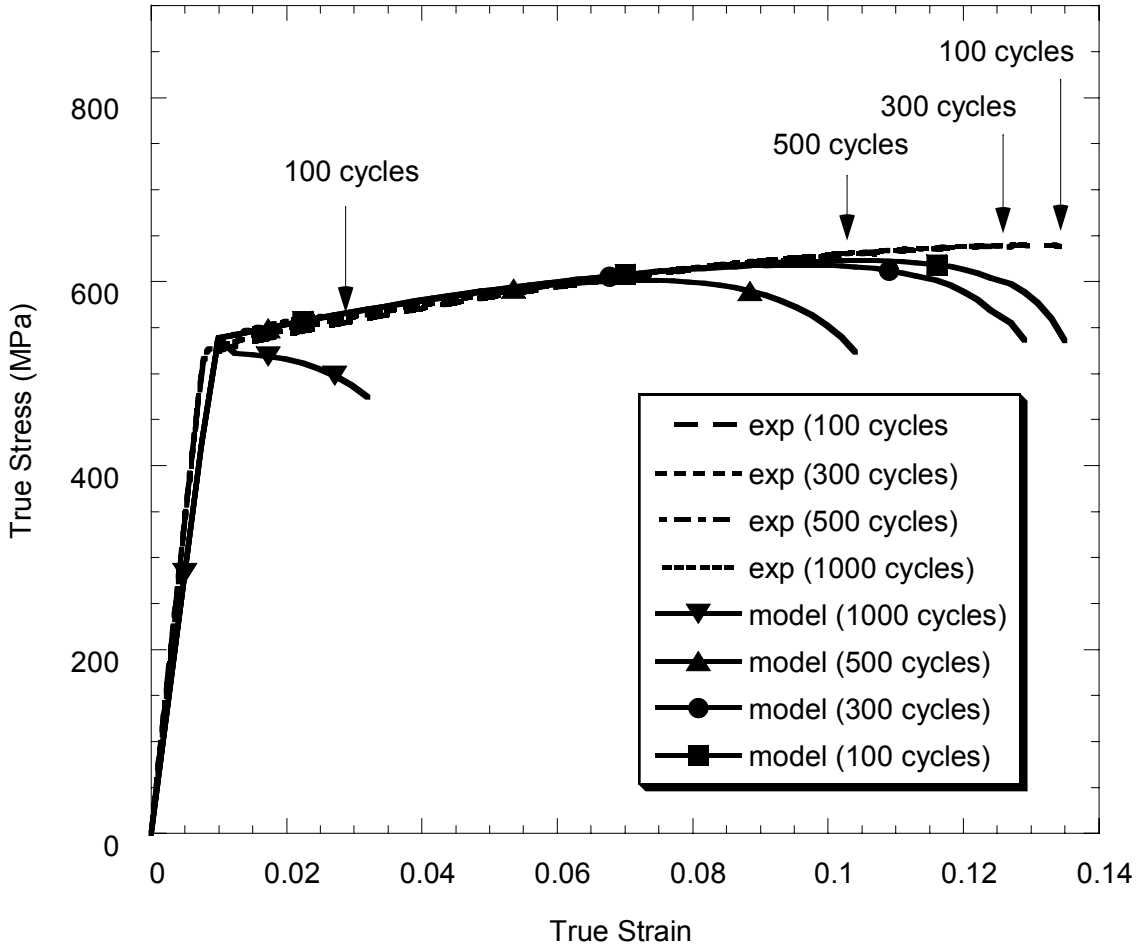

Figure 5.9 The experimental and modeling results for the tensile stress/strain behavior following low cycle fatigue for 7075-T651 aluminum alloy.

The main contribution of this work was to show that a material's strength, ductility, and fatigue resistance is a function of past damage history and the associated mechanisms related to that history. Thus, the damage history can be appropriately modeled using physically motivated microstructural material models for both monotonic and fatigue damage. The good correlation of the MSF fatigue model and ISV plasticity/damage model to the experimental results show that the damage effect due to

prestraining and pre-fatiguing are viable engineering tools and can distinguish between different mechanisms.

Conclusions

Experimental results for pre-fatiguing-followed-by-tension and prestraining-followed-by-cyclic-loading for a cast and a wrought aluminum alloy were presented. Specimens subjected to more precycling showed lower ductility for both alloys (7075-T651 and A356 Aluminum alloys). However, only the wrought alloy showed a degraded fatigue-life as a function of prestraining compared to the cast alloy which showed no effect. In addition, the MultiStage Fatigue model displayed good agreement with pre-straining-followed-by-cyclic loading experiments for the 7075-T651 alloy. Also, an internal state variable plasticity and damage model was employed to capture the tensile stress and damage state due to pre-fatiguing.

CHAPTER VI

SUMMARY AND FUTURE WORK

Summary

An internal state variable (ISV) plasticity/damage model was modified to capture the stress and damage state of 7075-T651 aluminum alloy. Modeling results along with scanning electron microscopy suggest that particle anisotropy is largely responsible for the anisotropic ductility of the wrought alloy. This study also showed that inclusion-property relations for fatigue on a cast A356 aluminum alloy can be integrated into a fatigue life model. A non-dimensional term comprised of the maximum pore size, nearest neighbor distance, and dendrite cell size was implemented into the MultiStage Fatigue (MSF) model with good agreement to the experimental results. Next, microstructurally small fatigue crack growth results were presented for a single-edge-notch specimen on the 7075-T651 aluminum alloy. Additionally, the FASTRAN model, calibrated to the small crack data, was employed to make fatigue-life predictions based on microstructural inclusion defects. Lastly, as a capstone to the work presented in the previous chapters, the ISV plasticity/damage and the MSF models were employed to predict failure for both the A356 and 7075 alloys that were prestrained and then fatigued and also specimens that were pre-fatigued, then tensile tested. Modeling and

experimental results reveal the damage mechanisms associated with these combined loading sequences.

Future Work

The modifications to the internal state variable plasticity/damage model described in Chapter II were employed to account for void nucleation due to cracked and/or debonded large and small particles. Since the work presented in Chapter II was based on experiments conducted at room temperature, modeling and experimental work can be performed on the 7075-T651 aluminum alloy to determine the structure-property relations for large and small particles at elevated temperatures.

Experimental and modeling efforts by Jordon *et al*. (2007) showed that the Bauschinger effect displayed by the 7075-T651 aluminum alloy is caused by both the back stress and damage accumulation. Future work on the topic of the Bauschinger effect could include examining a similar, but cleaner 7xxx series aluminum product: 7045-T651. With fewer intermetallic particles, the 7045 alloy should display a diminished Bauschinger effect. However, experimental results and model validation are needed.

Based on the experimental results of the small fatigue crack growth using the replica method, some multi-site fatigue cracking was observed. In addition, some instances of crack interaction and coalescence were observed. Thus, additional analysis of the 7075-T651 small crack results are needed to develop structure-property relations

for multi-site crack incubation, growth, and coalescence so as to improve future fatigue life prediction for engineering alloys with similar microstructural features.

In addition to the multi-site cracking, research could be conducted to study the crack initiation mechanism for aluminum alloys similar to the 7075-T651 alloy, but with fewer intermetallics. It is hypothesized that alloys with fewer intermetallics like 7045-T651 or 7050-T651 aluminum alloy would require more cycles under the same loading conditions to initiate an identical sized crack compared to the 7075-T651 alloy. Thus, the fatigue process for a cleaner alloy would be more incubation dominated and the alloy with more particles would be more crack growth dominated. However, small fatigue crack experiments on these or similar alloys are needed.

REFERENCES

Bammann, D. J., An Internal Variable Model of Viscoplasticity, eds. Aifantis, E. C. and Davison, L., Media with Microstructures and Wage Propagation, Int. J. Engineering Science, Vol. 8-10, Pergamon Press, p. 1041, 1984.

Bammann, D. J., and Aifantis, E. C., A Model for Finite-Deformation Plasticity, Acta Mechanica, 69, pp. 97-117, 1987.

Bammann, D.J., Aifantis, E.C., A Damage Model for Ductile Metals, Nuclear Engineering and Design;116: 355-362, 1989.

Bammann, D. J., Modeling Temperature and Strain Rate Dependent Large of Metals, Applied Mechanics Reviews, Vol. 43, No. 5, Part 2, May, 1990.

Bammann, D. J., Chiesa, M. L., Horstemeyer, M. F., and Weingarten, L. I., Failure in Ductile Materials Using Finite Element Methods, eds. N. Jones and T. Weirzbicki, Structural Crashworthiness and Failure, Elsevier Applied Science, 1993.

Bammann D.J., Chiesa M.L., Johnson G.C., Modeling Large Deformation and Failure in Manufacturing Processes App. Mech. eds, Tatsumi, Wannabe, Kambe. Elsevier Science: 256-276, 1996.

Berry, J.T., Kumble, R.G., Kumar, R., The Assessments of the Mechanical Behavior of Free-Machining Steels, Proceedings of ASM International Forum on Influence of Metallurgy on Machinability, edited by Vijay A. Tipnis, Chicago, pp. 234-246, 1975.

Brown, C. W.; and Smith, G. C.: A Two Stage Plastic Replication Technique for Monitoring Fatigue Crack Initiation and Early Fatigue Crack Growth, Advances in Crack Length Measurement, C. J. Beevers, Engineering Materials Advisory Services Ltd. (United Kingdom), pp. 41-51, 1982.

Buffie`re., J-Y., Savelli S., Jouneau, P.H. , Maire, E., Fouge`res, R., Experimental study of porosity and its relation to fatigue mechanisms of model Al–Si7–Mg0.3 cast Al alloys, Materials Science and Engineering. A, volume 316, pp.115-126, 2001.

Byczynski, G.E., Campbell, J., A Study of Crack Intiation sites in High Cycle Fatigue of 319 Aluminum Alloy castings, The John Campbell Symposium, Ed. By Murat Tiryakioglu and Paul N. Crepeau, TMS, pp. 235-244, 2005.

Dighe, M.D., Gokhale, A.M., Horstemeyer, M.F., Effect of Strain Rate on Damage Evolution in a Cast Al-Si-Mg Base Alloy. Metall. Mat. Trans A; 33A: 555-565, 2002.

Dougdale, D. S., Yielding of Steel Sheets Containing Slits, J. Mech. Phys. Solids, vol. 8, , pp. 100-104, 1960.

Edwards, P. R. and Newman, J. C., Jr., editors, Short-Crack Growth Behavior in Various Aircraft Materials, AGARD Report No. 767, 1990.

Elber, W., The significance of Fatigue Crack Closure in Damage Tolerance in Aircraft Structures, ASTM STP 486, p. 230-242, 1971.

Fan, J., McDowell, D.L., Horstemeyer, M.F., and Gall, K.A., Micromechanics Analysis and Model Development for Fatigue Behavior of a Microstructurally Small Crack Growing in Dual-Phase Materials, Engineering Fracture Mechanics, Vol. 68, No. 15, pp. 1687-1706, 2001.

Fan, J., McDowell, D.L., Horstemeyer, M.F., and Gall, K.A., Cyclic Plasticity in Pores and Inclusions in Cast Al-Si Alloys, Engineering Fracture Mechanics, vol. 70, no.10, p 1281-1302, 2003.

Fan, J., Hao, S., A Design-Centered Approach in Developing Al-Si-Based Light-Weight Alloys with Enhanced Fatigue Life and Strength, J. Computer-Aided Materials Design, 11: 139-161, 2004.

Forth, S. C., Newman, J. C., Jr. and Forman, R. G., On Generating Fatigue Crack Growth Thresholds, International Journal of Fatigue, Vol. 25, pp. 9-15, 2003.

Gall, K., Horstemeyer, M.F., Degner, B.W., McDowell, D.L., and Fan, J., On the Driving Force for Fatigue Crack Formation from Inclusions and Voids, International Journal of Fracture, Vol. 198, No. 3, pp. 207-233, 2001.

Gall, K., Yang, N., Horstemeyer, M.F., McDowell, D.L., and Fan, J., The Influence of Modified Intermettallics and Si Particles on Fatigue Crack Paths in a Commercial Cast A356 Al Alloy, Fatigue Frac. Eng. Mat. Struct., 23, pp. 159-172, 2000.

Gall, K., Yang, N., Horstemeyer, M.F., McDowell, D.L., and Fan, J., The Debonding and Fracture of Si Particles During the Fatigue of a Cast Al-Si Alloy, Met. Trans A., Vol. 30A, pp. 3079-3088, 1999.

Gangloff, R. P.: Electrical Potential Monitoring of Crack Formation and Subcritical Growth From Small Defects, Fatigue Eng. Mater. 84 Struct., voh 4, no. 1, pp. 15-33, 1981.

Garber, R., Bernstein, I. M., Thompson, A. W., 1976. Effect Of Hydrogen On Ductile Fracture Of Spheroidized Steel, Scripta Metall., v 10, n 4, Apr, p 341-345, 1976.

Garrison, W. M. Jr., Moody, N. R., Ductile Fracture, J. of Physics and Chem. of Solids, v 48, n 11, 1987, p 1035-1074, 1987.

Gurland J., and Plateau J., The mechanism of ductile fracture in metals containing inclusions, Trans. ASM, Vol. 56, PP 442-452, 1963.

Gungor, S., Edwards, L., Effect of Surface Texture on the Initiation and Propagation of Small Fatigue Cracks in a Forged 6082 Aluminium Alloy Materials Science and Engineering A (Switzerland). Vol. A160, no. 1, pp. 17-24, 1993.

Gregory, J.K., Gysler, A., Luetjering, G., The Influence of Texture on Fatigue Microcrack Propagation in an Al--Zn--Mg--Cu Alloy, Fatigue 84. Proceedings of the 2nd Conference on Fatigue and Fracture Thresholds. Vol. 2, Birmingham; UK; 3-7, pp. 847-856, Sept. 1984.

Hahn G.T., and Rosenfield A.R., Metallurgical Factors Affecting Fracture Toughness of Aluminum Alloys. Metall. Trans. A, vol. 6a, pp. 653-70, 1975.

Harris C.R. Particle Cracking Damage Evolution in 7075 Wrought Aluminum Alloy Under Monotonic and Cyclic Loading Conditions, M.S. Thesis, Georgia Institute of Technology, 2006.

Horstemeyer, M.F., Damage Influence on the Bauschinger Effect of a Cast A356 Aluminum Alloy, Scripta Materialia, Vol. 39, No. 11, pp. 1491-1495, 1998.

Horstemeyer, M. F. and Gokhale, A.M., A Void Nucleation Model for Ductile Materials, International Journal of Solids and Structures, Vol. 36, pp. 5029-5055, 1999.

Horstemeyer, M.F., Lathrop, J., Gokhale, A.M., and Dighe, M., Modeling Stress State Dependent Damage Evolution in a Cast Al-Si-Mg Aluminum Alloy, Theoretical and Applied Fracture Mechanics, Vol. 33, pp. 31-47, 2000a.

Horstemeyer, M.F., Matalanis, M.M., Sieber, A.M., and Botos, M.L., Micromechanical Finite Element Calculations of Temperature and Void Configuration Effects on Void Growth and Coalescence, Int J. Plasticity, Vol. 16, 2000b.

Horstemeyer, M.F. and Ramaswamy, S., On Factors Affecting Localization and Void Growth in Ductile Metals: A Parametric Study, Int. J. Damage Mech., Vol. 9, pp. 6-28, 2000.

Horstemeyer, M.F., Negrete, M., and Ramaswamy, S., Using a Micromechanical Finite Element Parametric Study to Motivate a Phenomenological Macroscale Model For Void/Crack Nucleation in Aluminum with a Hard Second Phase, Mechanics of Materials, Vol. 35, pp. 675-687, 2003.

Johnson, C.R. A Finite Element Evaluation of the Double Ligament Tension Test, Ph.D Dissertation, University of Alabama, 1994.

Jordon, J.B., Horstemeyer, M.F., Solanki, K., Xue, Y., Damage and stress state influence on the Bauschinger effect in aluminum alloys, Mechanics of Materials, 39 (10), p.920-931, 2007.

Kumble, R.G., The Evaluation of Anisotropy and Plane Strain Properties of Cast and Wrought Materials, Ph.D Dissertation, University of Vermont, 1973.

Kumble, R.G., Berry, J.T., Jalewalia, G., An Investigation of Anisotropy in Preminum Quality Aluminum Castings, Transaction of the American Foundryman's Society, Vol 83, pp. 295-298, 1975.

Kumble, R.G., Berry, J.T., The Application of the Double Ligament Tensile Test in Deformation Processing, J. Eng. for Industry, Vol 98, 4, pp. 1237-1242, 1976.

Kumai, S., Hu, J., Higo, Y., Nunomura, S., Effects of dendrite cell size and particle distribution on the near-threshold fatigue crack growth behaviour of cast Al-SiCp composites Acta Materialia, v 44, n 6 p 2249-225, 1996.

Lados, D.A., Diran, A., Fatigue crack growth characteristics in cast Al–Si–Mg alloys Part I. Effect of processing conditions and microstructure, Materials Science and Engineering. A, volume 385, pp.200-211, 2001.

Lados, D.A., APELIAN, D., MAJOR, J.F., Fatigue Crack Growth Mechanisms at the Microstructure Scale in Al-Si-Mg Cast Alloys: Mechanisms in Regions II and III, Materials Science and Engineering. A, volume 37A, pp.2405, 2006.

Lankford J., Growth of small fatigue cracks in 7075-T6 Aluminum. Fatigue Fract Engng Mater Struct; 5: 233-248, 1982.

Major, J.F., Porosity Control and the Fatigue Behavior in A356-T61 Aluminum Alloy, AFS Trans, 102, pp. 901-906, 1994.

Manjunatha, C.M., Parida, B.K., Prediction of fatigue crack growth after single overload in an aluminum alloy, AIAA journal, v 42, n8, August, p 1536-1542, 2004.

McClintock F. A., On the mechanics of fracture from inclusions," Ductility, Metals Park, Ohio, 1968.

Meyers, C.W., Saigal, A., Berry, J.T., Fracture Related Properties of Aluminum A357-T6 Cast Alloy and Their Interrelation with Microstructure, AFS Transactions Vol. 1, pp. 281-288, 1983.

Meyers, C.W., Transverse Property Determination of Aluminum Armor Alloys by Double Ligament Tests, for U.S. Amy Materials Testing Laboratory, Watertown MA, Contract no. DAAL03-86-0001, 1986.

McDowell, D.L., An Engineering Model for Propagation of Small Cracks in Fatigue, Engng Fract Mech; 56, p.357–377, 1997.

McDowell, D.L., Gall, K., Horstemeyer, M.F., and Fan, J., "Microstructure-Based Fatigue Modeling of Cast A356-T6 Alloy," Engineering Fracture Mechanics, Vol. 70, pp.49-80, 2003.

Newman, J.A., Willard, S.A., Smith, S.W., Piascik, R.S., Flow Liner Slot Edge Replication Feasibility Study, Nasa/TM-2006-213921, February 2006.

Newman, J.C., Jr., A Crack-Closure Model for Predicting Fatigue Crack Growth under Aircraft Spectrum Loading, Methods and Models for Predicting Fatigue Crack Growth under Random Laoding, ASTM STP 748, American Society for Testing and Materials, Philadelphia, PA, PP. 53-84, 1981.

Newman, J. C., Jr., A Nonlinear Fracture Mechanics Approach to the Growth of Small Cracks. Behaviour of Short Cracks in Airframe Components, AGARD-CP-328, pp. 6-16-26, Apr. 1983.

Newman, J.C., Jr. and Edwards, P. R., Short-Crack Growth Behavior in an Aluminum Alloy - An AGARD Cooperative Test Program, AGARD Report No. 732, 1988.

Newman, J.C., Jr., FASTRAN II--A Fatigue Crack Growth Structural Analysis Program. NASA TM-104159, 1992.

Newman, J.C., Jr, Wu XR, Venneri SL, Li CG. Small-crack effects in high-strength aluminum alloys. NASA Reference Publication 1309, May 1994.

Newman, J. C., Jr., Schneider, J., Daniel, A. and McKnight, D., Compression precracking to generate near threshold fatigue-crack-growth rates in two aluminum alloys, International Journal of Fatigue, Vol. 27, pp. 1432-1440, 2005.

Newman, J.C., Jr., Jordon, J.B., Anagnostou, E.L., Fridline, D., and Rusk, D., Fatigue and crack-growth analysis on specimens simulating details in wing panels of naval aircraft, Aging Aircraft Confernce, Phoenix, AZ, April 2008.

Oppenheimer, E.D., Berry, J.T., Measure of Short-Transverse Tensile-Impact Energy of Rolled Steel Plate, ASME Publication No. 68-PVP-18, 1968.

Picu, C., Interface Crack Impinging on a Triple Junction, International Journal of Solids Structures, , 33, pp. 1563, 1996

Picu, C., Gupta, V., Stress Singularities at Triple Junctions with Freely Sliding Grains, International Journal of Solids Structures, , 33, 1535, 1996.

Pearson, S., Initiation of Fatigue Cracks in Commercial Aluminum Alloys and the Subsequent Propagation of Very Short Cracks, Engineering Fracture Mechanics, Vol. 7, p 235-247, 1975.

Potirniche, G.P., Barlat, F., Daniewicz, S.R., Garratt, M., Bray, G., The influence of aluminium alloy anisotropic texture on crack-tip plasticity, Fatigue and Fracture of Engineering Materials and Structures, v 27, n 12, p 1157-1169, 2004.

Przystupa, M.A., Bucci, R.J., Magnusen, P.E., Hinkle, A.J. Microstructure based fatigue life predictions for thick plate 7050-T7451 airframe alloys, Int. J. Fatigue, v19, 93, p. 285-288, 2004.

Rawal S.P., and Gurland J., Observations On The Effect Of Cementite Particles On The Fracture Toughness Of Spheroidized Carbon Steels**.** Metall. Trans. A, , vol. 8A, pp. 691-98, 1977.

Rogers, H.C., The Tensile Fracture of Ductile Metals, Transactions of the Metallurgical Society of AIME, Vol. 218, pp. 498-506, 1960.

Schijve, J., The Practical and Theoretical Significance of Small Cracks – An Evauation, Fatigue 84, EMAS, Ltd., p. 751-771, 2004.

Srivatsan, T.S., Badrinath, K., Berry, J.T., Short Transverse Mechanical Properties of a Precipitation Hardened Aluminum Alloy. Aluminum Vol. 61, pp. 366-369, 1985.

Srivatsan, T.S., Meyers, C.W., Berry, J.T., A Method for Determining the Tensile Properties and Anisotropy of Aluminum Alloys. J. Testing and Evaluation, Vol. 15 , pp. 196-204, 1987.

Starke, Jr. E.A., Aluminium Alloys Of The 70's: Scientific Solutions To Engineering Problems. An Invited Review Mater. Sci. Eng., vol. 29, pp. 99-115, 1977.

Stephens, R.I., Berns, H.D., Chernenkoff, R.A., Indig, R.L., Koh, S.K., Lingenfelser, D.J., Mitchell, M.R., Testin, R.A., and Wigant, C.C., "Low-Cycle Fatigue of A356-T6 Cast Aluminum Alloy Wheels," Fatigue and Fracture Toughness of A356-T6 Cast Aluminum Alloy, SAE Tech. Publ. SP760, Vol. 881701, pp. 1-28, 1988a.

Stephens, R.I., Mahoney, B.J. and Fossman, R.G., Low Cycle Fatigue of A356-T6 Cast Aluminum Alloy Wheels, Fatigue and Fracture Toughness of A356-T6 Cast Aluminum Alloy, SAE Tech. Publ. SP760, Vol. 881707, pp. 93-102, 1988b.

Suresh, S., Fatigue of Materials, Cambridge University Press, New York, 1998.

Swain, M. H.; and Newman, J. C., Jr.: On the Use of Marker Loads and Replicas for Measuring Growth Rates for Small Cracks. Fatigue Crack Topography, AGARDCP-376, pp. 12-1 12-17, Nov. 1984.

Stotz, R.C. Berry, J.T., Anctil, A.A., Oppenheimer, Charterizating the through-thickness Properties of Ultra-High-Strength Steel Plate. Through-thickness Tension testing of steel, ASTM STP 794, edited by R. J. Glodowski, American Society for Testing of Materials, Philadelphia, pp. 70-84, 1983.

Tanaka, K., Hojo, M., Nakai, Y., Fatigue Crack Initiation and Early Propagation in 3% Silicon Iron, Fatigue Mechanisms: Advances in Quantitative Measurements of Physical Damage, ASTM STP 811, J. Lankford, D.L. Davidson, W.L. Morris, R.P. Wei, Eds., American Society for Testing and Materials, p. 207-232, 1983.

Tokaji, K, Notch fatigue behaviour in a Sb-modified permanent-mold cast A356-T6 aluminium alloy, Mat. Sci. Eng. A 396, 2005, pp. 333-340, 2005.

Tsuda, H., Daimaruya, M., Kobayashi, H., Sunayama, Y., Effect of pre-fatigue on impact tensile properties of laser welded butt joint of high strength steel plates Zairyo/ Journal of the Society of Materials Science, Japan, v 55, n 9, p 824-830, September, 2006.

Venkateswara Rao, K.T, Ritchie, R.O., Mechanisms for the retardation of fatigue cracks following single tensile overloads: Behaviors in aluminum-lithium alloys, Acta Metallurgica, v36, n10, p 2849-2862, Oct, 1988.

Wagner, L., Gregory, J.K., Gysler, A., Lutjering, G., Propagation Behavior of Short cracks in Ti-8.6 Al alloy. In Small Fatigue Cracks (eds. R.O. Ritchie &J. Lankford), pp. 117-28. Warrendale; The Metallurgical Society of the America Institute of Mining, Mineral and Petroleum Engineers, 1986.

Wang, L., Daniewicz, S.R., Horstemeyer, M.F., Sintay, S., Rollett, A.D. Three Dimensional Finite Element Analysis Using Crystal Plasticity for a Parameter Study of Microstructurally Small Fatigue Crack Growth in a 7075 Aluminum Alloy, Int. J. Fatigue, 2008 [in press]

Wang, Q.G., Crepeau, P.N., Griffiths, J.R., Davidson, C.J., The Effects of Oxide Films and Porosity on Fatigue of Cast Aluminum Alloys. The John Campbell Symposium, Ed. By Murat Tiryakioglu and Paul N. Crepeau, TMS, pp. 205-214, 2005.

Walker, A. C.: Continuous Fatigue Crack Inspection of Aluminum Alloy Plate Specimens Undergoing Spectrum Loading Using Ultrasonic Surface Waves. LTR-ST-1465, National Aeronautical Establ., National Research Council of Canada, July 1983.

Xue, Y., El Kadiri, H., Horstemeyer, M.F., Jordon, J.B., Weiland, H., Micromechanisms of Multistage Crack Growth in a High-Strength Aluminum Alloy, Acta Materialia, 55(6), 1975-1984, Oct. 2007a.

Xue, Y., McDowell, D., Horstemeyer, M.F., Dale, M., Jordon, J.B., Microstructure-based multistage fatigue modeling of aluminum alloy 7075-T651. Engineering Fracture Mechanics, 74, 2810-2823, Aug 2007b.

Yi, J.Z., Gao, Y.X., Lee, P.D., Flower., H.M., Lindley, T.C., "Scatter in Fatiuge Life Due to Effect of Porosity in Cast A356-T6 Aluminum –Silcon Alloys" Metallurgical and Materials Transaction A, volume 34A, pp.1879, 2003.

Yi, J.Z., Gao, Y.X., Lee, P.D., Lindley, T.C., Effect of Fe-content on fatigue crack initiation and propagation in a cast aluminum–silicon alloy (A356–T6) Materials Science and Engineering A 386, 396–407, 2004.

Yi, J.Z., Gao, Y.X., Lee, P.D., Lindley, T.C., Microstructure-Based Fatigue Life Prediction for Cast A356-T6 Aluminum-Silicon Alloys, Metallurgical and Materials Transaction B, volume 37B, pp.306, 2006.

Yi, J.Z., Lee, P.D., Lindley, T.C., Fukui, T., Statistical modeling of microstructure and defect population effect on the fatigue performance cast A356-T6 autommotive components, Materials Science and Engineering. A, volume 432, pp.59-68, 2006.

Zhai, T., The effects of macro- and micro-texture on the fatigue properties of Al-Li 8090 alloys, Advances in the Metallurgy of Aluminum Alloys, p 83-92, 2001.

Zhai, T., Jiang, X.P., Li, J.X., Garratt, M.D., Bray, G.H., The grain boundary geometry for optimum resistance to growth of short fatigue cracks in high strength Al-alloys, Int. J., 1202-1209, Fatigue 27, 2005

Zhang, B., Poirier, D.R., and Chen, W. Microstructural Effects on High-Cycle Fatigue-Crack Initiation in A356.2 Casting Alloy, Metallurgical and Materials Transactions A, 30A, pp. 2659-2666, 1999.

Zhang, X.P., Wang, C.H., Ye, L., Mai, Y.W., In situ Investigation of small fatigue crack growth in poly-crystal and single crystal aluminum alloys, Fatigue Fract. Engng Mater Struct 25, pp. 141-150, 2001.

Zhu, X.,. Yi, J.Z ., Jones, J.W., Allison, J.E., A Probabilistic Model of Fatigue Strength Controlled by Porosity Population in a 319-Type Cast Aluminum Alloy: Part I. Model Development, Metallurgical and Materials Transaction A, volume 38A, pp.1111, 2007.

.

APPENDIX A

ISV MODEL CONSTANTS FOR 7075-T651 ALUMINUM ALLOY

Table A.1 ISV plasticity/damage model equations (rate form).

$$\underline{D}_d^p = \sqrt{\frac{3}{2}} f(T) \sinh\left[\frac{\sqrt{3J_2^*} - \{R + Y(T)\}(1-\phi)}{V(T)(1-\phi)}\right] \underline{n}d \tag{A.1.1}$$

$$\dot{\underline{\alpha}} = \left\{h(T)\underline{D}^p - \left[r_d(T)\left\|\underline{D}^p\right\| + r_s(T)\right]\|\underline{\alpha}\|\underline{\alpha}\right\}\left(\frac{GS_0}{GS}\right)^Z \tag{A.1.2}$$

$$\dot{R} = \left\{H(T)\left\|\underline{D}^p\right\| - \left[R_d(T)\left\|\underline{D}^p\right\| + R_s(T)\right]R^2\right\}\left(\frac{GS_0}{GS}\right)^Z \tag{A.1.3}$$

$$\dot{D} = \left[\dot{\phi}_{particles} + \dot{\phi}_{pores}\right] C + \left[\phi_{particles} + \phi_{pores}\right] \dot{C} \tag{A.1.4}$$

$$\dot{\phi}_{particles} = \dot{\eta}_{l\arg e} v_{l\arg e} + \eta_{l\arg e}\dot{v}_{l\arg e} + \dot{\eta}_{small} v_{small} + \eta_{small}\dot{v}_{small} \tag{A.1.5}$$

$$\dot{\eta}_{primary/\sec ondary} = \left\|\underline{D}^P\right\| \frac{d^{1/2}}{K_{IC} f^{1/3}} \eta\left\{a\left[\frac{4}{27} - \frac{J_3^2}{J_2^3}\right] + b\frac{J_3}{J_2^{3/2}} + c\left\|\frac{I_1}{\sqrt{J_2}}\right\|\right\} \exp\left(C_{\eta T}/T\right) \tag{A.1.6}$$

$$\dot{v}_{primary/\sec ondary} = \frac{\sqrt{3}R_0}{2(1-n)}\left[\sinh\left(\sqrt{3}(1-n)\frac{\sqrt{2}I_1}{3\sqrt{J_2}}\right)\right]\left\|D^P\right\| \tag{A.1.7}$$

$$\dot{\phi}_{pores} = \left[\frac{1}{(1-\phi_{pores})^m} - (1-\phi_{pores})\right]\sinh\left\{\frac{2\left(2^{V(T)/Y(T)} - 1\right)}{\left(2^{V(T)/Y(T)} + 1\right)}\frac{\sigma_H}{\sigma_{vm}}\right\}\left\|\underline{D}^P\right\| \tag{A.1.8}$$

$$\dot{c} = \left[cd_1 + cd_2\left(\dot{\phi}_{particles}\right)\right]\exp(C_{CT}T)\left(GS_0/GS\right)^Z \tag{A.1.9}$$

Table A.2 Microstructure-property (elastic-plastic) model constants for 7075-T651 aluminum alloy.

7075-T651	Constants	L	L-T	ST
Constants for J/B formulas for G and K	G (MPa)	26426.3	26426.3	26426.3
	a	1	1	1
	Bulk (MPa)	68915.7	68915.7	68915.7
	b	58600	58600	58600
	melt temp (K)	1494	1494	1494
Specifies the yield stress	C1 (MPa)	0	0	0
	C2 (K)	0	0	0
	C3 (MPa)	360	360	360
	C4 (K)	110	110	110
	C5 (1/MPa)	1	1	1
	C6 (K)	0	0	0
Kinematic hardening and recovery terms	C7 (1/MPa)	0.02	0.02	0.02
	C8 (K)	0	0	0
	C9 (MPa)	2770	2770	2770
	C10 (K)	5	5	5
	C11 (sec/MPa)	0	0	0
	C12 (K)	0	0	0
Isotropic hardening and recovery terms	C13 (1/MPa)	.01	.01	.01
	C14 (K)	0	0	0
	C15 (MPa)	4150	4150	4150
	C16 (K)	12	12	12
	C17 (sec/MPa)	0	0	0
	C18 (K)	0	0	0
Hardening & recovery cons.	Ca	1.3	1.3	1.3
	Cb	-0.4	-0.4	-0.4
Temperature	init.temp (K)	297	297	297
	heat gen. Coeff.	0.3	0.3	0.3

Table A.3 Microstructure-property (damage) model constants for 7075-T651 aluminum alloy.

	Constants	L	L-T	S-T
McClintock Void Growth (primary)	void growth exp	0.3	0.3	0.3
	init. Rad. (mm)	0.0093	0.0112	0.0160
McClintock Void Growth (secondary)	void growth exp	0.3	0.3	0.3
	init. Rad. (mm)	0.0001	0.0001	0.0001
Nucleation (primary)	a	2500	2500	2500
	b	8100	8100	8100
	c	500	500	1500
	nuc coeff	0.007	0.007	0.007
	fract. Toughness MPa($m^{1/2}$)	29	29	29
	part. Size (mm)	0.0093	0.0112	0.0160
	part. Vol fract.	0.028	0.028	0.028
Nucleation (secondary)	a	47500	47500	47500
	b	153900	153900	153900
	c	9500	9500	9500
	nuc coeff	0.5	0.5	0.5
	fract. Toughness MPa($m^{1/2}$)	29	29	29
	part. Size (mm)	0.000063	0.000071	0.000112
	part. Vol fract.	0.032	0.032	0.032
Coalescence	cd1	14.645	14.645	14.645
	cd2	3	3	3
	cd3	10	10	10
	dcs0 (mm)	40	40	40
	dcs (mm)	40	40	40
	dcs exp. Zz	0.1	0.1	0.1
	nearest neighbor dist. (mm)	0.018	0.016	0.021
CA pore growth	init. Void vol. Fract.	0.0001	0.0001	0.0001
Nucleation	nuc. Temp. depend.	-2500	-2500	-2500
Coalescence	coal. Temp. depend	-0.01	-0.01	-0.01
Yield strength Adjustment terms	c19	0	0	0
	c20	0	0	0

APPENDIX B

MSF MODEL CONSTANTS FOR A356-T6 ALUMINUM ALLOY

Table B.1 MultiStage Fatigue model constants for A356-T651 aluminum alloy

Properties	upper bound	lower bound
Sut (MPa)	310	310
ζ	4.80	4.80
α	-0.48	-0.48
C_m	0.0870	0.0870
CTD_{th}	0.0002860	0.0002860
CI (in microns)	2400000	2400000
CII (in microns)	0.003	0.003
DCS (microns)	20	60
NND (microns)	794	488
MPS (microns)	90	265
ε_{th}	0.0005	0.0005
ε_{per}	0.0023	0.0023
η_{lim}	0.3	0.3
q	2.30	2.30
y1	3500	3500
y2	266	266
A (m/cyc-$(MPa\sqrt{m})^{-4.2}$)	1.5×10^{-11}	1.5×10^{-11}
M	4.2	4.2

APPENDIX C

ISV AND MSF MODEL CONSTANTS FOR 7075-T651 ALUMINUM ALLOY

Table C.1 Microstructure-property (damage) model constants for 7075-T651 aluminum alloy.

	Constants	100 cycles	300 cycles	500 cycles	1,000 cycles
McClintock Void Growth (primary)	void growth exp	0.3	0.3	0.3	0.3
	init. Rad. (mm)	0.0093	0.0093	0.0093	0.0093
McClintock Void Growth (secondary)	void growth exp	0.3	0.3	0.3	0.3
	init. Rad. (mm)	0.0001	0.0001	0.0001	0.0001
Nucleation (primary)	a	3500	3500	3500	3500
	b	11340	11340	11340	11340
	c	700	700	700	700
	nuc coeff	0.002	0.004	0.03	7
	fract. Toughness MPa(m^1/2)	29	29	29	29
	part. Size (mm)	0.0093	0.0093	0.0093	0.0093
	part. Vol fract.	0.028	0.028	0.028	0.028
Nucleation (secondary)	a	120000	120000	120000	120000
	b	324000	324000	324000	324000
	c	20000	20000	20000	20000
	nuc coeff	0.00003	0.00003	0.00003	0.00003
	fract. Toughness MPa(m^1/2)	29	29	29	29
	part. Size (mm)	0.000063	0.000063	0.000063	0.000063
	part. Vol fract.	0.032	0.032	0.032	0.032
Coalescence	cd1	10	10	10	10
	cd2	1	1	1	1
	cd3	200	200	200	200
	dcs0 (mm)	40	40	40	40
	dcs (mm)	40	40	40	40
	dcs exp. Zz	0.1	0.1	0.1	0.1
	nearest neighbor dist. (mm)	0.018	0.018	0.018	0.018
CA pore growth	init. Void vol. Fract.	0.0001	0.0001	0.0001	0.0001
Nucleation	nuc. Temp. depend.	-2500	-2500	-2500	-2500
Coalescence	coal. Temp. depend	-0.01	-0.01	-0.01	-0.01
Yield strength Adjustment terms	c19	0	0	0	0
	c20	0	0	0	0

Table C.2 MultiStage Fatigue model constants for 7075-T651 aluminum alloy.

Properties	No pre-strain	1% pre-strain	5% pre-strain	10% pre-strain
Sut (MPa)	515	515	515	515
ζ	0.173526	0.173526	0.173526	0.173526
α	-0.698266	-0.698266	-0.698266	-0.698266
C_m	0.3	0.3	0.3	0.3
CTD_{th}	0.0002860	0.0002860	0.0002860	0.0002860
CI (in microns)	80000	80000	80000	80000
CII (in microns)	0.003465	0.003465	0.003465	0.003465
ω	1.997	1.997	1.997	1.997
φ	0.00015	.0014	0.01	0.02
ψ	100	100	100	100
ε_{th}	0.0005	0.0005	0.0005	0.0005
ε_{per}	0.0023	0.0023	0.0023	0.0023
η_{lim}	0.3	0.3	0.3	0.3
q	2.30	2.30	2.30	2.30
y1	146	146	146	146
y2	300	300	300	300
A (m/cyc-$(MPa\sqrt{m})^{-4.2}$)	1.5×10^{-11}	1.5×10^{-11}	1.5×10^{-11}	1.5×10^{-11}
M	4.8	4.8	4.8	4.8